



## DIPLOMARBEIT

# As-deposited $VO_2$ Thin Films by Reactive DC Magnetron Sputtering at Reduced Target Cooling

zur Erlangung des akademischen Grades

**Diplom-Ingenieur**

im Rahmen des Studiums

**Technische Physik**

eingereicht von

**Anatol Beck**

Matrikelnummer 01125712

ausgeführt am Institut für Festkörperphysik  
der Fakultät für Physik der Technischen Universität Wien

Betreuer: Ao. Univ. Prof. Dipl.-Ing. Dr. Christoph Eisenmenger-Sittner

Wien, 13.12.2018

---

(Unterschrift Verfasser)

---

(Unterschrift Betreuer)



## Abstract

This work is focused on the production of vanadium dioxide thin films onto glass substrates by reactive DC magnetron sputtering at elevated target temperature between full target cooling (18 °C) and about 700 °C. Vanadium dioxide is thermochromic and exhibits a transition from a semiconducting (monoclinic) to a metallic (tetragonal) phase (SMT) at about 68 °C in bulk. The transition is accompanied by an increase in electrical conductivity as well as a decrease of transmittance in the infrared region. In thin films the SMT shows additionally a hysteresis behaviour. For these properties vanadium dioxide thin films are an intensively studied topic in research for temperature driven devices such as smart windows, optical switching or memory devices. DC magnetron sputtering allows the production of high quality thin films and is therefore widely used in research and industry.

However, during this work it could be shown that vanadium dioxide thin films are very difficult to produce and stabilize with reactive DC magnetron sputtering at full target cooling, as many oxides of vanadium have similar bond enthalpies close to the one of vanadium dioxide. As a further approach, the target cooling was gradually decreased by reducing the contact area between cooling system and target to investigate the influence on the sputter process and oxide film properties. The target temperature was therefore measured indirectly during the sputter process. Within this thesis, the temperature could only be assessed qualitatively but it was confirmed to rise when the contact area is reduced.

The production of thin films at elevated target temperatures was found to clearly enhance not only the thermochromic properties and thus the stabilization of vanadium dioxide but also the reproducibility. Further, an overall trend of increasing conductivity and smaller hysteresis width towards smaller contact areas between target and cooling system could be demonstrated.

The results of this thesis could open up promising opportunities for further research on the influence of the target temperature on the reactive sputter process and especially the production of high quality vanadium dioxide thin films.

## Zusammenfassung

Der Fokus dieser Diplomarbeit ist die Erzeugung von dünnen Vanadiumdioxid Schichten auf Glas mittels reaktivem DC Magnetronspütern bei verschiedenen Target-Temperaturen von 18 °C (volle Kühlung) bis etwa 700 °C. Vanadiumdioxid ist ein thermochromes Material, welches bei einer Temperatur von circa 68 °C einen Übergang von einer halbleitenden in eine metallische Phase erfährt (SMT). Die Kristallstruktur ändert sich dabei von monoklin zu tetragonal, wobei die elektrische Leitfähigkeit zunimmt und die Transmission im Infrarot-Bereich abnimmt. Bei dünnen Schichten ist der Übergang in die metallische Phase zumeist bei einer höheren Temperatur als der umgekehrte Prozess, was zur Ausbildung einer Hysterese führt. Es sind diese Eigenschaften, welche Vanadiumdioxid zu einem der interessantesten Materialien in der Halbleitertechnik und Dünnschicht-Technologie für Temperatur-gesteuerte Systeme werden ließ. Die Einsatzmöglichkeiten reichen von intelligenten Gläsern, welche bei einer bestimmten Temperatur ihre Transmission ändern über optische Schalter bis hin zu Speichergeräten. DC Magnetronspütern wiederum ist eine weithin gängige Methode zur Erzeugung hochwertiger, dünner Schichten in Industrie und Forschung.

Im Zuge dieser Arbeit wurde jedoch festgestellt, dass Vanadiumdioxid Schichten mittels reaktivem Magnetronspütern und bei voller Kühlung des Targets nur schwer herzustellen sind, da sich neben dem gewünschten Oxid verschiedene Vanadiumoxide mit ähnlicher Bindungsenthalpie bilden, welche den Phasenübergang behindern. Den zentralen Ansatz meiner Experimente stellte das schrittweise Erhöhen der Target-Temperatur, durch sukzessive Reduktion der Kontaktfläche zwischen Target und Kühlsystem dar. Dabei wurde die Auswirkung der Target-Temperatur auf den Sputter-Prozess und die Eigenschaften der Schichten untersucht. Aus diesem Grund war es erforderlich die Target-Temperatur zu bestimmen, was durch indirekte Messmethoden getan wurde. Die Messwerte stimmen qualitativ mit der erarbeiteten Theorie überein, wenn auch keine quantitativen Aussagen möglich waren.

Es zeigte sich, dass die Erhöhung der Target-Temperatur zu einer Verbesserung der Thermochromie sowie der Reproduzierbarkeit der Schichten führt. Die Auswertungen ergaben zudem einen Trend zu größeren Widerstandsänderungen und schmälere Hysteresen mit abnehmender Kontaktfläche.

Die Resultate dieser Arbeit stellen einen vielversprechenden Ansatz für weitere Forschungen dar, in welchen die Auswirkungen der Target-Temperatur auf den reaktiven Sputter-Prozess und insbesondere die Erzeugung hochwertiger Vanadiumdioxid Schichten fokussiert werden.

## Acknowledgement

I would like to thank the following persons and institutes for their support and assistance during my thesis:

First of all, my gratitude goes to Ao. Univ. Prof. Dr. Christoph Eisenmenger-Sittner for engaging me with the topic of this thesis. He encouraged me in developing new approaches and myself scientifically and opened up a great opportunity when he invited me to the 17<sup>th</sup> *JVC Vacuum Conference 2018* to present my findings.

I also warmly thank the *X-Ray Center* for always allocating time slots so that I could process my loads of samples in time. I especially thank Dipl. Ing. Werner Artner in this regard as he was often a helping hand during the evaluation of my diffractograms. I would also like to mention my colleagues from the *Thin Film Group* for the countless afternoons and evenings we spent together in the laboratory wondering about red blinking lights on the vacuum system, pondering about the outcome of our measurements and discussing our different interpretations of them.

Finally, I like to particularly thank my parents for enabling me to study physics and supporting me in any situation throughout the years.

# Contents

<b>1</b>	<b>Introduction</b>	<b>1</b>
<b>2</b>	<b>Theory</b>	<b>3</b>
2.1	Reactive DC Magnetron Sputtering . . . . .	3
2.1.1	Ion Sputtering . . . . .	3
2.1.2	DC Magnetron Sputtering . . . . .	5
2.1.3	Reactive DC Magnetron Sputtering . . . . .	6
2.2	The Oxidation States of Vanadium and their Physical Properties . . . . .	9
2.3	Current understanding of the Semiconductor to Metal Transition in $VO_2$	10
2.4	Current Developments in the Production of $VO_2$ Thin Films by DC Magnetron Sputtering . . . . .	15
2.5	Basics of Thin Growth . . . . .	18
2.6	Electrical Conductivity in Thin Films . . . . .	21
2.6.1	Four-Point Probe Method . . . . .	23
2.6.2	Measurement Setup . . . . .	23
2.6.3	Analysis of the Semiconductor to Metal Transition . . . . .	25
2.7	Principle of X-Ray Diffraction (grazing incidence) and Crystal Structures	26
2.7.1	Measurement Setup . . . . .	28
2.7.2	Analysis of Crystalline films on amorphous substrates in XRD .	29
2.8	Surface Analysis by Secondary Electron Microscopy . . . . .	29
2.8.1	Measurement Setup . . . . .	32
2.9	Optical Analysis by Fourier-Transform Infrared Spectroscopy (FTIR) .	33
2.9.1	Tauc Plots . . . . .	34
2.9.2	Measurement Setup . . . . .	35
<b>3</b>	<b>Experimental Setup of the Sputter System</b>	<b>36</b>
3.1	Sputtering System and Sample Preparation . . . . .	36
3.2	Digitizing an analog Pressure Sensor and Power Supply for Reactive DC Magnetron Sputtering . . . . .	38
<b>4</b>	<b>Target Temperature Calculation, Simulation and Measurement with Reduced Target Cooling</b>	<b>50</b>
4.1	Calculations of the Target Temperature in a 1D Model and Simulations	51
4.2	Indirect Measurement of the Target Surface Temperature and Modeling	55

<b>5</b>	<b>Analysis of as-deposited <math>VO_2</math> thin films produced by reactive DC magnetron sputtering</b>	<b>59</b>
5.1	Parameter Variation in reactive DC Magnetron Sputtering for as-deposited Crystalline $VO_2$ Thin Films . . . . .	60
5.1.1	Analysis of $VO_2$ Thin Films produced with full Target Cooling .	62
5.1.2	Analysis of $VO_2$ Thin Films produced with reduced Target Cooling	68
<b>6</b>	<b>Discussion</b>	<b>80</b>
<b>7</b>	<b>Conclusion and Outlook</b>	<b>86</b>
<b>8</b>	<b>Design Drawings</b>	<b>89</b>
<b>A</b>	<b>Appendix</b>	<b>104</b>
A.1	Berg Model . . . . .	104
A.2	Explanation of XRD and Laue Condition . . . . .	106
A.3	Explanation of SEM by Bethe-formula . . . . .	107
A.4	Simulations of Target Temperature by <i>Solidworks 2017</i> . . . . .	109
<b>B</b>	<b>Table of Measurements</b>	<b>112</b>

# 1 Introduction

The topic of this thesis is the production of vanadium dioxide ( $VO_2$ ) thin films on glass substrates by reactive DC magnetron sputtering.  $VO_2$  is a metal oxide, which exhibits a temperature driven transition from a semiconducting to a metallic phase (SMT) at about 68 °C (for single crystal bulk material) [1]. The reversible transition is driven by a rearrangement of the crystal from a monoclinic into a tetragonal structure. This rearrangement closes the bandgap of about 0.7 eV and leads to a change of its optical and electrical properties. The change of optical properties upon temperature variation is called thermochromism and is always accompanied by a distinct change in electrical properties such as electrical resistivity. For its particular physical properties,  $VO_2$  became an extensively studied material over the past 60 years. So far many interesting applications have been reported, such as infrared blocking thin films for smart windows [2], detector protection [3], bolometer [4], hydrogen nanosensors [5] or optical switching [6] and memory devices [7].

The physical properties of thin films are known to differ from the bulk behaviour and are therefore a great field of interest for manipulating and optimizing the properties of thermochromic materials, such as lowering the transition temperature or the formation of a hysteresis between the semiconductor-to-metal and metal-to-semiconductor phase. (Reactive) DC magnetron sputtering is a widely used and well-developed method for the production of thin films in research and industry. The production of  $VO_2$  thin films by reactive sputtering, however, was found to be challenging due to the coexistence of many different oxide states, which makes it difficult to control of the thin film composition even at minimal variations of the sputter parameters. Some authors claimed to have overcome this issue by either applying a bias voltage to the substrate during the deposition [8] or sputtering at high deposition power and post-deposition thermal annealing at temperatures of 300-550 °C under varying atmospheres [9, 10, 11]. Despite those approaches, a yet only rarely investigated but promising method for the modification of sputtered (oxide) thin films represents the variation of the temperature at the target surface during the sputter process [12]. The findings of A. Billard et al. [13] show that the target temperature has a direct influence on the reactive sputter process and thus the oxide composition. The controlled production of as-deposited  $VO_2$  thin films based on the temperature variation at the target surface sets the aim of this work and will clearly show to enhance the thermochromic properties of  $VO_2$  films.

This thesis is structured as follows. Chapter two presents the fundamentals of reactive

DC magnetron sputtering, thin film growth and physical properties. Further, the current theoretical understanding of the SMT in  $VO_2$  and developments in the production of such thin films is given, as well as the methods used for the analysis. In chapter three, the sputter system and its digitization during this work are explained. In chapter four the calculations and experimental attempts to measure the target temperature during the sputter deposition process are shown. Chapter five and six present the process and results for the production of vanadium oxide thin films at a constant target temperature of about  $18^\circ\text{C}$  and at variable target temperature up to approximately  $700^\circ\text{C}$ . An outlook for further studies on target temperature variation in the production of thermochromic thin films by reactive sputtering, based on the promising results found in this thesis, is given in chapter seven.

## 2 Theory

In this chapter, the fundamentals of reactive DC magnetron sputtering are explained for the production of vanadium dioxide thin films. A short overview of vanadium oxides showing a semiconductor to metal transition (SMT) is then given, followed by a quantum mechanical and thermodynamic derivation of the SMT in vanadium dioxide. Current developments in the production of vanadium dioxide thin films using DC magnetron sputtering are summarized. The thin films produced in this work were studied by four-point-probe measurements, x-ray diffraction, secondary electron microscopy and Fourier-transform infrared spectroscopy, of which a theoretical background and the detector setups used during this work are explained.

### 2.1 Reactive DC Magnetron Sputtering

The process of reactive DC magnetron sputtering is a special form of DC magnetron sputtering where a reactive gas is added to the system. DC magnetron sputtering in turn is based on the principle of ion sputtering. The three processes ion sputtering, DC magnetron sputtering and reactive DC magnetron sputtering are explained successively in the following. The reactive sputter process is also investigated using a simple kinetic approach called *Berg model* to understand the hysteresis behaviour shown by reactive sputter systems.

#### 2.1.1 Ion Sputtering

In general, ion sputtering is a deposition technique in which atoms are knocked out of a surface (target) by ions generated in a gas discharge (plasma). In order to do so, a high vacuum is generated inside a vacuum chamber. The chamber is then floated with an ionisation gas (helium, argon, neon) and a voltage is applied between the anode (deposition chamber) and the cathode (target), see fig. 1.

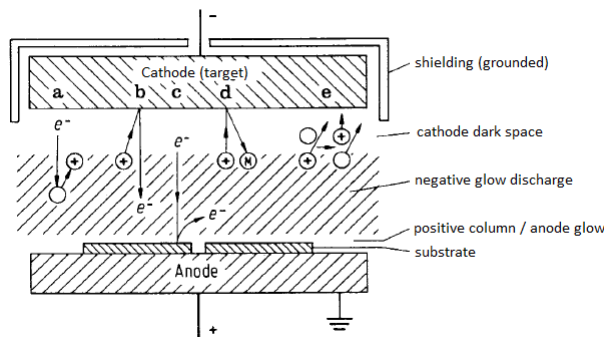


Figure 1: *Schematic of DC-Sputtering: (a) free electrons ionize the gas atoms which then accelerate to the target and (b) generate secondary electrons; (c) electrons accelerating onto the anode/substrate generate secondary electrons; (d) knock out neutral particles from the target or (e) neutralize by charge transfer, adapted from [14]*

Noble gases are used as ionisation gas because of their high ability to neutralize therefore being chemically inert. At relatively low voltages, free electrons are able to ionize the gas atoms and generate an electron cascade from the cathode to the anode. The ions accelerate onto the target and knock out atoms and secondary electrons or ionize other gas atoms near the cathode. The behaviour of a gas discharge at a fixed ionisation gas pressure is characterized by its voltage-current curve. Raising the current at low voltages leads to a fast rise of the voltage to high values but the free electrons are not fast enough to ionize the gas. As the voltage further rises the electrons and ions are fast enough to generate a charge avalanche and knock out electrons of cathode and anode leading to a voltage-breakdown. The ion density at the cathode rises till the entire cathode-surface is covered, which leads to a lowering of the voltage with rising current. Then the abnormal glow regime begins, where electrons are generated by strong ion impact. The strong impact leads to a heating of the cathode and thermally driven electron emission begins, leading to the arc-regime, where a further voltage-breakdown occurs. The regime in which ion sputtering is performed is the abnormal glow regime [15, 16]. The driving force in ion sputtering is impulse transfer between plasma ions and target atoms. The inversion of the impulse direction is caused by impulse transfer between the atoms close to the target surface. The sputter-yield  $Y$  is therefore characterized by the plasma ion kinetic energy  $E_{kin}^{ion}$ , the work function of the target material at the surface  $E_{bind}$ , and the mass-ratio  $\eta = \frac{M_{ion}}{M_{target}}$  of the ionized gas and target atoms. Furthermore, the sputter-yield depends on the incident angle of the plasma ions. For small angles (relative to the surface normal)  $Y$  rises with  $\cos^{-1}(\vartheta)$  but for large angles ( $\vartheta \rightarrow 90^\circ$ ) the

sputter yield decreases because of increasing reflections. The sputtering mechanisms may be classified into three regions [17, 18]:

- *Single-knock-on regime*:  $E_{kin}^{ion} < 10 \text{ eV}$  or/and  $M_{ion} \ll M_{target}$  then  $Y(E_{kin}^{ion}) \propto \frac{E_{kin}^{ion}}{E_{bind}}$
- *Linear-collision-cascade regime*:  $0.1 \text{ keV} < E_{kin}^{ion} < 10 \text{ keV}$  then  $Y(E_{kin}^{ion}) \propto \frac{4\eta}{(\eta+1)^2} \frac{E_{kin}^{ion}}{E_{bind}}$
- *Thermal-spike regime*:  $10 \text{ keV} < E_{kin}^{ion}$  then  $Y(T) \propto e^{-\frac{E_{bind}}{k_B T}}$

An illustration of the three regions is shown in *fig. 2*.

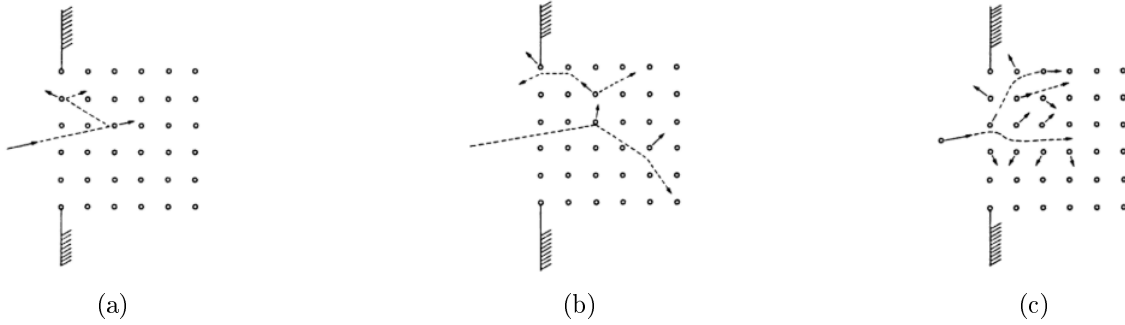


Figure 2: (a) *Single-knock-on regime*, penetration depth is in the order of  $\text{\AA}$  - nm; (b) *Linear-collision-cascade regime*: penetration depth is in the order of nm; (c): *Thermal-spike regime*,  $Y$  is mostly depending on the temperature near the surface, penetration depth exceeds the nm-region; adapted from [17]

99% of all sputtered atoms are neutral and therefore unaffected by the magnetic and electric fields inside the vacuum chamber.

### 2.1.2 DC Magnetron Sputtering

Magnetron sputtering is based on the Lorentz-force which traps the electrons at the target surface leading to a high electron and ion density. Therefore, a cooled magnetic system is installed behind the target of which an illustration is given in *fig. 3*.

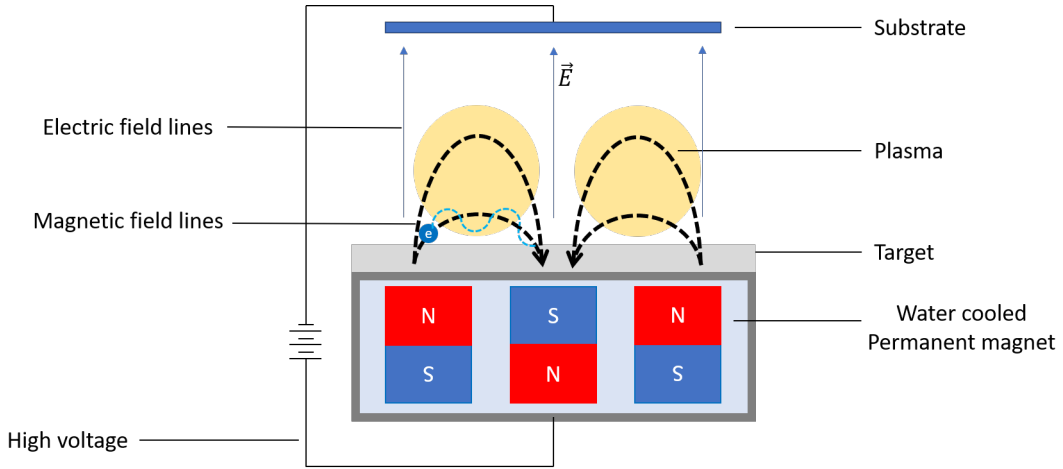


Figure 3: *Schematic of DC magnetron sputtering; the cooled magnets generate a magnetic field, due to the electric field, the electrons are forced on colloidal tracks leading to an increase of the ionisation probability, the plasma concentrates along the magnetic field lines near the target surface.*

The electric field  $\vec{E}$  between anode and cathode and the magnetic field  $\vec{B}$  are designed in a way that electrons emitted from the target by ion collision or electrons from the ionisation gas are forced onto a cycloidal path and loose energy (during the first loop) by collision with plasma ions. If so, the electron moves outwards onto the next cycloidal path and ionizes further gas atoms till it eventually reaches the anode, leading to an electron flux between cathode and anode and a flux in  $\vec{E} \times \vec{B}$  direction. The latter flux leads to an increase of the ionisation-probability and therefore the sputter-rate. The highest electron density occurs where the magnetic field lines are parallel to the target surface. Reactive gases can be added to the sputter system in which case a reactive magnetron sputter process eventually starts.

### 2.1.3 Reactive DC Magnetron Sputtering

Reactive sputter processes often show a hysteresis behaviour most commonly studied through either the voltage-current characteristic or the chamber pressure in dependence of the reactive gas flow (oxygen, nitrogen). Two typical hysteresis curves taken from this work by means of pressure and flow rate are shown in fig. 4.

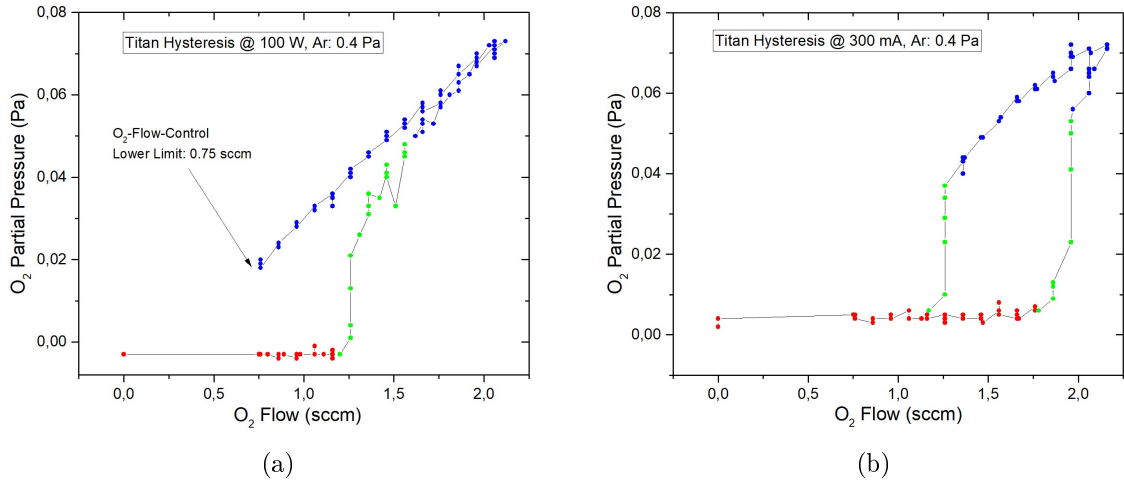


Figure 4: (a) *Hysteresis of titanium at a fixed power level of 100 W power and (b) of titanium at a fixed current of 300 mA, both at an argon pressure of 0.4 Pa; The red dotted areas represent the metallic regions and the green ones the transition regions; the transition occurs abrupt but not instantly as the measured points in this region indicate; blue regions show the poisoned region where mainly oxide compounds form at the target surface; the oxygen flow controller is limited to  $>0.75$  sccm which is why the hysteresis in (a) stops at this point.*

As can be seen, the flow rate does not change the oxygen partial pressure at flow rates along the red dotted lines, this marks the metallic mode. Along the green dotted lines the unstable region appears and the oxygen partial pressure drastically increases. At the onset of the blue lines no further abrupt changes occur as long as only one target and one reactive gas are used and the so called poisoned mode begins. At this point the target surface (at which the plasma tube forms) is fully covered by compounds and oxygen impurities. By decreasing the flow rate into the instable region again, the pressure remains linear and the target remains poisoned. A second point shows up at which the pressure decreases abruptly and the poisoned mode ends, thus the target surface becomes mostly metallic again. To explain the behaviour of a reactive sputter process which not only exhibits a high sensitivity against the reactive gas flow but in certain flow regions also shows instabilities, it is important to treat the process kinetically. For this purpose, the so called Berg model by S. Berg et al. [19, 20] was proposed. The model and the simulation methods are explained in detail in the appendix A.1. A simulation with arbitrary values and oxygen as reactive gas is given in fig. 5 to show the qualitative behaviour of the oxygen partial pressure and poisoning of the target surface in dependence of the oxygen flow.

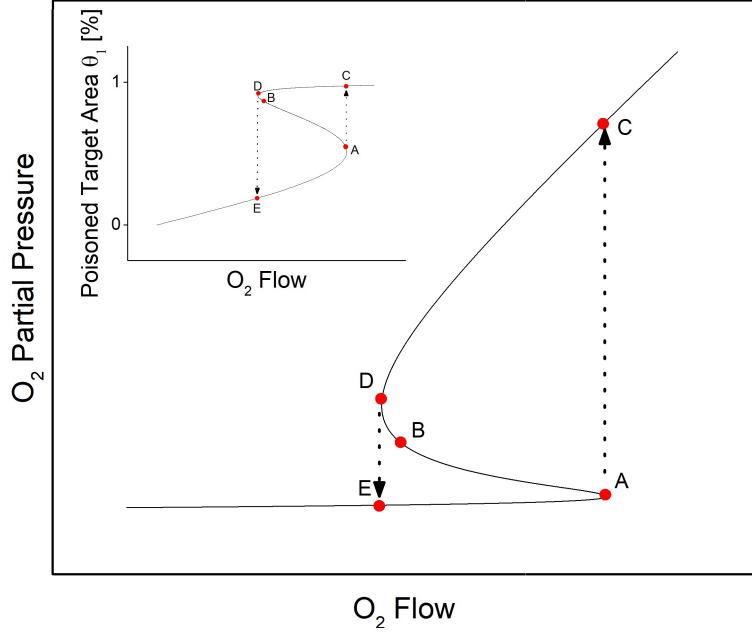


Figure 5: *Simulation according to the Berg model. The inset shows the corresponding course of the target poisoning in dependence of the flow. The region through E to A marks the metallic mode. As can be seen from the inset, the target is already partially poisoned ( $\simeq 0.5$  of total area) at A. The course ABDC is unstable and leads to the straight increase of partial pressure from A to C and target poisoning to nearly 1. A further increase above C is already in the saturated region where no additional oxygen consumption takes place. Going back through DBAE is also unfavoured and results in a second straight downfall of the partial pressure from D to E and a decrease of target poisoning to around 0.15. The parameters used for the simulations according to the nomenclature in the appendix are  $S = 100 \frac{\text{l}}{\text{s}}$ ,  $\alpha_t = \alpha_c = 0.3$ ,  $A_t = 10^{-3} \text{ m}^2$ ,  $A_c = 10 \cdot A_t$ ,  $Y_t = 1$ ,  $Y_c = 0.1 \frac{\text{mA}}{\text{cm}^2}$ ,  $J = 0.1$ ,  $T = 300 \text{ K}$ .*

As can be seen, through E to A the oxygen partial pressure does not increase but the fraction of the poisoned target surface increases to about half of the target surface. The region from A to B is unstable and therefore the oxygen partial pressure and the poisoned fraction of the target surface quickly increases towards C directly in most cases. At C the target is fully poisoned, thus the surface is covered with compounds and reactive gas atoms which lowers the sputter yield as the voltage and consequently the ion current is diminished by the insulating layer. Further, the surface binding energy of most metal oxides exceeds the metallic one and as a result further lowers the sputter yield. As the target is saturated at this point, a further increase in oxygen flow leads to a linear increase in pressure. By decreasing again to D the instability of DBAE leads

to a quick drop of partial pressure from D to E in most cases lowering the poisoned fraction of the target surface by about eighty percent following the simulation results. The hysteresis is therefore given by the trapezoid ACDE.

## 2.2 The Oxidation States of Vanadium and their Physical Properties

Vanadium is a transition metal and has the noble-gas electron configuration  $[Ar]3d^34s^2$  [21] and an atomic number of 23. When vanadium oxidizes it forms various semiconducting configurations which may be described by the following three formulas [22]:

- $V_nO_{2n+1}$ : e.g.  $V_2O_5$ ,  $V_4O_9$ ,  $V_6O_{13}$
- $V_nO_{2n-1}$ : e.g.  $V_2O_3$ ,  $V_3O_5$
- $V_nO_{2n}$ : e.g.  $VO_2$ ,  $V_2O_4$

Besides, semiconductor to metal transitions (SMT) can be observed in multiple oxidation states of vanadium. Vanadium oxides showing a SMT are given in table 1 together with their transition temperature in the heating process  $T_{c\uparrow}$  at ambient pressure and their respective bandgaps in the semiconducting state [23, 24].

Oxide	$T_{c\uparrow}$ [K] at amb. press.	bandgap [eV]	Ref.
$VO_2$	340	0.7	[1, 24]
$V_2O_3$	153	0.66	[1, 25]
$V_3O_5$	428	0.99	[26, 27, 28, 29, 30]
$V_4O_7$	250	0.58	[24, 31, 32, 33]
$V_5O_9$	135	0.76	[24, 34, 35]
$V_6O_{11}$	177	0.45	[36, 24]
$V_8O_{15}$	70	0.54	[24, 37, 38]

Table 1: *The transition temperature  $T_{c\uparrow}$  in the heating cycle of different vanadium oxides with a thermochromic behaviour and the respective bandgap in the semiconducting state*

Fig. 6 shows the corresponding SMT of the phases in comparison as a function of the inverse temperature.

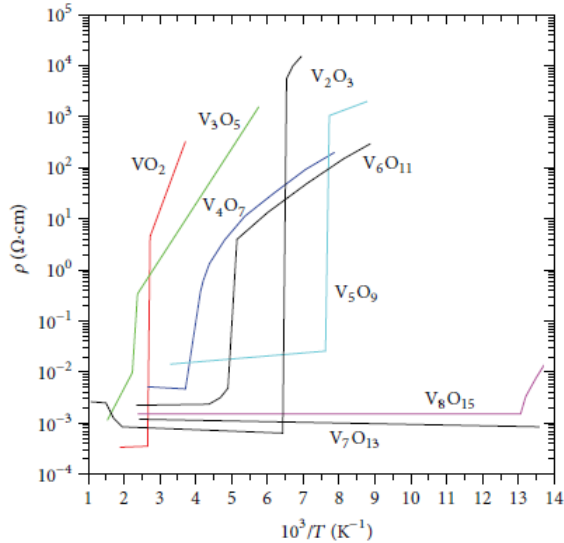


Figure 6: Comparison of semiconductor to metal transitions in various vanadium oxides in terms of the resistivity as a function of the inverse temperature. The corresponding transition temperatures and bandgaps in the semiconducting state are given in table 1 [23].

It should be noted that current studies are performed on a SMT in  $V_2O_5$  [39] which are assigned to a loss of oxygen and thus a formation of other oxide states like  $V_2O_3$  and  $V_6O_{13}$ . It is therefore not a SMT in the classical sense. For example the mixing of  $VO_2$  and  $V_2O_3$  would yield a SMT at 153K thus being at least partially metallic before the onset of  $VO_2$  at around 340 K. For a certain use as thermoelectric device it is of utmost importance to exactly control the composition or rather the purity of the oxide to obtain a well defined transition temperature.

### 2.3 Current understanding of the Semiconductor to Metal Transition in $VO_2$

The investigation of the SMT of  $VO_2$  began in the 1950s [1] and forms a rich field of discussion since then about the origin of the transition behaviour. To understand the current theory a short overview of the contributions which lead to SMT is given in the following.  $VO_2$  forms a monoclinic dimerized (V-V) crystal structure [40] below the critical temperature of the SMT around  $T_{crit} = 68^\circ\text{C}$  in bulk. The vanadium dimers form zigzag chains with unequal spacing along the c-axis. The distance between vanadium atoms of a dimer is about  $2.6\text{ \AA}$  and between the dimers about  $3.2\text{ \AA}$  [41].

The distance between the dimers is too big for the d-orbitals of the vanadium atoms to share their electrons. The critical distance to overcome this was estimated by J.B. Goodenough [40] to be 2.94 Å. Above the critical temperature the structure rearranges to a tetragonal lattice where the vanadium atoms are separated equally along the c-axis by about 2.88 Å which is close enough for the d-orbitals to interact and share their electrons. An illustration of the monoclinic and tetragonal structure of  $VO_2$  is given in fig. 7, together with a schematic of the rearrangement taking place during the SMT.

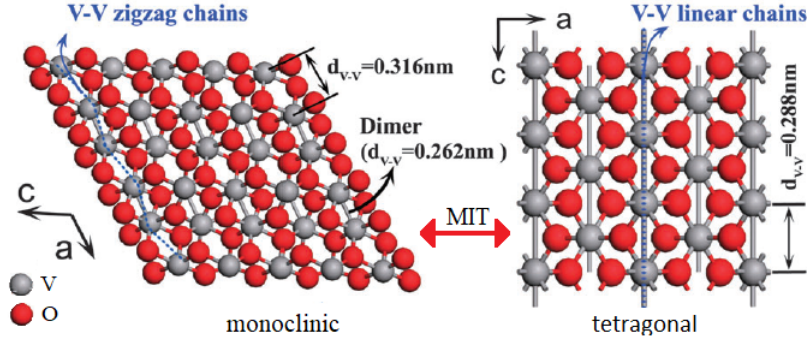


Figure 7: *Semiconductor to metal transition between the semiconducting monoclinic and the conductive tetragonal structure of  $VO_2$ . In the monoclinic phase the vanadium ions form dimer bonds with a intermediate distance of 2.62 Å and 3.16 Å between the dimers which hinders the electrons from moving freely along the c-axis. The dimers form a zig-zag chain along the c-axis. In the tetragonal phase the distance between the dimers shortens to 2.88 Å allowing the electrons to move freely in the c-axis direction. The entropy of the phonons stabilizes the tetragonal, conducting phase; adapted from [41]*

Significant contributions to the explanations of SMT came from N.F.Mott [42], R. Peierls [43], P.W. Anderson [44] and J. Hubbard [45]. The structural changes in most SMT are described by electron-electron interactions leading to Mott transitions and electron-phonon interactions leading to Peierls transitions. In a simple one-dimensional approach the two effects are modeled by the Holstein-Hubbard model [46, 47]:

$$\hat{H}_{HH} = - \underbrace{\sum_{\langle i,j \rangle, \sigma=\downarrow\uparrow} t_{ij} \cdot \hat{c}_{i\sigma}^\dagger \hat{c}_{j\sigma}}_{\hat{H}_{tb}} + \omega_0 \cdot \underbrace{\sum_i \hat{b}_i^\dagger \hat{b}_i}_{\hat{H}_p} - g \cdot \omega_0 \cdot \underbrace{\sum_{i, \sigma=\downarrow\uparrow} (\hat{b}_i^\dagger + \hat{b}_i) \cdot \hat{n}_{i\sigma}}_{\hat{H}_{ep}} + U \cdot \underbrace{\sum_i \hat{n}_{i\uparrow} \hat{n}_{i\downarrow}}_{\hat{H}_{ee}} \quad (1)$$

This hamiltonian contains the necessary interactions between electrons and phonons to

investigate phase transitions. The term  $\hat{H}_{tb}$  is simply the total energy of electrons in the tight-binding approximation with the hopping integral  $t_{ij}$  between nearest neighbors, where  $\hat{c}_{i\sigma}^\dagger$  denotes the creation operator for an electron at position  $i$  with spin  $\sigma$  and  $\hat{c}_{j\sigma}$  the annihilation of the respective electron at site  $j$ . The term  $\hat{H}_p$  denotes the total energy of the phonons with a certain frequency, where  $\hat{b}_i^\dagger$  describes the creation and  $b_i$  the annihilation of a phonon at site  $i$  so that they together form the “number-of-particles” operator  $\hat{n}_i = \hat{b}_i^\dagger \hat{b}_i$ . The term  $\hat{H}_{ep}$  describes the scattering of an electron by either creation  $\hat{b}_i^\dagger \hat{n}_{i\sigma}$  or annihilation  $\hat{b}_i \hat{n}_{i\sigma}$  of a phonon with frequency  $\omega_0$ . The parameter  $g$  contains the coupling strength between electrons and phonons.  $\hat{H}_{ep}$  thus describes the Peierls-like transitions. These transitions occur when the distortion of the lattice favours the formation of an electronic band gap lowering the energy by a bigger amount than the distortion needs. Similarly, the term  $\hat{H}_{ee}$  contains the repulsion of electrons at a certain point  $i$  in the lattice with different spins and therefore accounts for the Mott-like transitions. The parameter  $U$  is the repulsion strength. Mott transitions are favoured when two electrons of opposite spin could by the Pauli principle be at the same position but due to their repulsion get energetically separated which opens up a bandgap, trapping the electrons close to their atoms. At higher temperatures these effects can be overcome and a transition from an insulator to a metal occurs. In fig. 8 a schematic of the processes and the resulting phases is given.

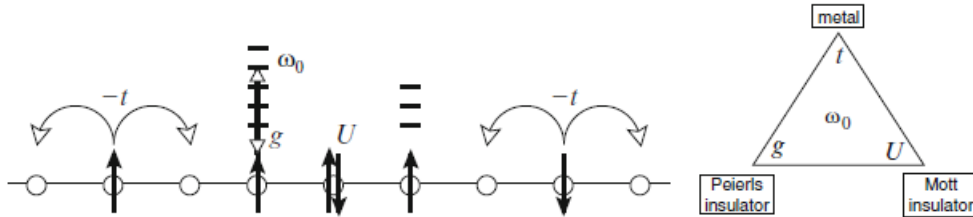


Figure 8: *Schematic illustration of the terms in the Holstein-Hubbard hamiltonian in eq. 1. The hopping integral  $t$  gives the respective overlap of the nearest neighbour atomic orbitals in the tight binding approximation. The term  $g$  accounts for the electron-phonon interaction, the closer the electrons are localized to the ions the smaller  $g$  gets. The Peierls transition occurs when a distortion of the lattice leads to an overweight of electronic energy lowering. The  $U$ -term denotes the electron-electron interaction. Two electrons at the same site and thus with opposite spin experience a repulsive force which leads to the splitting of the band, forming a Mott insulator.*

The Holstein-Hubbard model is designed in a way that it only accounts for dispersionless phonons corresponding to optical phonons or in other words the Einstein approximation

for the phonon density of states (PDOS)  $g$ . For a treatment of acoustic phonons one has to deal with the Su-Schrieffer-Heeger model [48]. In most cases the phonons are treated in a harmonic or quasi harmonic limit. This means that the elastic forces between the ions follow Hooke's law  $\vec{F} = k \cdot \delta\vec{x}$  where  $k$  is the elastic force constant and  $\delta\vec{x}$  a rather small deviation from the equilibrium position. The quasi harmonic approximation considers Hooke's law as valid but allows a pressure or temperature dependence of the spring constant  $\delta k(p, T)$  so that  $\vec{F} = (k + \delta k(p, T)) \cdot \delta\vec{x}$ . When the quasi-harmonic approximation does not hold anymore higher order terms in the forces between the ions must be involved so that  $F = k_1 \cdot \delta x + k_2 \cdot \delta x^2 + k_3 \cdot \delta x^3 + \dots$ . The higher order terms stand for the phonon-phonon interactions and are described as phonon scattering. The quasi harmonic case can be visualized by a set of one dimensional springs. When temperature is applied to the system, the volume expands and so do the distances between the springs which leads to a decrease of the elastic force constant, the parabolic energy potential becomes flatter and the phonons reduced in frequency which are then said to be softened. Pressure or cooling in turn decreases the distance between the springs and increases  $k$ , which leads to the inverse process of phonon-stiffening. The strong anharmonic effects must be included when the deviation from the harmonic behaviour and thus the phonon-phonon interaction becomes large. The anharmonic effects in either the Holstein-Hubberd or the Su-Schrieffer-Heeger model lead to a shift in the phonon frequency  $\omega = \omega_{ham} + \Delta\omega_{anh} + i\Gamma$  (also called renormalized frequency) and thus the PDOS  $g(\omega) = g(\omega_{ham} + \Delta\omega_{anh} + i\Gamma)$  where  $\Delta\omega_{anh}$  accounts for the frequency shift and  $i\Gamma$  for the damping of the individual phonons due to scattering. The treatment of this in perturbation theory would exceed the scope of this work.

The key message is to account on the one hand for the electronic interactions (electron-electron and electron-phonon) and on the other hand for the phonon interactions (phonon-phonon) in the analysis of SMT. To understand the dynamics of thermal processes leading to SMT the hamiltonian has to be identified with the total internal energy of a crystal. The internal energy of a system  $U$  in a quantum mechanical manner is connected to the hamiltonian via the thermodynamic density operator  $\hat{\rho}_T$  [49]:

$$\begin{aligned}
 U &= Tr \left( \hat{\rho}_T \cdot \hat{H} \right) \\
 \hat{\rho}_T &= Tr \left( e^{-\frac{\hat{H}}{k_B T}} \right)^{-1} \cdot e^{-\frac{\hat{H}}{k_B T}}
 \end{aligned} \tag{2}$$

The internal energy is a thermodynamic potential depending on entropy and volume<sup>1</sup>,  $U(S, V)$  so that<sup>2</sup>:

$$\frac{dU}{dT} = T \cdot \frac{\partial S}{\partial T} - p \cdot \frac{\partial V}{\partial T} = \left( T \cdot \frac{\partial}{\partial T} + p \cdot \frac{\partial}{\partial p} \right) S \quad (3)$$

By heating the sample, the entropy increases leading to an increase of internal energy. Only when a change in entropy at some point enables a change in internal energy  $dU < -dS < 0$  (e.g. by electron phonon interactions) a stabilization of the system can be achieved. As the entropy is an additive quantity it is possible to divide it into the respective contributions like phononic and electronic ones  $S = S_{el} + S_{ph} + \dots$  which are in turn in a statistical way connected to the occupation factors  $f$  and density of states  $g$  by<sup>3</sup>: [50]

$$\begin{aligned} S_{ph} &= 3k_B\hbar \int_0^{\omega_{max}} [(f_{ph} + 1) \cdot \ln(1 + f_{ph}) - f_{ph} \cdot \ln(f_{ph})] \cdot g_{ph}(\omega) d\omega \\ S_{el} &= k_B\hbar \int_{-\infty}^{\infty} [(f_{el} - 1) \cdot \ln(1 - f_{el}) + f_{el} \cdot \ln(f_{el})] \cdot g_{el}(\omega) d\omega \\ S_{tot} &= S_{el} + S_{ph} + (S_{mag} + etc.) \end{aligned} \quad (4)$$

By measuring the EDOS, PDOS in dependency of the temperature throughout the phase transition the contributions to the total entropy change of the individual (quasi) particles can be quantified.

In the case of vanadium dioxide a recent paper by A.L. Pergament [23] discussed in detail the trouble of assigning the SMT to either the Mott or Peierls interactions. In 2014 J.D. Budai et al. published a breakthrough in this regard [50]. They revealed, mostly by inelastic neutron scattering the contributions of lattice vibrations to the stabilization of the metallic phase in the  $VO_2$  SMT, measuring the phonon entropy to change by  $\Delta S_{ph} = 0.34 \pm 0.03 k_B \cdot atom^{-1}$  obtained from the PDOS. This entropy change contributes with about two thirds to the total entropy change  $\Delta S_{tot} = 0.5 \pm 0.05 k_B \cdot atom^{-1}$ . Therefore the electronic contribution could be estimated by  $\Delta S_{el} \leq \frac{1}{3} \Delta S_{tot}$  as other contributions like magnetic ones must be taken into account. Acoustic, soft phonons which can be described harmonically in the semiconducting monoclinic phase become strongly anharmonic during the phase transition. This anharmonicity upon heating leads to the overcome of electronic energy leading to an overlap of the d-orbitals along the c-axis, changing the electronic bonds, forming a conduction band. The  $d_{x^2-y^2}$  were

---

<sup>1</sup> Assuming a constant number of particles inside the system

<sup>2</sup> From the Maxwell relations follows  $\frac{\partial V}{\partial T} \Big|_p = - \frac{\partial S}{\partial p} \Big|_T$

<sup>3</sup> Assuming a constant  $f_{ph} = \left( e^{\frac{\hbar\omega}{k_B T}} - 1 \right)^{-1}$  and  $f_{el} = \left( e^{\frac{\hbar\omega}{k_B T}} + 1 \right)^{-1}$



In addition, the region of films containing crystalline  $VO_2$  extended only over a small pressure range between 0.08 Pa and 0.081 Pa (corresponding to a ratio of oxygen to argon of 0.3) with a slight stabilization at higher substrate temperatures. Beside the dioxide being present at this small pressure range another phase  $V_6O_{11}$  showing itself a semiconductor to metal transition (SMT) is present at around 0.08 Pa. They further found the sputter yield of a fully poisoned target to decrease by a factor of 10 relative to the metallic phase which is important for simulations as performed in section 2.1.3 using the Berg model (see appendix A.1). The measured yields for metallic vanadium was found to be  $Y_V = 0.53$  and  $Y_{VO} = 0.05$  per 500 eV argon ion. The paper reports the production of thin films at 400 °C substrate temperature in the mentioned region of oxygen partial pressure showing a resistivity change of up to  $r_{IM} = 6 \cdot 10^3$  and a hysteresis width  $\Delta T_H = 2 - 3^\circ C$  while the transition temperature in the heating cycle was found to be around  $T_{trans} = 67^\circ C$ . However, the paper does not quantify the reproducibility of the samples.

Sihai Chen et al. [10] produced films at a sputter power of 374 W and an argon flow of 145 to 175 sccm while the oxygen flow was held between 18 and 25 sccm. This corresponds to a ratio of oxygen to argon between 0.1 and 0.17. A silicon substrate with a 200-300 nm buffer layer of  $Si_3N_4$  was used and the temperature was kept at 200 to 250 °C. The samples were studied before and after a thermal annealing at 400 to 475 °C for one hour under constant argon flow. They concluded that a SMT could not be detected before annealing but afterwards a resistivity drop of two orders of magnitude could be observed at 68 °C. The as deposited oxide films were found to be tetragonal  $VO_2$  at room temperature and only after annealing the dimerisation of vanadium took place to form monoclinic  $VO_2$ . The surface structure of the as deposited vanadium films had fine nano-structured grains which start to form an even surface of monoclinic crystallites after annealing. The thermochromic properties of the annealed films at 475° C are not mentioned in the papers but were estimated from the shown graphs with a resistivity change  $r_{IM} \cong 200$ , a hysteresis width  $\Delta T_H \cong 6^\circ C$  at a transition temperature in the heating cycle  $T_{trans} \cong 68^\circ C$ .

Dong-ping Zhang et al. [8] have found monoclinic  $VO_2$  to form at a fixed argon flow of 40 sccm and oxygen flow of 1.6 sccm which equals a ratio of 0.04 and a sputter power of 110 W at a substrate temperature of 200 °C and a bias voltage of -160 V without further thermal annealing on glass substrates. This outcome would show that sputtering is a possible way to coat temperature-sensitive materials. The polycrystalline  $VO_2$  films showed a SMT at  $T_{trans} \cong 56^\circ C$ , at a hysteresis width of  $\Delta T_H \cong 12^\circ C$  and a resistivity

change of  $r_{IM} \cong 20$ . An indirect optical bandgap of 0.69 eV was estimated by a Tauc-plot of optical FTIR measurements. However, during the project work of M. Zeiner [52] at this institute using the same power settings, substrate temperature and bias voltage and a varying low ratio of oxygen to argon content, no films could be deposited containing  $VO_2$  but mostly  $V_2O_5$ . As we do not doubt the validity of the results by Dong-ping Zhang et al. we concluded that the production at this settings must be very sensitive to the chamber geometry and position of the oxygen inlet.

A paper of V. Melnik et al. [11] even produced thin films at 70 W sputter power at a substrate temperature of 200 °C and a ratio of oxygen to argon flow of 0.05. The films were post annealed at 300 °C in atmospheric conditions. The annealing process changed the films from amorphous to polycrystalline  $VO_2$  measured by XRD analysis. The resistivity changed after annealing by up to  $r_{IM} = 10^2 - 10^3$  at a transition temperature  $T_{trans} = 58^\circ C$ . While the hysteresis width was not mentioned in the text, it was estimated from the graphs to be  $\Delta T_H \cong 5^\circ C$ . These measurements were also reproduced during this work, but none of the samples came close to the proposed properties of the paper.

Shu-Yi Li et al. [53] produced thin nano rods of  $VO_2$  at a sputter power of 172 W , an argon flow of 1.33 sccm and an oxygen flow 0.083 sccm corresponding to a ratio of 0.06. The glass substrates were heated between 450 °C and 550 °C during the deposition. Before starting the oxide growth a thin gold layer was deposited as a seed layer. The structure and growth of the oxide films was then changed by controlling the direction and position at which the oxygen enters the chamber. Therefore, a ring-like tube with holes for the outlet of oxygen was placed atop the glass sample. The paper could show significant structural changes of the films in dependence of the direction of the oxygen gas inlet. On the one hand, this shows the sensibility of reactive sputter systems to not only the oxygen content but also the way it flows through the chamber and across the substrate and the target. On the other hand it opens up a method for the controlled production of nano-structured, crystalline  $VO_2$  films. The films were not investigated electrically by the authors.

A. Billard et al. [13] did reactive sputter experiments on titanium in a mixed argon/oxygen and argon/nitrogen atmosphere. The transition region from the metallic into the poisoned mode stabilized upon heating the target to around 1155 K (observed by the phase transition of titanium from hcp to bcc  $\alpha$ -Ti) and thus a rise in the metallic content of the sputtered compounds. The reactive sputter hysteresis measurements were carried out at an argon pressure of 0.3 Pa and 0.4 Pa for oxygen and nitrogen

as reactive gas respectively, while the current was initially set to 0.5 A for both. Upon heating the current increased to about 0.65-07 A in steady state conditions. By using the Berg model and adapting it to account for temperature driven diffusion of oxidic compounds at the target surface by a Crank-Nicholson method, they could show that the oxygen/nitrogen content of the first (three) monolayers decreases with increasing target temperature.

However, no current papers on the effect of target heating on the production and stability of  $VO_2$  films by DC magnetron sputtering could be found.

## 2.5 Basics of Thin Growth

Sputtered particles are either reflected from the substrate or they diffuse along the surface and eventually desorb again. The desorption and diffusion rate depend on the phonon frequency  $\nu_0$  of the substrate, the binding or adsorption energy  $E_{ad}$  (1 – 2 eV) and the substrate-temperature  $T_s$ . The Boltzmann factor gives the fraction of particles which desorb from the surface in dependence of the substrate temperature and adsorption energy by  $e^{-E_{ad}/k_B T_s}$ . The rate of desorption from the surface  $r_{des}$  in turn is connected to the Boltzmann factor and the phonon frequency by [54, 55]:

$$r_{des} = \nu_0 \cdot e^{-E_{ad}/k_B T_s} \quad (5)$$

The potential-barrier  $E_{pb}$  limits the mobility of the adsorbed particles. The probability for an adsorbed particle to leave a local minimum of the potential energy surface is given by  $e^{-E_{pb}/k_B T_s}$ . The mean distance  $l(t)$  a particle travels across the surface during the time  $t$  is given by<sup>4</sup> [56]:

$$l(t) = a \cdot e^{-E_{pb}/2k_B T_s} \cdot \sqrt{\nu_0 \cdot t} \quad (6)$$

The layer growth and adhesion to the substrate is therefore dependent on the occurrence and formation of minima in the potential energy surface. One adsorbed particle is called a monomer and an aggregate of monomers forms a nucleus. Nucleation either occurs at lattice-defects or by accumulations of adsorbed particles. Nucleation itself is separated

---

<sup>4</sup>Assuming the particle to move randomly across the surface, the traveled distance  $l$  of a particle can be described by a Brownian motion. The number of jumps of a particle  $\langle N(t) \rangle \cong \langle \frac{dN}{dt} \rangle \cdot t = \nu_0 \cdot e^{-E_{pb}/k_B T_s} \cdot t$  after a time  $t$  and the approximated mean square step size  $a^2$  per jump are thereby proportional to the mean square displacement of the particle from its initial position  $\langle \Delta x^2(t) \rangle = N(t) \cdot a^2$  and by  $l(t) = \sqrt{\langle \Delta x^2(t) \rangle}$  follows eq. 6

into three phases [14, 56]:

1. the accumulation of monomers to subcritical nuclei. The compound of the monomers is unstable and can easily decay.
2. When subcritical nuclei grow instead of decaying, a critical, stable nucleus forms. This happens if the surface to volume ratio becomes energetically favorable.
3. The critical nucleus can then further grow to form a hypercritical nucleus or a stable island. Thereby the nucleus grows and absorbs monomers close by.

When stable islands reach a certain size coalescence starts. Depending on the substrate temperature, they rearrange and minimize their lateral extent by surface energy minimization. This leads to empty spaces in between them where secondary nucleation and diffusion take place. In this process the islands further grow forming at first channels and then holes in between which is followed by the formation of a continuous layer. For an illustration of these steps see fig. 10.

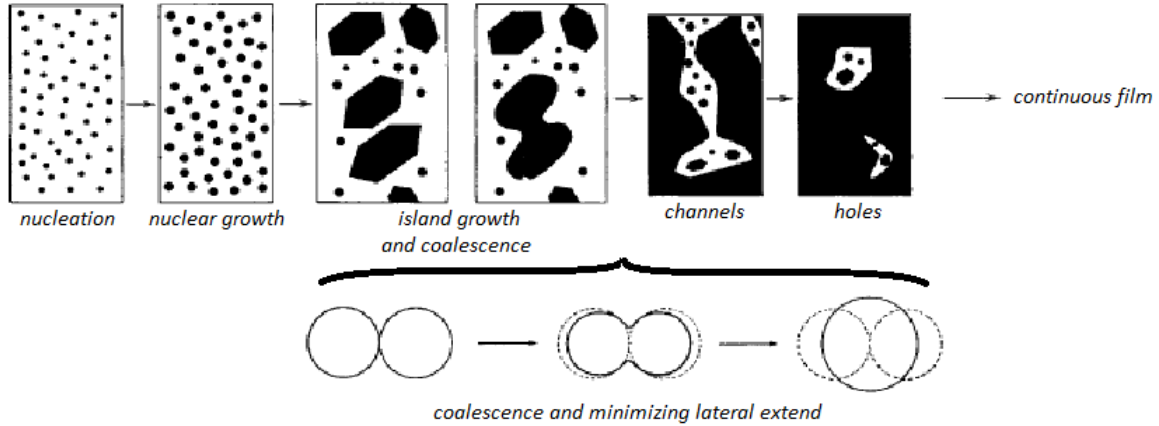


Figure 10: *Nucleation starts with subcritical nuclei which at a certain point form energetically favourable stable nuclei; The nuclei further merge to form islands which then coalesce to minimize their extension; secondary nucleation takes place inbetween, first channels and then holes remain until a continuous film forms; adapted from [57]*

For a good adhesion of the layer to the substrate the structure of the layer is important. The structure is classified by the empirically derived Thornton-model [58], shown in fig. 11. It describes the layer growth of DC sputtered elemental or single phase films in dependence of the argon gas pressure and the substrate temperature  $T$  compared to the melting point of the layer material  $T_m$ .

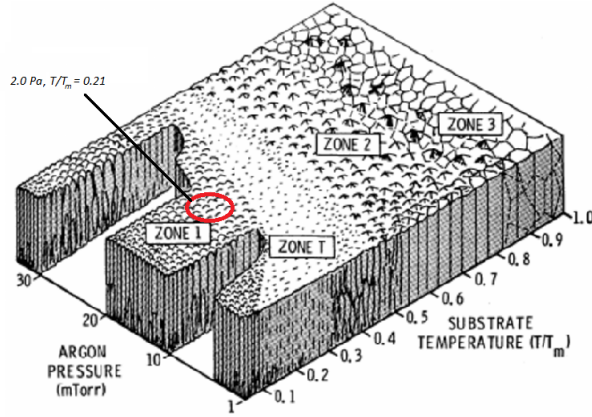


Figure 11: *Thornton's zone diagram: gives a schematic view of the film structure in dependence of the substrate temperature  $T$  compared to the melting point of the material  $T_m$  (for  $VO_2$ :  $T_m = 2243$  K) and the chamber pressure (the red circle shows the corresponding regions for a substrate temperature of  $T = 673$  K and an argon pressure of  $p_{Ar} = 2.0$  Pa as used for the reduced target cooling experiments performed in this work [59])*

Zone 1 describes a region of low diffusion rates and thus a porous structure and long, cone-like crystallites. In Zone 2 porosity decreases by an increase of surface diffusion. The structure becomes fibrous and denser and mostly columnar crystallites form. In Zone 3 the diffusion of defects and atoms inside the crystal structure starts and the so called re-crystallization begins, forming a highly dense structure. Besides the substrate temperature and the gas pressure the layer growth can be further influenced by ion bombardment. In order to do so, the substrate is set to a negative potential (bias)  $U_{BIAS}$ , which in turn leads to the impact of ionized gas atoms. The ions on the one hand heat up the surface thus facilitating diffusion and on the other hand knock out atoms from the forming layer which leads to defects. An intrinsic influence on the layer growth and adhesion to the substrate arises from stresses. Besides internal stresses there are also thermal stress which mostly occur at the interface of crystallites and in between the layer and the substrate due to different thermal expansion. The thermal stress can be minimized by cooling down the substrate slowly to room temperature past deposition. A quick cooling could lead to cracks in the layer and a detachment from the substrate.

## 2.6 Electrical Conductivity in Thin Films

The electrical conductivity of metal thin films is described in a quantum mechanical manner by the Fuchs-Sondheimer-model (FS model). For a detailed treatment of the FS model see [60, 61] However, the contributions to the electrical conductivity in thin films is calculated by a classical approach used by J.J. Thomson [62]. In order to do so, Matthiessen's rule is used, which states that the total resistivity  $\rho_T$  of a material is simply the sum of resistivities due to different scattering contributions  $\rho_i$  and because the resistivity is indirectly proportional to the mean free path of the charge carrier  $\rho_i \propto \lambda_i^{-1}$  the inverse total mean free path of a charge carrier inside a medium is given by<sup>5</sup>:

$$\lambda_T^{-1} = \sum_i \lambda_i^{-1} \quad (7)$$

The main scattering contributions to the resistivity in metals are [63]:

- scattering of electrons at phonons which temperature dependence is described by the Wiedemann-Franz-law at known thermal conductivity  $\kappa$  to be  $\lambda_{Th} \propto \frac{L}{\kappa} \cdot T$  where  $L$  denotes the Wiedemann-Franz constant
- scattering at impurities  $\lambda_I$
- scattering at defects  $\lambda_D$

Especially in thin films where  $\lambda_T$  can be smaller than the film thickness  $d_S$  or the grain size  $d_G$ , two main contributions must be added:

- scattering at the surface  $\lambda_S$
- scattering at grain boundaries  $\lambda_G$

Both scattering effects are of diffusive and specular kind. If one considers an electron to move inside a thin film which is only limited by the films thickness and can move with the mean free path of the bulk  $\lambda_T^b$  in the plane, the only additive scattering mechanism would occur at the interfaces between both, substrate and ambient. This leads by simple geometrical considerations and for films much thinner than the mean free path of the bulk material  $d_S \ll \lambda_T^b$  to a mean free path for a thin film  $\lambda_T^{tf}$  of [61]:

---

<sup>5</sup> $\rho_T = \sum_i \rho_i \propto \sum_i \lambda_i^{-1} := \lambda_T^{-1}$

$$\lambda_T^{tf} = \lambda_T^b \cdot \frac{t}{2} \cdot \left( \ln \left( \frac{1}{t} \right) + \frac{3}{2} \right) \quad (8)$$

Here,  $t = \frac{d_S}{\lambda_T^b}$  describes the ratio between the film thickness and the bulk mean free path, which in turn leads to a ratio of the bulk to the thin film resistivity of:

$$\frac{\rho_T^b}{\rho_T^{tf}} = \frac{\lambda_T^{tf}}{\lambda_T^b} = \frac{t}{2} \cdot \left( \ln \left( \frac{1}{t} \right) + \frac{3}{2} \right) \quad (9)$$

For  $t < 1$  eq. 9 shows a fast increasing behaviour as one would expect. The Fuchs-Sondheimer model also allows to study the thickness dependency for  $t > 1$  and yields an indirect proportion  $\frac{\rho_T^b}{\rho_T^{tf}} \cong 1 - \frac{3}{8t}$  in that case.

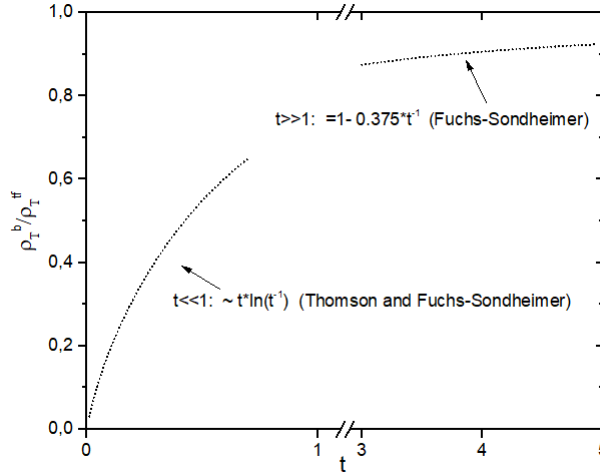


Figure 12: Comparison of theoretical bulk electrical resistivity  $\rho_T^b$  to the one of thin films  $\rho_T^{tf}$  for surface scattering in dependency of the ratio  $t$  of the film thickness to the mean free path in bulk; Thomson- and FS-model agree for  $t \ll 1$  with  $\frac{\rho_T^b}{\rho_T^{tf}} \propto t \cdot \ln \left( \frac{1}{t} \right)$ , for  $t \gg 1$  the FS-model yields  $\frac{\rho_T^b}{\rho_T^{tf}} = 1 - \frac{0.375}{t}$  with  $\rho_T^b = \rho_T^{tf}$  for  $t \rightarrow \infty$ .

In analogy to the FS model Mayadas and Shatzke [64] found a qualitatively similar expression for the grain boundary scattering (MS model). For a detailed treatment of the MS model see [65]. The conductivity in thin films is therefore proportional to that of the bulk, with multiplicative functions accounting for the different types of scattering which in the “bulk-limit” trend towards one.

### 2.6.1 Four-Point Probe Method

A four-point probe consists of four metal pins contacting the surface of the thin film. The contact force is controlled by a Newton meter to prevent the probe and the sample from damage. A schematic is shown in fig. 13.

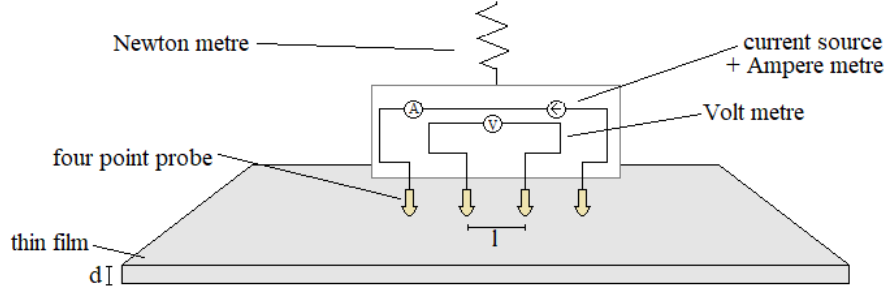


Figure 13: *Schematic of the principle of a four point probe setup. The Newton meter controls the contact pressure; the outer probes conduct a current and the inner ones (separated by the length  $l$ ) measure the voltage of the thin film of width  $w$  and thickness  $d$*

The outer two probes conduct a current  $I_F$  while the inner probes measure the voltage  $U_F$ . The resistivity for films, where the thickness is much smaller than the distance between the pins, is determined by [63, 66]:

$$\rho = \frac{U_F}{I_F} \cdot \frac{\pi}{\ln(2)} \cdot d := R_S \cdot d \quad (10)$$

Here,  $d$  denotes the thickness of the film. To determine a resistance of the film  $R$ , the sheet resistivity  $R_S = \frac{\rho}{d}$  is introduced and defined by the unit  $\Omega/\square$  (ohms per square).

### 2.6.2 Measurement Setup

The setup for heated four-point probe measurements is shown in fig. 14.

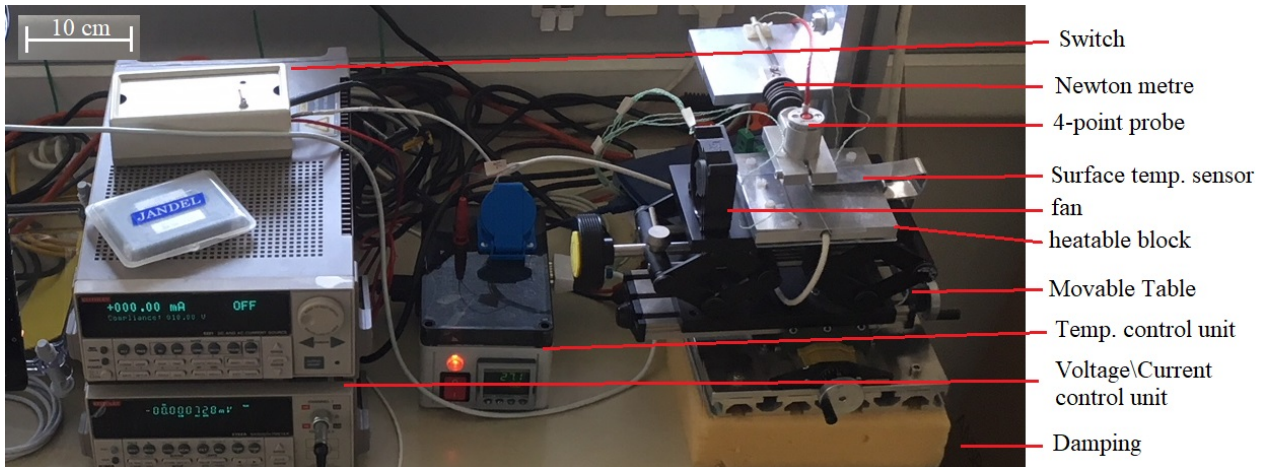


Figure 14: *Four point probe setup*

The sample is mounted onto an aluminum block which is heated by a 150 W heating cartridge. The heating cartridge is connected to a *Eurotherm 3216* digital temperature-controller. The temperature is measured with a thermocouple (type K) mounted under an aluminum clamp to contact with the substrate surface and is also read out digitally via an *Omega TC-08* thermocouple data acquisition module. For substrates with sensitive layers, the surface of a dummy-sample can be measured near the sample using the clamp. The heatable aluminum block is mounted on a movable XYZ-stage which is mounted on a foam mat to avoid vibrations. The four-point probe *Jandl Cylindrical* is mounted on a *Burster 8511-5050* Newton meter. The four-point probe is further connected to a nanovolt-meter *Keithley 2182A* and a constant current supply *Keithley 6221* for high precision measurements. The supplies are controlled digitally to calculate the resistivity following eq. 10. After the sample is positioned in the plane, the stage is lifted till the probe slightly touches the tungsten pins of the four-point probe which is monitored by the Newton meter and should not exceed 5 N to protect the probe. Furthermore, the probe is detached electrically from the supplies before contacting the sample surface to avoid damages to the units by floating potentials. The short-circuiting or off-loading must be done manually using a switch before and after the measurements. Temperatures at the tungsten heads below 120 °C should not affect its functionality and thus the samples were not heated above this limit. The cooling cycles can be accelerated by a 12 V manually controlled fan, installed onto the movable stage.

### 2.6.3 Analysis of the Semiconductor to Metal Transition

A SMT in thin films is mainly characterized by the decrease/increase of the sheet resistivity and a hysteresis behaviour. The hysteresis is due to the fact, that the transition temperature from the semiconducting to the metallic phase differs from the transition temperature from the metallic to the semiconducting phase. A schematic drawing is given in fig. 15 where the heating cycle is shown in red and the cooling in blue.

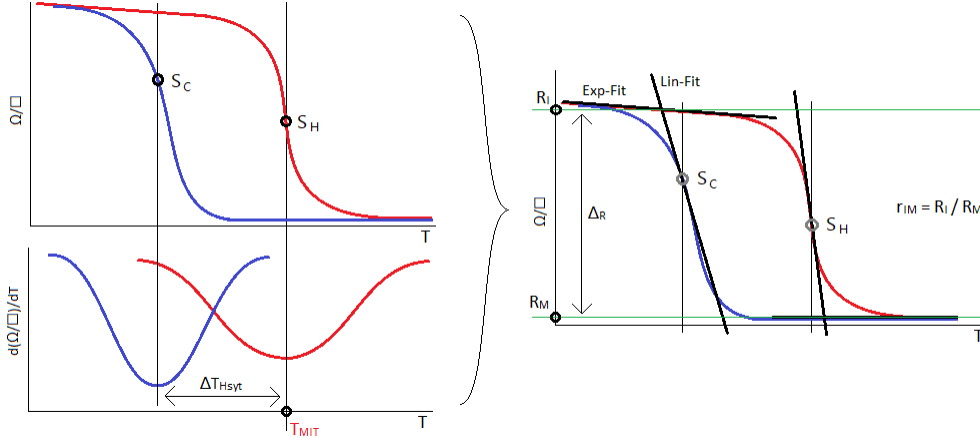


Figure 15: Schematic illustration of how transition temperature, hysteresis width and resistivity change are calculated; The minima ( $S_C, T_{MIT\downarrow}$ ) and ( $S_H, T_{MIT\uparrow}$ ) of the gaussian fit (saddle points of hysteresis) of the derivatives  $\frac{\Delta(\Omega/\square)}{\Delta T}$  of the SMT hysteresis in the heating and cooling cycle yield the transition temperature  $T_{MIT\uparrow} = T_{MIT}$  and the hysteresis width  $T_{MIT\uparrow} - T_{MIT\downarrow}$ ; performing a linear fit around the saddle point of the heating cycle  $L_\uparrow$  and the cooling cycle  $L_\downarrow$  and an exponential fit before  $E_I$  and after  $E_M$  the hysteresis yields four curves; the intersection of  $E_I$  and  $L_\downarrow$  gives  $R_I$  the semiconducting resistivity and  $E_M$  and  $L_\uparrow$  the metallic resistivity  $R_M$  which determines the resistivity change  $r_{IM} = \frac{R_I}{R_M}$

The hysteresis width is estimated by forming the derivative of the four-point measurement data  $\frac{\Delta(\Omega/\square)}{\Delta T}$  and performing a standard Gaussian fit for the heating and cooling cycle. The interval between the maxima of the fitted functions, corresponding to the saddle points of the resistivity curves, is used as a measure for the width of the hysteresis  $\Delta T_H$ . Additionally the determined saddle-points are used to quantify the temperature at which the SMT and the opposite transition occur. The decrease of the sheet-resistivity is obtained by a two-steps fitting process. At first, the regions before and after the SMT are fitted with an exponential function. Then a small region around the saddle points, determined by the fitting procedure used for the hystere-

sis width is fitted by a linear function and extrapolated. The interception values  $R_I$  (sheet resistivity of semiconducting phase) and  $R_M$  (sheet resistivity of metallic phase) of the exponential and the linear functions are then used to determine the drop of the sheet-resistance  $\Delta_R = R_I - R_M$  and the ratio  $r_{IM} = \frac{R_I}{R_M}$  of the SMT.

## 2.7 Principle of X-Ray Diffraction (grazing incidence) and Crystal Structures

The principle of x-ray diffraction (XRD) is based on elastic (Thomson) scattering of photons and electrons. The electrons, in a classical picture, in this case behave like a Hertzian-dipole in an electromagnetic field. A dipole oscillation of an electron bound to an atom is in the order of the atomic size  $\lambda \propto \text{\AA}$  and corresponds to an exciting photon energy  $h\nu = \frac{hc}{\lambda} \propto keV$ , which in turn corresponds to the x-ray spectrum. The reader is referred to the appendix for a detailed derivation of the Laue condition. When a monochromatic x-ray hits a crystal lattice under an angle  $\theta$  and gets scattered at different lattice points they interfere with each other. Constructive interference in the Fraunhofer limit only occurs for angles fulfilling the Laue or Bragg condition [67, 68]:

$$\sin(\theta) \cdot d_{hkl} = \frac{\lambda}{2} \quad (11)$$

Here, the interplanar spacing  $d_{hkl} = \left( \frac{h^2}{a_1^2} + \frac{k^2}{a_2^2} + \frac{l^2}{a_3^2} \right)^{-\frac{1}{2}}$  describes the distance between two parallel lattice planes,  $\lambda$  denotes the wavelength of the impinging monochromatic x-rays and  $a_i$  the lattice constants. The indices  $hkl$  (Miller indices) describe the order of an observed peak in the diffraction pattern. Before analyzing an XRD interference pattern, it is advantageous to have information on the crystal lattice of the sample. The crystal lattice is described by its unit cell which in turn is specified by the three lattice constants ( $a_1 = a$ ,  $a_2 = b$ ,  $a_3 = c$ ) and the three angles between them ( $a_2 \angle a_3 = \alpha$ ,  $a_1 \angle a_3 = \beta$ ,  $a_1 \angle a_2 = \gamma$ ). On the basis of symmetry relations between, or constraints on those quantities, different crystal systems can be identified. Table 2<sup>6</sup> shows a list of crystal systems and the corresponding dependencies of the interplanar spacing  $d_{hkl}$  on  $hkl$  and  $a_i$ .

---

<sup>6</sup> $V = abc\sqrt{1 - \cos(\alpha)^2 - \cos(\beta)^2 - \cos(\gamma)^2 + 2\cos(\alpha)\cos(\beta)\cos(\gamma)}$ ,  $s_{11} = b^2c^2\sin(\alpha)^2$ ,  $s_{22} = a^2c^2\sin(\beta)^2$ ,  $s_{33} = a^2b^2\sin(\gamma)^2$ ,  $s_{12} = abc^2(\cos(\alpha)\cos(\beta) - \cos(\gamma))$ ,  $s_{23} = a^2bc(\cos(\beta)\cos(\gamma) - \cos(\alpha))$ ,  $s_{13} = ab^2c(\cos(\alpha)\cos(\gamma) - \cos(\beta))$

Crystal System	Constraints	$d_{hkl}^{-2}$
Cubic	$a_1 = a_2 = a_3 = a$ $a_1 \angle a_2 = a_2 \angle a_3 = a_1 \angle a_3 = 90^\circ$	$\frac{h^2+k^2+l^2}{a^2}$
Orthorhombic	$a_1 \angle a_2 = a_2 \angle a_3 = a_1 \angle a_3 = 90^\circ$	$\frac{h^2}{a^2} + \frac{k^2}{b^2} + \frac{l^2}{c^2}$
Tetragonal	$a_1 = a_2 = a, a_3 = c$ $a_1 \angle a_2 = a_2 \angle a_3 = a_1 \angle a_3 = 90^\circ$	$\frac{h^2+k^2}{a^2} + \frac{l^2}{c^2}$
Hexagonal	$a_1 = a_2 = a, a_3 = c$ $a_1 \angle a_2 = a_2 \angle a_3 = 90^\circ, a_1 \angle a_3 = 120^\circ$	$\frac{4}{3} \frac{h^2+hk+k^2}{a^2} + \frac{l^2}{c^2}$
Monoclinic	$a_1 \angle a_2 = a_2 \angle a_3 = 90^\circ$ $a_1 \angle a_3 = \beta$	$\frac{h^2}{a^2 \sin^2(\beta)} + \frac{k^2}{b^2} + \frac{l^2}{c^2 \sin^2(\beta)} - \frac{2hl \cos(\beta)}{a \sin^2(\beta)}$
Trigonal/Rhombohedral	$a_1 = a_2 = a_3 = a$ $a_1 \angle a_2 = a_2 \angle a_3 = a_1 \angle a_3 = \alpha$	$\frac{(h^2+k^2+l^2) \sin^2(\alpha) + 2(hk+hl+kl)(\cos^2(\alpha) - \cos(\alpha))}{a^2(1-3\cos^2(\alpha)+2\cos^3(\alpha))}$
Triclin	No constraints	$\frac{s_{11}h^2+s_{22}k^2+s_{33}l^2+2s_{12}hk+2s_{13}hl+2s_{23}kl}{V}$

Table 2: Five crystal systems and the respective constraints on their lattice constants  $a_i$  and angles in between them  $a_i \angle a_j$  and the corresponding interplanar spacing  $d_{hkl}$  defining the Laue condition for x-ray analysis [67]

The investigation of thin films by XRD is challenging due to the small investigation volume compared to the substrate. The reflections from the lattice planes of the thin films will thus be strongly overlaid by the signal from the substrate. To minimize this signal the so called grazing incident x-ray diffraction (GIXRD) can be used. In this case, the incident x-ray beam hits the surface under a flat angle  $\alpha$ . Therefore the path length of the x-rays in the thin film increases and so do the contributions to the signal. This angle is kept constant during the measurements and only the detector is moved along a circle of radius  $R$  between sample and detector. Fig. 16 shows the principle of GIXRD. When the crystal system of the sample and the lattice constants of the sample are known, a certain order of diffraction under an angle  $\theta$  can be assigned to an interplanar spacing  $d_{hkl}$  or lattice plane. following eq. 11. When a sample is unknown the interference pattern can be matched with known samples to identify the crystal. The Scherrer-formula is useful to interpret the width of the XRD peaks. The formula assigns an approximate crystallite size to the FWHM of a peak. It is assumed that crystallites are composed of unit cells stacked together to certain geometrical forms like a cube or sphere, without imperfections and mono-disperse. The Scherrer formula then reads [69]:

$$D_{cryst} = K_S \cdot \frac{\lambda}{\beta_\theta \cdot \cos(\theta)} \quad (12)$$

Here,  $K_S$  denotes the Scherrer constant, which for a cubic packing of the unit cells reads  $K_S = 1$  and for a spherical packing  $K_S = \frac{4}{3} \left(\frac{\pi}{6}\right)^{\frac{1}{3}} \cong 1.07$ . The value of  $\beta_\theta$  is the FWHM of the peak with its center at  $2\theta$  and an excitation wavelength  $\lambda$ .

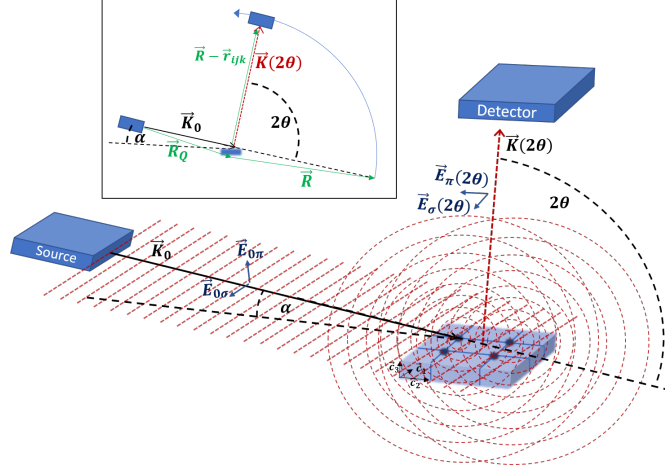


Figure 16: Schematic drawing of GIXRD in the inset and the generation of interference pattern at the detector. The monochromatic x-rays hit the surface under a flat angle  $\alpha$  in a distance  $R_Q$  and leads to dipole radiation from different points  $r_{ijk}$  of the crystal lattice which interfere. The source is kept at the same flat angle while the detector is moved at fixed distance  $R$  over an angle of  $2\theta$ . As XRD detects elastically scattered x-rays the values of the incident and scattered wavevector are equal  $|\vec{K}_0| = |\vec{K}(2\theta)|$

### 2.7.1 Measurement Setup

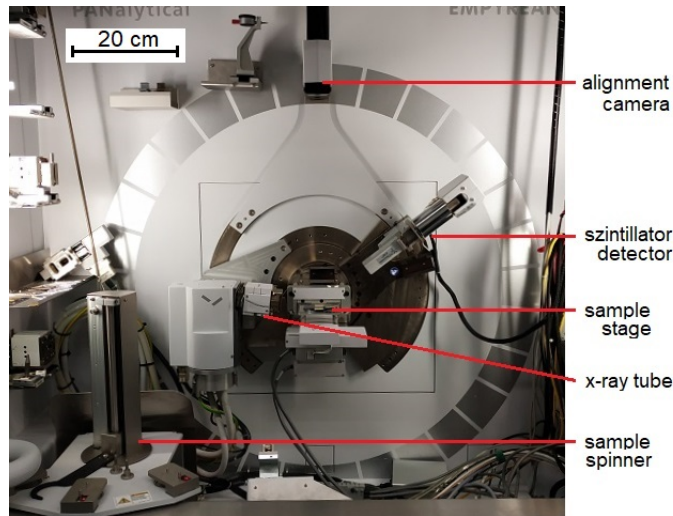


Figure 17: XRD setup used for the (non-heated) GIXRD measurements

The GIXRD setup is shown in fig. 17. The detector is a *PANalytical Empyrean  $\theta - \theta$*  diffractometer. This device allows a broad range of operational modes and setups. During the analysis of the thin films produced during this work a sample changer (sample spinner) was used for automated measurements over night. The GIXRD angle  $\alpha$  was set to  $5.5^\circ$  at a radius R of the setup of 240 mm between sample and detector. As x-ray source a *Cu  $K\alpha_1$  Empyrean Cu LFF HR DK418967* and as detector a scintillation point detector were used. The acceleration voltage at the x-ray tube was set to 450 kV at a current of 0.4 A.

For heated measurements a *PANalytical XPert Pro MPD  $\theta - \theta$*  diffractometer was used. The same settings were used as for the *Empyrean* except the sample was put into an *Anton Paar XRK 900* reaction chamber at 1 bar of pure argon during the heating cycles. The samples could not be mounted on a sample changer and had to be exchanged manually.

### 2.7.2 Analysis of Crystalline films on amorphous substrates in XRD

As the thin oxide films are deposited onto glass substrates of 1 mm thickness which are amorphous, it is important to quantify the contributions of such structures to the XRD signal. In amorphous structures the atomic orientation and lattice constants are not necessarily disordered or randomly distributed but on a longer distance these parameters vary uncorrelated. Therefore, a single lattice plane is not periodic over a long range which is called a short-range order. Interpreting the Scherrer formula in this regard, the crystallite size is very small and therefore the peaks are very broad. These broadened peaks underlay the sharp peaks of the crystalline thin films. In the analysis, the diffractogram of the amorphous glass substrates was determined by asymmetric least square fitting (AsLS) [70] which could automatically be done in the program *HighScore Plus* used to analyze the GIXRD diffractograms. The program additionally identifies the peak positions in the diffractogram and proposes a list of patterns (crystal structures) from elements, that are or could be present in the pattern. This elemental composition must be given to the program by the user. Also the final selection of a set of patterns must be done manually. See chapter five for a visualization.

## 2.8 Surface Analysis by Secondary Electron Microscopy

The principal of secondary electron emission is based on the inelastic scattering of electrons in a medium. The secondary electron microscopy is a sub-field of scanning

electron microscopy (SEM). Electrons interact strongly with matter and have therefore a short penetration depth of 2  $\mu\text{m}$  or less in solids [71]. The main interactions are:

- elastic Rutherford scattering
  - deflections along the path
  - reflections (back-scattered electrons)
- inelastic scattering leading to energy loss:
  - excitation of a loosely bound valence electron or an electron from the conduction band (secondary electron generation), which themselves undergo scattering
  - deflection of an electron in the Coulomb field of a nucleus leading to the emission of electromagnetic waves by the electron in a continuous manner. For high energy electrons this effect leads to the emission of light in the range of several keV which is known as Bremsstrahlung and contributes to the x-ray spectrum of the sample

Due to the excitation of the electrons bound to atoms subsequent quantum mechanical events occur:

- generation of Auger-electrons
- emission of characteristic x-rays by inner shell relaxation
- emission of photons in the from the infrared to the ultraviolet region due to outer shell relaxation

The illustration in fig. 18 shows the so called interaction volume of the electrons, which is determined by the maximum path length an electron can travel inside a medium due to inelastic scattering and thus energy loss.

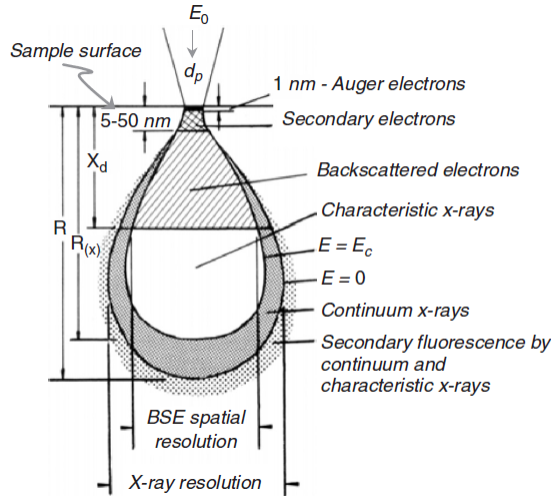


Figure 18: *Interaction volume of an electron beam with initial energy  $E_0$  hitting a sample's surface; along the electron's mean penetration depth  $R \cong 10 \mu\text{m}$  it encounters various scattering mechanisms and following secondary emissions; the best surface resolution is achieved by Auger (surface composition analysis) and secondary (surface topology) electrons; besides simulations, the Bethe formula gives an estimate for the traveling distance and losses of a passing electron in a solid [71]*

A more detailed treatment of theory is given in the appendix. The high resolution of secondary electron microscopy is due to the De Broglie wavelength of electrons, which is given by<sup>7</sup>:

$$\lambda_e = \frac{h}{|\vec{p}_e|} \cong \frac{1.2}{\sqrt{V}} \quad [nm] \quad (13)$$

The wavelength given in eq. 13 using the accelerating potential  $V$  decreases when entering the sample due to the energy and therefore impulse loss. For  $V=30 \text{ kV}$  the corresponding resolution would be  $\lambda_e = 0.1 \text{ \AA}$ . The limiting factor to this resolution are [71]:

- aberrations of the electron optics: quantified by the aperture diameter  $d$  and the aperture-sample distance  $l$  via  $\alpha = \arctan\left(\frac{d}{2l}\right)$ 
  - spherical aberrations  $\propto \alpha^3$
  - chromatic aberrations  $\propto \alpha$
  - aperture diffraction  $\propto \alpha^{-1}$

---

<sup>7</sup>  $\frac{h}{|\vec{p}_e|} = \frac{h}{m_e |\vec{v}|} \sqrt{1 - \frac{v^2}{c^2}} \stackrel{v \ll c}{\cong} \frac{h}{m_e |\vec{v}|} \stackrel{\frac{p^2}{2m_e} \cong E}{=} \frac{h}{\sqrt{2m_e E}} = \frac{h}{\sqrt{2m_e eV}} \cong \frac{1.2}{\sqrt{V}} \cdot 10^{-9} [m]$

- astigmatism: different focal points of horizontal and vertical planes
- the finite size of the interaction volume at the point of impact leads to a decrease of the lateral resolution

Due to the constant electron bombardment, dielectric samples become charged negatively. To prevent this, a thin metal film (e.g. AuPd alloy) of some nanometers is sputtered onto the sample and then grounded.

### 2.8.1 Measurement Setup

The SEM investigations were performed on a *QUANTA FEG 250* shown in fig. 19.

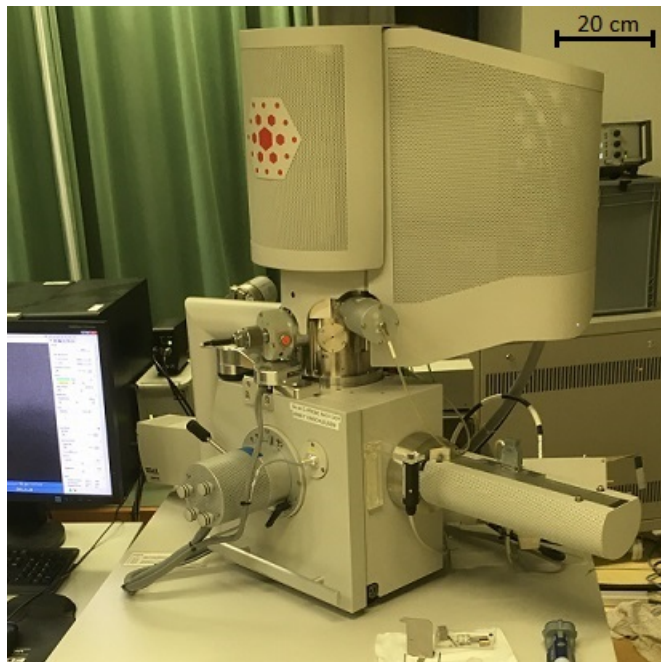


Figure 19: *SEM setup used for secondary electron images*

The electrons are generated by a Schottky emitter with accelerating voltages between 200 V and 30 kV at a chamber pressure of  $6 \cdot 10^{-4}$  Pa. The insulating oxidic samples were coated with a 4 nm thick in layer of AuPd (60:40) in a *Quorum Q150T-S* sputter system and mounted onto a stainless steel specimen holder with a conductive varnish. The samples analyzed in cross section were molded with synthetic resin and cut with an ultramicrotome *RMC Boeckeler PTPC PowerTome*.

## 2.9 Optical Analysis by Fourier-Transform Infrared Spectroscopy (FTIR)

Fourier transform infrared spectroscopy (FTIR) is used to measure optical spectra in the infrared region. The principle of FTIR is to measure an interference pattern of polychromatic light that passes through a Michelson interferometer before screening the sample [72]. The Michelson interferometer consists of a light source that emits mono- or polychromatic light of the form  $E_0(\tilde{\nu}_i) = A_i(\tilde{\nu}_i) e^{i2\pi\tilde{\nu}x}$  where  $A_i(\tilde{\nu}_i)$  denotes the amplitude of a single mode of wave number  $\tilde{\nu}_i = \lambda_i^{-1}$  traveling along x. A beam-splitter divides the light into two beams of half amplitude each. One of the beams travels the distance  $d$  and the other one the distance  $d + \Delta x$  to a movable mirror before both return to the beam splitter where they recombine to  $E'_0(\nu_i) = \frac{1}{2}A_i(\nu_i) e^{i2\pi\tilde{\nu}d} (1 + e^{i2\pi\tilde{\nu}\Delta x})$ . The total intensity is formed by the square of the electric field which is given by<sup>8</sup>:

$$I'_0(\nu_i) = \frac{1}{2}A_i^2(\nu_i) (1 + \cos(2\pi\tilde{\nu}\Delta x)) = \frac{1}{2}A_i^2(\nu_i) + \mathcal{I}(\Delta x) \quad (14)$$

$\mathcal{I}(\Delta x)$  denotes the interferogram containing the information on the phase shift. When the electromagnetic wave travels through a sample (or gets reflected by it) into the detector, the amplitude of the electric field is diminished due to absorption in the sample (or due to transmissive losses in the case of reflection)  $A_i(\nu_i) \rightarrow A_i^s(\nu_i)$  and thus the interferogram changes its shape. The detector collects the total intensity over all wave numbers for each step  $\Delta x_m$ . It therefore measures a set of  $\mathcal{I}(\Delta x_m)$  which by the cosine Fourier transform (in the limit  $\Delta x_m \rightarrow 0$ ) yields the wave number dependent intensity modulation:

$$\hat{\mathcal{I}}(\tilde{\nu}) = \int_{-D > -\infty}^{D < \infty} \mathcal{I}(\Delta x) \cos(2\pi\tilde{\nu}\Delta x) d(\Delta x) = 2 \int_0^D \mathcal{I}(\Delta x) \cos(2\pi\tilde{\nu}\Delta x) d(\Delta x) \quad (15)$$

The upper limit of the integral  $D$  denotes the finite distance which can be covered by the moving mirror and thus the main factor limiting the resolution of the method.  $\hat{\mathcal{I}}(\tilde{\nu})$  denotes the Fourier transform of  $\mathcal{I}(\Delta x)$ . The non-dispersive nature of FTIR has three main advantages over dispersive spectrometers [73]:

- precision and accuracy: the movement of the mirror is controlled by a laser

---

<sup>8</sup> $|E'_0(\nu_i)|^2 = \frac{A_i^2(\nu_i)}{4} |(1 + e^{i2\pi\tilde{\nu}\Delta x})|^2 = \frac{A_i^2(\nu_i)}{4} (2 + e^{i2\pi\tilde{\nu}\Delta x} + e^{-i2\pi\tilde{\nu}\Delta x}) = \frac{A_i^2(\nu_i)}{2} (1 + \cos(2\pi\tilde{\nu}\Delta x))$

(passing the same Michelson interferometer) which produces a monochromatic and highly coherent wave. This allows to measure the mirror position  $x$  (accuracy) and changes  $\Delta x$  (precision) with a high local resolution.

- High signal-to-noise ratio and scanning speed: to gain a high spectral resolution in dispersive spectrometers the light is separated by a grating and the frequency range  $\nu \pm \delta\nu$  is collected by a fine slit, decreasing the amount of light and thus the signal-to-noise ratio significantly while slowing down the scanning process. In the case of FTIR such fine slits are not necessary as the whole frequency (or rather wave number) spectrum and total intensity is measured at a time. After one scan of  $n$  frequency steps the dispersive spectrometer measured one value of every interval while the FTIR spectrometer measured  $n$  values of every wave number.

For a treatment of the resolution of FTIR it is referred to [74]. As an upper limit however, the maximum resolution  $\Delta\tilde{\nu}$  in the wave number spectrum is in any case at least  $\Delta\tilde{\nu} = D^{-1}$ .

### 2.9.1 Tauc Plots

To estimate the bandgaps of metal oxide thin films, Tauc plots have shown to be a simple and powerful tool. Tauc plots are based on the Tauc-formula for the calculation of direct and indirect optical bandgaps [75]:

$$\alpha \cdot h\nu = A \cdot (h\nu - E_g^o)^n \quad \begin{cases} n = \frac{1}{2} : & \text{direct allowed bandgap} \\ n = 2 : & \text{indirect allowed bandgap} \end{cases} \quad (16)$$

The value  $\alpha$  is the mass absorption coefficient,  $h\nu$  the excitation energy,  $E_g^o$  the optical bandgap and  $A$  a constant. An optical bandgap corresponds to the energy needed to absorb a photon of energy  $h\nu$ . The electronic bandgap is the energy needed to excite an electron into the conduction band, where it can separate from the hole, this is not necessarily the case for an electron excited by photon absorption. In this case the electron and hole may still be bound in a sense, that the electron movement is not independent from that of the hole, which is called an exciton. An exciton has a certain exciton binding energy, quantifying the interaction strength between electron and hole. The terms “direct allowed bandgap” and “indirect allowed bandgap” refer to the way an electron moves into the conduction band. This becomes clear from the energy dispersion  $E(\vec{k})$  of the electronic band structure where  $E$  describes the energy and  $\vec{k}$  the wave

vector of the lattice. Direct band gaps allow the electron to move into the conduction band without a change of  $\vec{k}$  while indirect ones are accompanied by a change of  $\vec{k}$ . For photon absorption, the possibility to be absorbed in a transition is much higher for direct bandgaps, as the band electron only has to change its energy and not the impulse. A transition is said to be allowed, if the corresponding quantum mechanically calculated transition probability is greater than zero. Under the assumption of either direct or indirect allowed transitions in a semiconductor, one can plot the quantity  $(\alpha \cdot h\nu)^{\frac{1}{n}}$  over  $h\nu$ . This quantity is then proportional to  $h\nu - E_g^o$  in certain regions. In other words, linear regions of  $(\alpha \cdot h\nu)^{\frac{1}{n}}$  can be fitted by a function  $C_1 \cdot (h\nu - C_2)$ , where the fitting constant  $C_2 = E_g^o$  yields the corresponding optical bandgap.

### 2.9.2 Measurement Setup

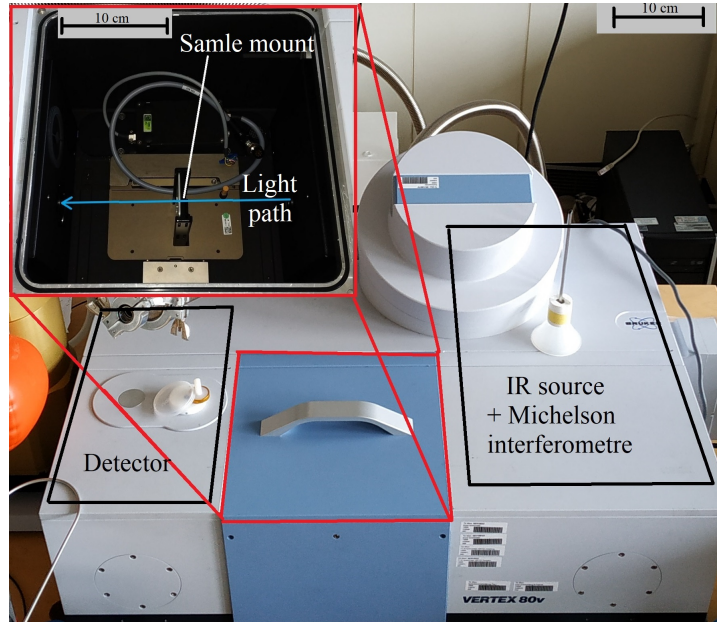


Figure 20: *FTIR setup: the inset shows the vacuum chamber in transmission mode, the blue arrow indicates the light path; the IR source and Michelson interferometer are positioned on the right side and the detector on the left.*

The FTIR measurements were performed on a *Bruker Vertex 80v* shown in fig. 20. The samples were mounted on a specimen holder and placed inside the vacuum chamber for transmission measurements. The vacuum was set below 1.25 hPa to eliminate scattering by air molecules.

### 3 Experimental Setup of the Sputter System

In the following chapter, the functionality of the sputter system together with the preparation of the samples are explained. During this work, parts of the sputter system were digitized using analog to digital converters and a micro-controller. The digital and digitized components of the system were implemented into a central PC using LabView and an “easy-to-use” graphical interface was programmed for the central control of the (reactive) DC magnetron sputter system. Hence, the digitization and the LabView program are explained and illustrated in detail as well.

#### 3.1 Sputtering System and Sample Preparation

A technical drawing of the sputter system in which the vanadium oxides were produced including the heatable substrate holder, is shown in fig. 21.

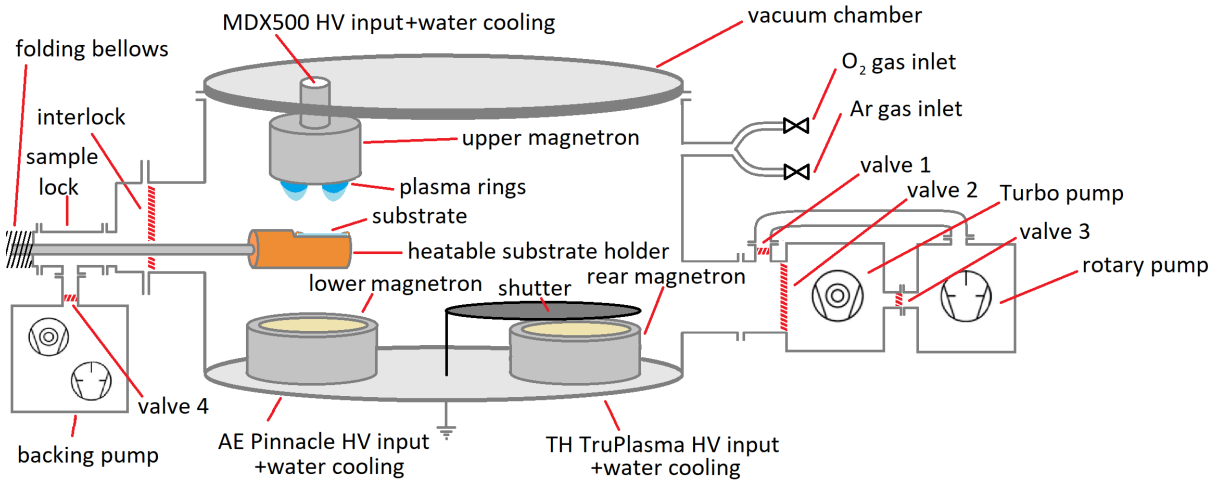


Figure 21: *Schematic drawing of the sputter system with a loaded substrate holder, explanation see text*

The vacuum chamber contains three planar magnetrons and can therefore hold three targets. The planar magnetrons and targets are cooled by a water cooling system to about 18 °C during the sputter process. The upper magnetron can fit a target of 2” diameter. This magnetron was used for the deposition of the vanadium layers using a 2” vanadium target of 99.99% purity from *Kurt J. Lesker Company*. As power supply an *Advanced Energy MDX500W* was used. The lower and the rear magnetron both fit a 4” target. The rear magnetron contains a 4” titanium target used for the chemisorption

of residual gases in the chamber to obtain lower background pressure and uses a *TRUMPF Hüttlinger TruPlasma 3005* power supply. The lower magnetron contains a 4" tungsten target which was not used during the experiments and is supplied by an *Advanced Energy Pinnacle 10 kW*. It is installed for a possible doping of the vanadium oxide layers following recent results concerning this matter [76]. A rotational shutter is positioned at the bottom of the vacuum chamber to cover the targets when not in use and to control the deposition from the lower and rear target onto the substrate. The vacuum chamber is separated from the sample lock by a sliding valve. The valve is connected by two guiding rods to the frame holding a gear unit to slide the substrate holder in and out of the chamber. The horizontal sliding movement in high vacuum conditions is ensured by a folding bellows fixed on the substrate holder and connectable to the sample lock. The sample holder is rotatable by a stepper motor which is also mounted on the guiding rods. The rotational movement in high vacuum conditions is possible due to a magneto-fluid sealing. The substrate holder and the stepper motor are connected to the gear unit via a roller chain. The chain itself is kept under tension by the vacuum and can be fixed by a ratchet mechanism. The substrate holder head made of copper is heatable up to 400 °C by a 300 W heating cartridge and controlled by an *Eurotherm 3216* temperature control PID unit. The sample holder head can also be grounded or set to a bias voltage. The sample lock is vented to change the sample when the interlock is closed. Via a backing pump *Alcatel DRYTEL 25* the sample lock and the folding bellows are evacuated to about  $10^{-2}$  Pa before the valve to the high vacuum chamber can be opened. This is indicated by a green LED on the backing pump. The backing pump is accessible via a manually operated valve (valve 4 in fig. 21). The substrate holder head is centered below the vanadium target at a sample-target distance of 50 mm. The pressure inside the chamber is controlled by a turbomolecular pump *Alcatel 5402 CP* connected through valve 2. A rotary pump *Alcatel 2033* is used as backing pump for the turbomolecular pump (via valve 3) and to evacuate the chamber down to about 10 Pa (via valve 1) after it was vented, before the turbomolecular pump is switched into the system. The pressure is controlled by three pressure sensors. A Pirani pressure gauge *Alcatel PB 101/111* covers the region from about 100 Pa down to 0.1 Pa. A penning pressure gauge *Alcatel CF2P* ranges from 1 Pa down to  $10^{-5}$  Pa. A capacitance manometer *MKS Baratron 390HA* which is controlled by a *High Accuracy Signal Conditioner MKS 270D*, measures from 133 Pa to about  $10^{-3}$  Pa. The Pirani pressure gauge is connected to valve 1, valve 2 and the opening valve for the Baratron. In case of a pressure increase inside the chamber above 10 Pa

the Pirani triggers the closing of these valves to keep the devices from damage (due to a defect of the alert unit the penning gauge is not protected by this mechanism). The gas inlets for argon and oxygen are controlled by mass-flow controllers from *MKS GE50A* which regulate flows from 1 sccm to 100 sccm in the case of argon and from 0.75 sccm to 50 sccm in the case of oxygen. They are each separable from the pressure regulators attached to the gas cylinders by needle valves and digitally accessible via Ethernet ports.

As a substrate, standard microscope slides of 1 mm thickness were used. The slides were cut into pieces of 26 by 10 mm, to fit the substrate holder head. They were cleaned with ethanol and low linting laboratory wipes before fixing them onto the substrate holder head by two copper platelets. A loaded sample is shown in fig. 22.

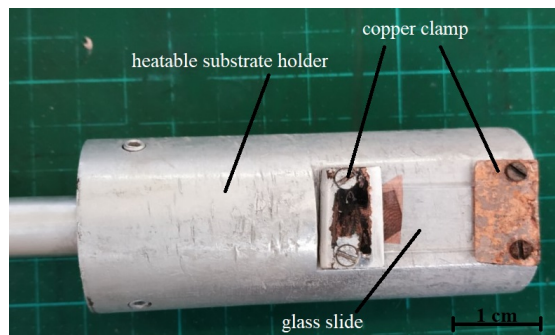


Figure 22: *The glass slide is mounted on a heatable copper substrate holder containing a 300 W heating cartridge; for an even heat distribution the slide is clamped to the holder by two copper plates*

### 3.2 Digitizing an analog Pressure Sensor and Power Supply for Reactive DC Magnetron Sputtering

The aim was to digitally control the pressure from the pressure sensor *MKS Baratron 690A*, gas flow from the oxygen and argon gas flow controllers *MKS GE50A* and to record the voltage, current and power from the power supply *Advanced Energy MDX500*. The pressure sensor is accessible via the readout unit *High Accuracy Signal Conditioner MKS 270D* which is equipped with an analog output. Likewise is the power supply. The flow controllers are accessible via an Ethernet interface. Thus, an analog-to-digital converter (ADC) had to be set up for the pressure sensor readout unit and the *MDX500* while the flow controllers were connected to the computer in parallel via a LAN-switch. An *Arduino Uno* micro-controller turned out to be the best choice for the readout of the

analog data at a reasonable price while providing a broad range of easy to implement sensor systems, converters and communication devices (breakout boards). The type of ADC used to communicate with the pressure sensor readout unit is a 16 bit  $i^2c$ <sup>9</sup> converter *ADS1115* which can digitize analog signals up to 6 V. The maximum sample rate of the *ADS1115* is 860 sps which is equivalent to 1 value every 1.2 ms. (the manual is added in the CD attached to this thesis)

The Baratron pressure sensor can operate at a maximum pressure of 1 Torr (=1.33 · 10<sup>2</sup> Pa) and resolves pressure above 1 · 10<sup>-5</sup> Torr (=7 · 10<sup>-3</sup> Pa). The pressure sensor readout unit has a 0 to 10 V analog output with a relative resolution of 5 · 10<sup>-5</sup>. At 10 V output voltage the pressure would then be 1.33 · 10<sup>2</sup> Pa and at 0 V the pressure would be ≤ 7 · 10<sup>-3</sup> Pa at full scale. The pressure sensor readout unit can be tuned to a certain percentage of the full range. In our case it is set to 10% which corresponds to a maximum pressure of 0.1 Torr (=13.3 Pa). The analog signal from the pressure sensor readout unit must be down-converted due to the input limit to the *ADS1115*. At 1 V input voltage, the ADC has its maximum resolution of 2<sup>15</sup> channels corresponding to an absolute resolution of  $\Delta p = 4.1 \cdot 10^{-4}$  Pa which is required for a fine control of the pressure. Therefore a voltage divider was necessary to scale down the voltage by a factor of 10. The principle of a voltage divider is given by the following formula:

$$V_{out} = V_{in} \cdot \frac{R_{out}}{R_{in}} \quad (17)$$

Here,  $R_{out}$  is the output resistor and  $R_{in}$  the resistor connected to the analog output. To protect the Arduino from current and voltage spikes a zener diode with a breakdown voltage of 5.6 V is installed in parallel to the output resistor.

The *MDX500* power supply generates analog output voltages between 0 V and 10 V corresponding to either 0 W to 500 W output power  $P$ , 0 A to 1 A output current  $I$  or 0 V to 1200 V output voltage  $U$ . Because of the relation  $P = U \cdot I$  one quantity is always expressible by the other two and therefore only two of them were read out by an ADC. Due to connection problems with the analog output of the voltage at the *MDX500* (no signal at the pin) the two values read out are the power and the current. The voltage values are then calculated by  $U = \frac{P}{I}$ . As the resolution of the analog output of the power supply is quite limited with 0.2% off the chosen full scale which corresponds to

---

<sup>9</sup> $i^2c$  is a BUS system in which the external devices like an *ADS1115* communicate with the Arduino via the SCA and SCL port in parallel. The devices are assigned with a certain address (e.g. 4 bit address allows 2<sup>4</sup> devices). The devices can then be accessed one after another through one connection only.

an uncertainty of 2.4 V, 2 mA and 1 W respectively, the built in 10 bit ( $2^{10}$  channels) ADC of the *Arduino Uno* could be used. The built in ADC can process voltages up to 5 V. Thus, the voltage  $V_{in}$  from the power supply had to be down converted as well. A down conversion from 10 V maximum output to 5 V at the *ADS1115* and a resolution of 0.97 mV and 0.48 W seemed sufficient. In fig. 23 the circuits of the two analog devices are shown.

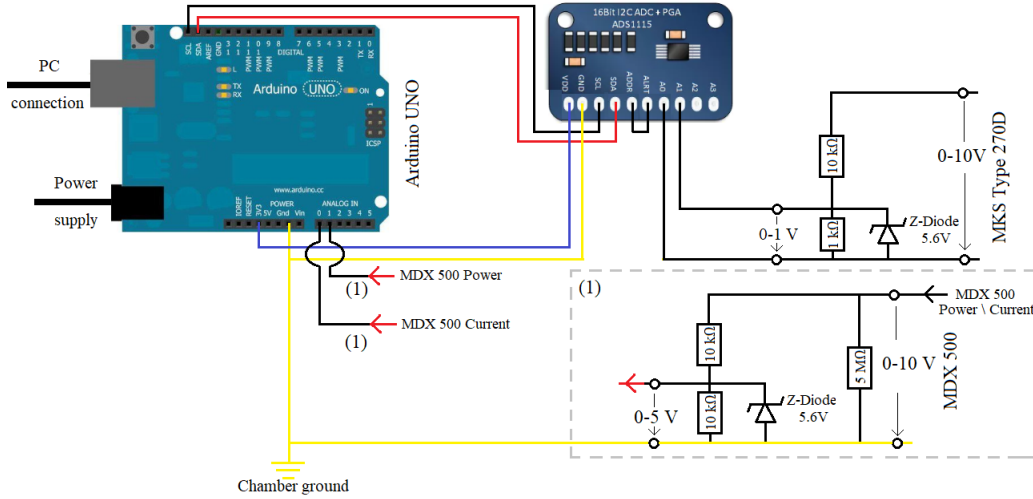


Figure 23: Schematic circuit of the analog to digital converters(ADC) for the MDX500 power supply and the readout unit MKS (type 270D) of the pressure sensor MKS Baratron (type 690A). The pressure sensor is converted differentially by a ADS1115 ADC of 15 bit resolution while the MDX 500 signal is directly converted from the built in ADC of the arduino with 10 bit resolution. The 0-10 V output of the pressure sensor is down-converted to 0-1 V by a voltage divider and protected from voltage spikes by a 5.6 V Zener diode. The two signals from the MDX 500 are also down-converted to 0-5 V against chamber and power supply ground shown in the inset (1)

The digitized voltage values from the pressure sensor and the *MDX500* are converted into pressure, current and power values by the Arduino who runs the program *Differential\_Output\_ADC.h*. The arduino in turn is controlled by the central computer of the working station. However, during the measurements it was found that (only) the power supply *Advanced Energy Pinnacle* generates an impedance when operating, which through the grounding enters the circuit of the arduino and the ADC. The impedance leads to slight fluctuations and an offset of the pressure output from the arduino. This issue should be addressed in further improvements of the setup.

The computer controls all digital and analog devices by the graphical programming interface *LabVIEW* from National Instruments. In the process of this work the analog

devices and the flow controllers were implemented into LabVIEW. The flow controllers were delivered already providing the LabVIEW subVIs necessary to communicate and control them. The program was later further expanded by David Böhm during his PD. The parts programmed during my work are the automated recording of the reactive sputter hysteresis, the pressure control, the *MDX500* readout and the alarm mode. In the following, a short explanation of the programmed units and their functionality is given.

The subVIs written for the communication with the arduino and the flow controllers are part of the main program *Steuerung\_LABII.lvproj*. The aim was to keep the program as time efficient as possible. The subVIs were thus built up from case structures. Further, to better control the data stream from and to the arduino, the communicating parts of the program actively ask the devices for data rather than reading a continuous data stream.

The subVI *Arduino\_readout.vi* controls the data readout from the arduino which in turn reads out the *MDX500*, the pressure sensor readout unit and also two digital temperature sensors (*DALLAS 18B20*). The temperature sensors were installed at the chamber walls and inside the box containing the arduino and the voltage dividers. The subVI is shown in fig. 24.

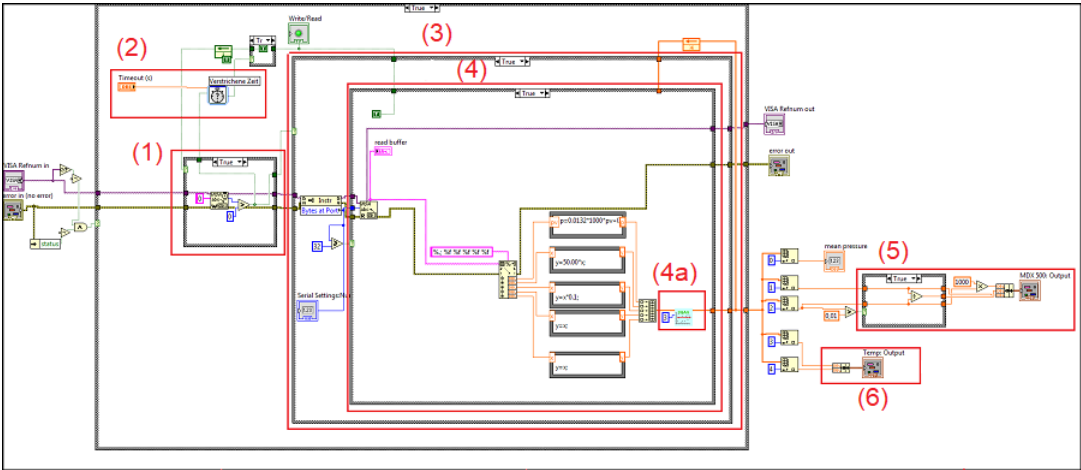


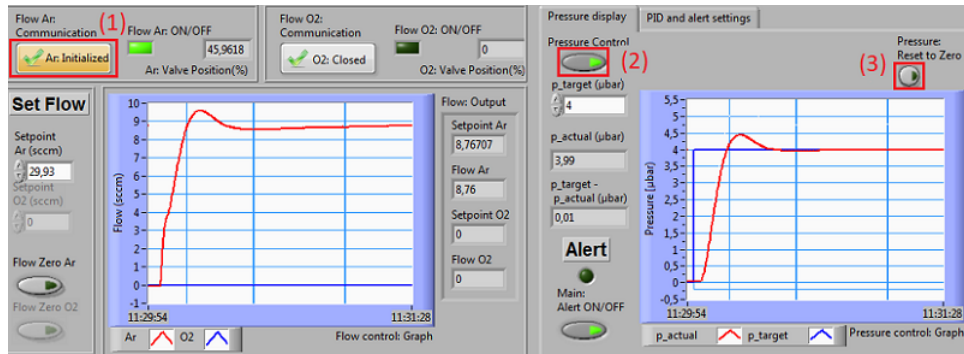
Figure 24: *Block diagram of the LabView subVI “Arduino\_readout.vi”, explanation in the text*

The outermost case structure checks if the path to the arduino is valid and if no error occurred up to this point. If the conditions are satisfied the true-case is entered. At (1) the arduino receives a “0” byte from the program . The arduino only writes to

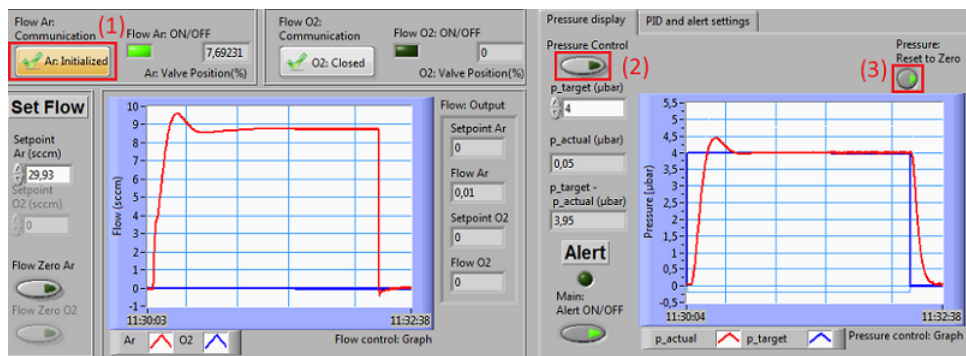
the port if it gets a byte from the program. The true-case of (1) is only entered, if the last read-write-cycle has finished (therefore a “true” is sent from (4) to the selector input of (1)) or the timeout (2) has expired. If the writing of a “0” byte by (1) to the arduino was successful a “true” is sent to the selector-input of (3) the timeout (2) is reset. If not, the writing process to the arduino is going to be repeated in the next loop and the false case of (3) is entered. Then, the function *Bytes at Port* asks for information from the arduino and only enters the "true" case of (4) if the minimum number of bytes (in the current case 32) are present at the port. If not, the false case of (4) is entered, returning a false to the selector-input of (1). In (4) the data stream from the arduino is read out and converted from a string to double precision numbers. The numbers are then further converted into physical values. The pressure readout value  $pv$  (voltage corresponding to a certain pressure) is converted by the empirically derived formula  $p = 0.00132 \cdot pv + 0.003$  into a pressure value in Pa. The readout values from the *MDX500* are converted into current- and power-values by the conversion factors from the *MDX500* manual. The values from the temperature sensors are already sent as real temperature values and are left unchanged. Then the converted values are averaged by the subVI (4a) over a certain number of loops (in the current case 3) to gain a smoother signal. Then, a "true" is sent to the to the selector input of (1) and the values are passed at the one hand to (5) where the voltage value is calculated by  $U = \frac{P}{I}$ . The current value is converted from mA to A and the two temperatures are forward to the temperature output (6).

### ***Pressure\_PID\_Control.vi***

The subVI *Pressure\_PID\_Control.vi* allows to regulate the argon chamber pressure to a certain value. In order to set the argon pressure, a communication to the flow controllers had to be set up. The flow controllers themselves were already delivered from *MKS* with a library of subVIs to control them via an Ethernet connection. For the pressure control subVI only the subVI *MB\_Sp+.vi* from the *MKS* library was needed, which can read/or write a flow value from/to a certain IP address. The front panel of the pressure control subVI is shown in fig. 25. It is designed to regulate the argon pressure. Therefore the *Pressure Control* button (2) is grayed out as long as there is no communication with the argon flow controller. When the button (1) is pressed, the Ethernet connection to the argon flow controller is activated and the pressure control VI can be started by pressing (2). When the “Reset to Zero” button (3) is pressed



(a)



(b)

Figure 25: Front panel of flow and pressure control: (a) PID-controller regulates to the target pressure (here  $4 \cdot 10^{-3}$  mbar) with an accuracy of  $\pm 0.01 \cdot 10^{-3}$  mbar; (b): (3) “Pressure Reset to Zero” is activated and resets the flow automatically to zero when the “Pressure Control” button is released

before or during the pressure control, the argon flow and thus the pressure will be reset to zero when (2) is released. The block diagram is shown in fig. 26.

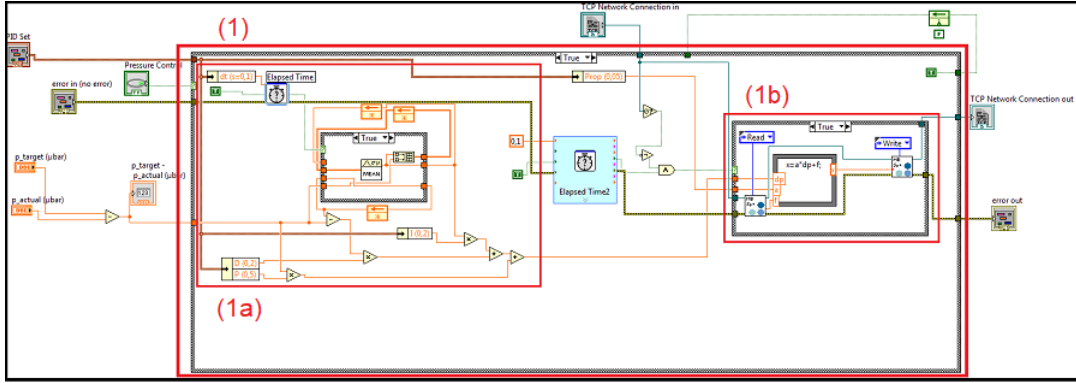


Figure 26: Block diagram of the LabView subVI “Pressure\_PID\_Control.vi” showing the true-case of structure (1), explanation in the text

The main input parameter for this subVI is the difference between the target pressure and the actual argon pressure  $\delta p_{Ar}$ . The "true" case of (1) contains the PID controller (1a) and the set-point unit (1b). The principle of the PID controller is a feedback loop, following the general equation (in first order):

$$\delta f_{Ar} = prop \cdot \left( \hat{P} \cdot \delta p_{Ar} + \hat{I} \cdot \int_{t_1}^{t_2} \delta p_{Ar} dt + \hat{D} \cdot \left. \frac{d(\delta p_{Ar})}{dt} \right|_{\xi \in [t_1, t_2]} \right) := prop \cdot \Delta p_{PID} \quad (18)$$

The argon flow change  $\delta f_{Ar}$  is proportional to the pressure difference  $\hat{P} \cdot \delta p_{Ar}$ , the summed up change of the pressure difference in a certain time interval  $\hat{I} \cdot \int_{t_1}^{t_2} \delta p_{Ar} dt$  and the gradient  $\hat{D} \cdot \left. \frac{d(\delta p_{Ar})}{dt} \right|_{\xi \in [t_1, t_2]}$ . The parameters  $\hat{P}$ ,  $\hat{I}$ ,  $\hat{D}$  had to be tuned empirically. the value  $prop$  is a parameter, introduced for convenience as it regulates  $\delta f_{Ar}$  without having to tune the sensitive PID values. The behavior of such a feedback loop is a damped oscillation which regulates to the point where  $\delta p_{Ar} = \delta f_{Ar} = 0$ . In order to numerically use eq. 18 in a program the integral is approximated by a sum<sup>10</sup> and the gradient by a difference quotient<sup>11</sup>. The constant  $dt$  is subsumed into  $D = \frac{\hat{D}}{n \cdot dt}$  and  $I = \hat{I} \cdot dt$ . The best PID values, time interval  $n \cdot dt$  and proportion factor  $prop$  found by calibration in range between 0.1 Pa and 2 Pa are given in table 3.

---

<sup>10</sup>  $\int_{t_1}^{t_2} \delta p_{Ar} dt \cong dt \sum_{i=1}^n \delta p_{Ar, i}$   
<sup>11</sup>  $\left. \frac{d(\delta p_{Ar})}{dt} \right|_{\xi \in [t_1, t_2]} \cong \frac{\delta p_{Ar}(t+n \cdot dt) - \delta p_{Ar}(t)}{n \cdot dt}$

P	I [ $s^{-1}$ ]	D [s]	prop [ $\mu\text{bar}^{-1} \cdot \text{sccm}$ ]	$n \cdot dt$ [s]
0.5	0.2	0.2	0.05	0.1

Table 3: Empirically derived values for “Pressure\_PID\_Control.vi” on the basis of eq. 18

The value  $\Delta p_{PID}$  is calculated by (1a) in the "true" case of (1) and sent to (1b). To regulate the number of reading and writing cycles from the argon flow controller, the true-case of (1b) is only called when 0.1 seconds have passed and the communication is working properly. The true-case in (1b) first reads the actual flow value from the controller and then calculates  $f_{Ar}(t + n \cdot dt) = f_{Ar} + \delta f_{Ar} = f_{Ar} + prop \cdot \Delta p_{PID}$  which is then set at the argon flow controller. The false case of the *Pressure\_PID\_Control.vi* is shown in fig. 27.

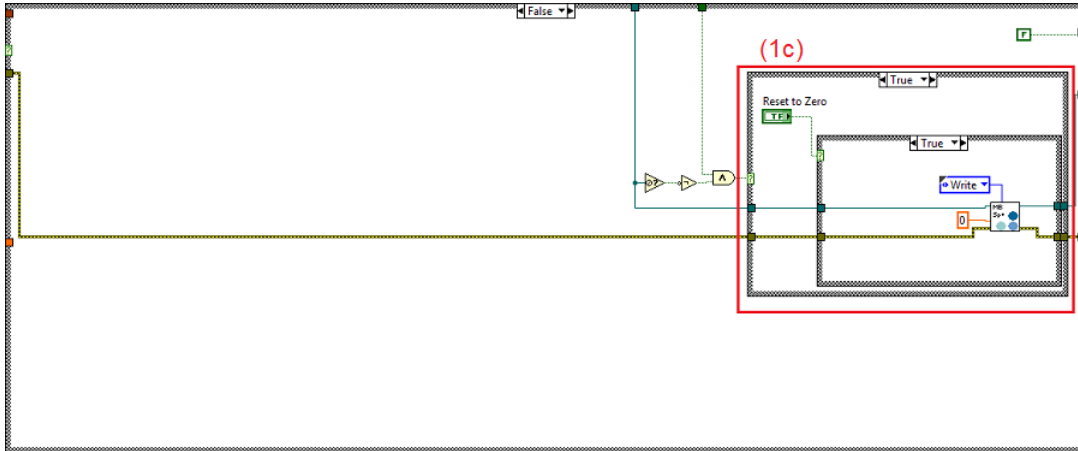


Figure 27: Block diagram of the LabView subVI “Pressure\_PID\_Control.vi” showing the false-case of structure (1), explanation in the text

The case structure (1c) receives a "true" value, when the pressure control button was just released. In the true-case of (1c) the Boolean “Reset to Zero” controls whether or not the flow and therefore the argon pressure should be set to zero when the PID control is ended.

## Alarm

The main program also features an alarm mode. The alarm is not designed as a subVI but integrated into the main program shown in the block diagram in fig. 28.

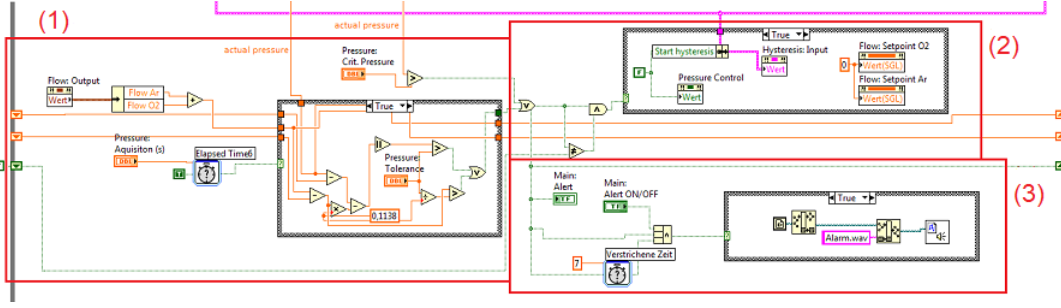


Figure 28: Block diagram of the LabView VI “Steuerung\_LABII.lvproj” showing the alarm mode, explanation in the text

The alarm reacts if either a critical pressure is reached or the total flow change  $\Delta f_{tot} = \Delta f_{Ar} + \Delta f_{O_2}$  (argon and oxygen) and the total pressure change  $\Delta p$  during the acquisition time  $\Delta t_{aq}$  drift apart by a certain value. At (1) the total flow of argon and oxygen  $f_{tot}(t)$  is calculated and passed to the case structure. The acquisition time handles the case structure and defines the reaction time of the alarm. The actual pressure  $p(t)$ , coming from the arduino, is on the one hand compared to the critical pressure  $p_{crit}$ , and other other hand passed to the case structure. The pressure and flow values  $p(t - \Delta t_{aq})$  and  $f_{tot}(t - \Delta t_{aq})$  from the preceding acquisition are passed through the while loop as long as  $\Delta t_{aq}$  has not expired. When  $\Delta t_{aq}$  has expired  $p(t)$ ,  $f_{tot}(t)$ ,  $p(t - \Delta t_{aq})$  and  $f_{tot}(t - \Delta t_{aq})$  are passed to the case structure in (1). From those values the total flow change  $\Delta f_{tot} = f_{tot}(t) - f_{tot}(t - \Delta t_{aq})$  and total pressure change  $\Delta p = p(t) - p(t - \Delta t_{aq})$  are calculated inside the loop. Empirically, the change of pressure in dependence of the flow change was found to be  $\Delta p = 0.1138 \cdot \Delta f_{tot}$ . This equation forms the “drift” condition, which can react to errors before the critical pressure is reached. If the pressure change lies above a tolerance  $\Delta p^{tol}$  expressed as  $|\Delta p_{tot}| \geq |\Delta p_{tot}^{tol}| = \alpha \cdot |\Delta p_{tot}|$  and/or the flow change above  $|\Delta f_{tot}| \geq \frac{\alpha \cdot |\Delta p_{tot}^{tol}|}{0.1138}$  the case (1) passes a "true" to (2). The same counts for the critical pressure condition. In (2) the pressure control and hysteresis mode are stopped and the flows are reset to zero. Case (3) then starts the alarm tone and only stops if either the system returns to a normal state or the alert is turned of by the *Alert ON/OFF* button manually.

### *Pressure\_hysteresis.vi*

The subVI *Pressure\_hysteresis.vi* is designed to automatically carry out a reactive sputter hysteresis and display and save the time course of the system parameters as an external exe-file. A view of the front panel of the subVI is shown in fig. 29.

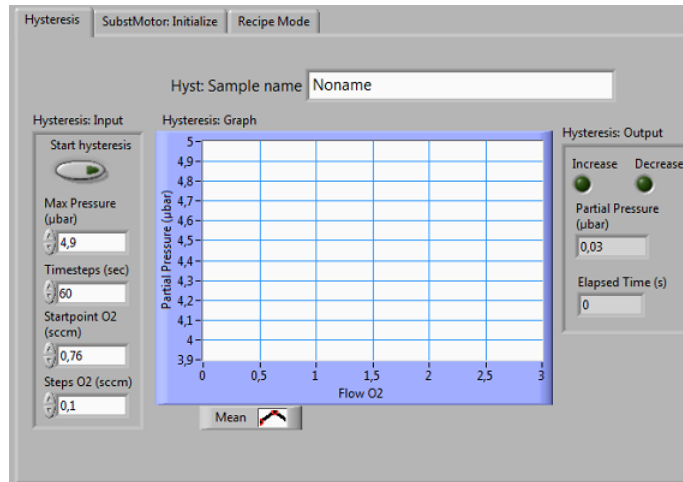


Figure 29: Front panel of the subVI “*Pressure\_hysteresis.vi*” used to automatically perform hysteresis measurements for reactive DC magnetron sputtering

Before pressing the *Start hysteresis* button, four parameters have to be set:

- the maximum pressure (“*Max Pressure (µbar)*”), which determines at which total pressure inside the chamber the flow stops to increase and starts decreasing
- the time-steps (“*Timesteps (sec)*”), which controls the rate of oxygen flow
- the change of oxygen flow per time-step and the starting point (“*Steps O2 (sccm)*”)
- the starting-point (“*Startpoint O2 (sccm)*”)
- a distinct filename can be chosen (“*Hyst: sample name*”)

The oxygen flow controller is by construction unable to pass oxygen flows below 0.75 sccm. The oxygen partial pressure  $\Delta p_O = p - p^{start}$  is calculated from the total pressure during the hysteresis  $p$  minus the (argon) pressure in the chamber at the start of the hysteresis  $p^{start}$ . A drawback of this simple method is that the pressure in the chamber may not only change due to the reactive sputter process itself but also due to heat fluxes, which is not accountable for directly in the program. Fig. 30 shows the block diagram of the VI.

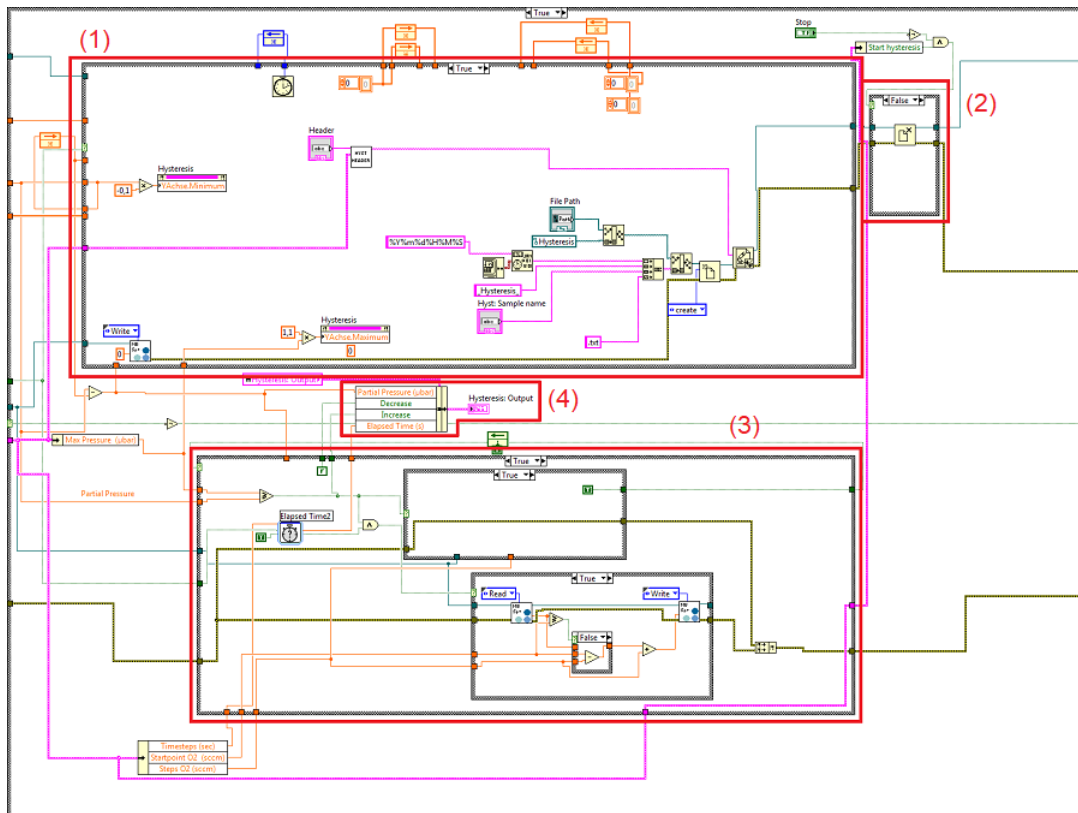


Figure 30: Block diagram of the LabView subVI “Pressure\_PID\_Control.vi”, explanation in the text

The case structure (1) handles the writing of data (voltage and current from all power supplies, gas flows, total and partial pressures and temperatures) to an external file. The true-case is only called once at the beginning of a hysteresis measurement to set the Y-axis according to the chosen maximum pressure of the hysteresis parameters, create a new txt.file at the main path and write a header into the file. The false-case of (1) averages the data periodically five times per time-step and writes them to the external file and the front panel. (2) closes the file when the hysteresis is finished or the main program is ended. In (3) the flow increase and decrease are executed, of which a detailed view is shown in fig. 31.



not reached and a therefore a “false” is sent to the selector input of (3). When 0.75 sccm are reached (3c) enters the false-case, not further decreasing the flow as well as (3d), resetting the oxygen flow to zero, sending a "true" to the selector input of (3) and setting the start hysteresis Boolean to “false”, which leads to the false-case of (2) where the file is closed and the hysteresis terminated.

The event structures controlling the flow controllers are part of the subVI *Modbus MFC Example.vi* from MKS and were only slightly changed to meet the requirements of the program. The well documented subVIs and an extra manual from MKS are provided in the extra CD to this work.

## 4 Target Temperature Calculation, Simulation and Measurement with Reduced Target Cooling

In this chapter, the target temperature during the sputter deposition in dependence of the contact area between target and cooling system is studied by calculations in a simplified one dimensional model and simulations, using the software *Solidworks 2017*. Further, several approaches to measure the target temperature in situ are presented and discussed.

For the production of  $VO_2$  thin films with reduced target cooling described in section 5.1.2, the contact area between target and water cooling system was reduced by cooling plates of variable diameter  $d_C$  as shown in fig. 33.

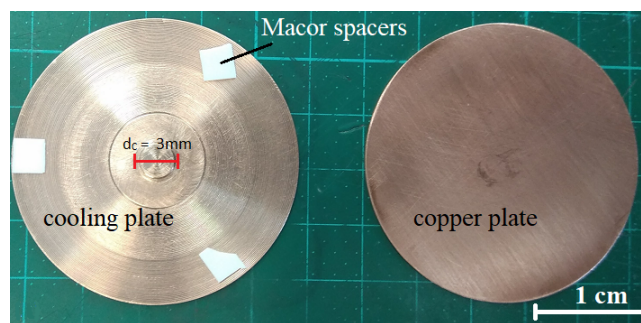


Figure 33: (a): Example of copper plates for connection of target to the cooling system used during the experiments, left copper plate has a total diameter of 50.4 mm and a cooling plate diameter  $d_C = 3$  mm at 1 mm height and is coupled to the flat copper plate on the right with 50.4 mm diameter at 1 mm height, Macor<sup>®</sup> spacers of 0.75 mm height are positioned in between to avoid additional heat contact

The calculations and simulations of the temperature and temperature gradient across the target surface are given in section 4.1, the measurements of the target temperature are presented in section 4.2.

#### 4.1 Calculations of the Target Temperature in a 1D Model and Simulations

The diameter  $d_C$  and position of the contact area determine the target temperature and gradient. The diameter of the contact area determines the maximum temperature and the temperature gradient at the target surface during the sputter process. The target temperature has three main contributions (fig. 34):

- heat flux from the plasma to the target:  $\varepsilon_P^T$
- radiative losses mainly at the target surface:  $-\sigma A_T \xi_R^V T_T^4$
- radiative influx from the heated substrate and chamber walls:  $\sigma A_T \xi_R^{Cu} T_S^4$

Fig. 34 shows an illustration of the one dimensional approach.

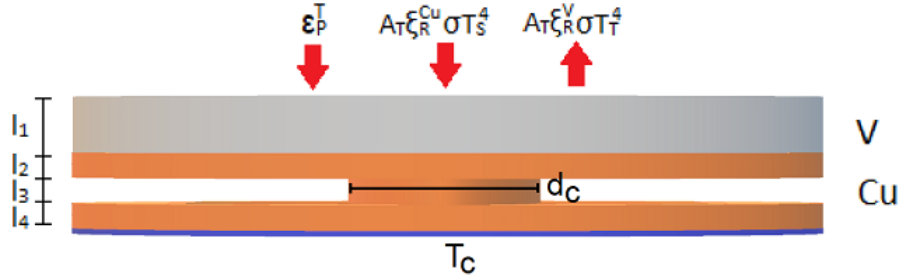


Figure 34: *Illustration of the variables in the one dimensional model for the calculation of the heat flux and target temperature, explanation in the text*

Starting from a simple one dimensional model the heat flux  $\frac{dQ}{dt}$  through a surface  $A$  in a medium with thermal conductivity  $\lambda$  is given by Fourier's law [77]:

$$\frac{dQ}{dt} = -A(x) \lambda(x) \frac{dT}{dx} \quad (19)$$

The internal energy in a volume  $dV$  is connected to the heat flux by:<sup>12</sup>

$$\frac{dU}{dt} = -\frac{d}{dx} \left( A(x) \lambda(x) \frac{dT}{dx} \right) \quad (20)$$

<sup>12</sup>In a volume  $dV = dAdx$  the change in internal energy  $dU = c_P dV dT$  is determined by the

The stationary solution of eq. 20 yields upon integration:<sup>13</sup>

$$-A(x) \lambda(x) \frac{dT}{dx} = E_P \quad (21)$$

Here,  $E_P$  defines the total heat flux per unit volume. In the case of reduced target cooling with a vanadium target of surface area  $A_T$  the constraints following fig. 34 are given by:

$$\begin{aligned} A_T \lambda_V & \quad \{0 < x < l_1 \\ A_T \lambda_{Cu} & \quad \{l_1 < x < l_1 + l_2 \\ A_C \lambda_{Cu} & \quad \{l_1 + l_2 < x < l_1 + l_2 + l_3 \\ A_T \lambda_{Cu} & \quad \{l_1 + l_2 + l_3 < x < l_1 + l_2 + l_3 + l_4 \\ T(l_1 + l_2 + l_3 + l_4) & = T_C = 292K \end{aligned} \quad (22)$$

Where  $A_T$  is the target surface area and  $\lambda_V$  the thermal conductivity of vanadium.  $A_C$  is the contact area between target and cooling plate which in turn is determined by the cooling plate diameter  $A_C = \left(\frac{d_C}{2}\right)^2 \pi$ . The fifth condition states that the capacity of the cooling system is infinite and therefore the cooling temperature  $T_C$  is constant. By rewriting and integrating eq. 21, the temperature difference between the surface  $T_T$  and the back of the cooling plate  $T(l_1 + l_2 + l_3 + l_4) = T_C$  is then equivalent to:

$$T_T - T_C = E_P \cdot \int_0^{l_1+l_2+l_3+l_4} \frac{1}{A(x) \lambda(x)} dx \quad (23)$$

The total heat flux  $E_P$  is given by the heating power of the plasma at the target surface  $\varepsilon_P^T$ , the radiative power due to the heated substrate holder  $\sigma A \xi_R^{Cu} T_S^4$  and the radiative losses at the target surface  $-\sigma A \xi_R^V T_T^4$  as seen in fig. 34.<sup>14</sup> The value  $\xi_R^V$  and  $\xi_R^{Cu}$  are the respective emissivities of the surfaces. For polished and unoxidized copper the emissivity is estimated by  $\xi_R^{Cu} = 0.57$  [78, 79] between 200 °C and 600 °C. For polished and unoxidized vanadium, the emissivity at 300°C was estimated to be

---

difference between the energy flux at the point  $x$  and  $x+dx$  hence  $\underbrace{\frac{dQ}{dt} \Big|_{x+dx} - \frac{dQ}{dt} \Big|_x}_{-\frac{d}{dx} (A \lambda \frac{dT}{dx})} = \frac{dU}{dt} = c_P dV \frac{dT}{dt}$ .

The stationary solution is given by  $\frac{dT}{dt} = 0$ . This yields  $-\frac{d}{dx} (A \lambda \frac{dT}{dx}) = 0$  and therefore  $-A \lambda \frac{dT}{dx} = \epsilon_P$ , where  $\epsilon_P$  is the total heat flux.

<sup>13</sup>The stationary solution is given by  $\frac{dU}{dt} = 0$ . This yields  $-\frac{d}{dx} (A \lambda \frac{dT}{dx}) = 0$  and therefore by integration  $-A \lambda \frac{dT}{dx} = \epsilon_P$

<sup>14</sup>The influx coming from the substrate holder is given by the Stefan-Boltzmann law  $\frac{dQ_R}{dt} = \sigma \xi_R A T^4$  where  $\sigma = 5.67 \cdot 10^{-8} \text{ W m}^{-2} \text{ K}^{-4}$  is the Stefan-Boltzmann constant and  $\xi_R$  the emissivity of a real surface.

$\xi_R^V = 0.08$  [80] and assumed to be constant in the range of interest. Assuming a substrate temperature of  $T_S = 673K$  and the surface of the substrate holder  $A_S$  to be completely covered by the target, the radiative power due to the heated substrate holder becomes  $\frac{dQ_R^S}{dt} \cong \sigma A_T \xi_R^{Cu} T_S^4$ . At the same time the target is losing the flux  $\frac{dQ_R^T}{dt} = -\sigma A_T \xi_R^V T_T^4$  at its surface. Therefore,  $E_P \cong \varepsilon_P^T + \sigma A_T \xi_R^{Cu} T_S^4 - \sigma A_T \xi_R^V T_T^4$  and defining the heating power of the plasma per unit area  $e_P^T = \frac{\varepsilon_P^T}{A_T}$  this can be simplified to  $E_P = A_T (e_P^T + \sigma (\xi_R^{Cu} T_S^4 - \xi_R^V T_T^4))$ . Eq. 23 then becomes:

$$T_T - 292 = (e_P^T + \sigma (\xi_R^{Cu} T_S^4 - \xi_R^V T_T^4)) \int_0^{l_1+l_2+l_3+l_4} \frac{A_T}{A(x) \lambda(x)} dx \quad (24)$$

The solution to this equation is calculated by integration:<sup>15</sup>

$$T_T = (e_P^T + \sigma (\xi_R^{Cu} T_S^4 - \xi_R^V T_T^4)) \left( \frac{l_1}{\lambda_V} + \frac{A_T}{A_C} \frac{l_3}{\lambda_{Cu}} + \frac{l_2 + l_4}{\lambda_{Cu}} \right) + 292 \quad (25)$$

Using the real values of the sputter system <sup>16</sup> and  $A_C = \left(\frac{d_C}{2}\right)^2 \pi$ , eq. 25 yields:

$$T_T = 292 + (10^5 + 5.67 \cdot 10^{-8} \cdot (0.57 \cdot 673^4 - 0.08 \cdot T_T^4)) \left( 8.3 \cdot 10^{-5} + \frac{1.6 \cdot 10^{-9}}{d_C^2} \right) \quad (26)$$

This equation can only be solved implicitly as  $T_T$  is inseparable. The resulting surface temperatures using the cooling plate diameters from the reduced target cooling experiments are given in table 4.

$d_C$ [mm]	$T_T$ [°C]
10	29
6	32
2	70
1	198
0	$\infty$

Table 4: Calculated target temperatures  $T_T$  from eq. 26 by implicit calculation for different cooling plate diameters  $d_C$

The simple model shows at least qualitatively the increasing temperature change with

$$\overline{^{15}T(0) - 292 = e_P^T + \sigma (\xi_R^{Cu} T_S^4 - \xi_R^V T_T^4) \left[ \frac{1}{\lambda_V} \int_0^{l_1} dx + \frac{1}{\lambda_{Cu}} \int_{l_1}^{l_1+l_2} dx + \frac{1}{\lambda_{Cu}} \frac{A_T}{A_C} \int_{l_1+l_2}^{l_1+l_2+l_3} dx + \frac{1}{\lambda_{Cu}} \int_{l_1+l_2+l_3}^{l_1+l_2+l_3+l_4} dx \right] = (e_P^T + \sigma (\xi_R^{Cu} T_S^4 - \xi_R^V T_T^4)) \left( \frac{l_1}{\lambda_V} + \frac{A_T}{A_C} \frac{l_3}{\lambda_{Cu}} + \frac{l_2+l_4}{\lambda_{Cu}} \right)}$$

<sup>16</sup> $l_1 = 0.003$  mm,  $l_{2,3,4} = 0.001$  mm,  $\lambda_V = 36$  Wm<sup>-1</sup>K<sup>-1</sup>,  $\lambda_{Cu} = 400$  Wm<sup>-1</sup>K<sup>-1</sup>,  $A_T = (0.0254)^2 \pi = 0.002$  m<sup>2</sup> mm and  $\varepsilon_P^T = 200$  W [81]

decreasing cooling plate diameters although the values seem to be quite low. For a more accurate calculation and view of the temperature gradient across the target surface, the real configuration of the target and the cooling plate was implemented into *Solidworks 2017* and simulated with various cooling plate diameters and the heated substrate holder positioned at a distance of 50 mm from the target surface. An image of the configuration used to simulate the target temperature and gradient across the surface is given in fig. 35.

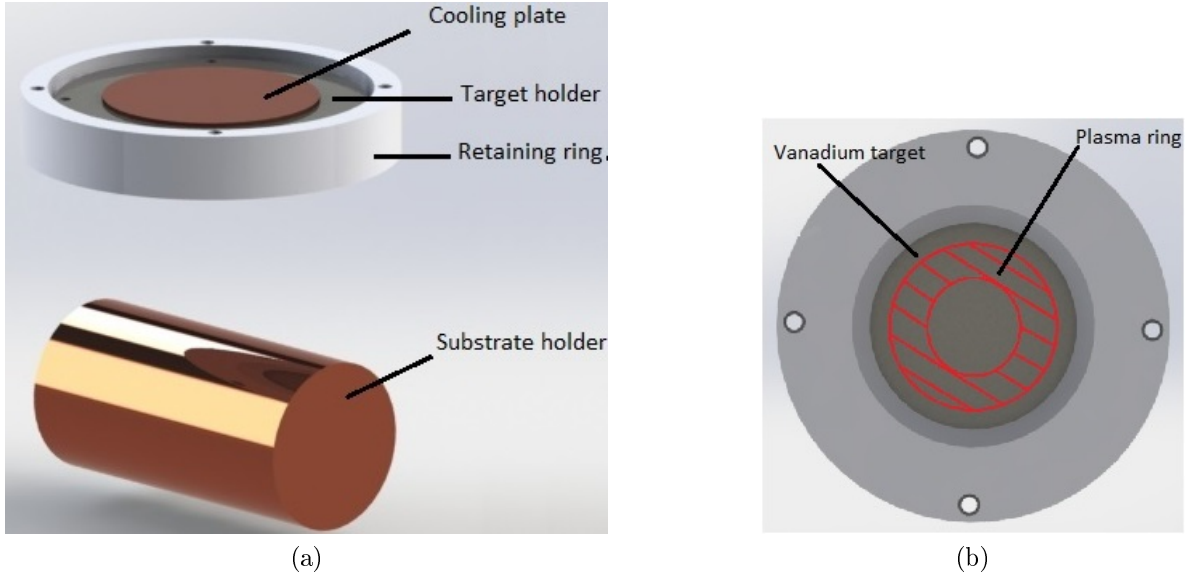


Figure 35: (a) assembly of target holder with mounted vanadium target, cooling plates and heatable substrate holder used for the simulations in *Solidworks 2017* with different  $d_C$ ; (b) view of the vanadium target and marking (red) of the assumed area where the plasma ring forms

In the “static temperature simulation” of *Solidworks 2017*, the boundary conditions were set as follows:

- The temperature at the back of the cooling plate to  $T_C = 292$  K
- The ambient temperature to 300 K
- The plasma ring was limited to the circular area (red area in fig. 35(b)) where the magnetic field is present and the heating power set to  $e_P = 200$  W
- the surface temperature of the substrate holder to  $T_S = 673$  K

- The emissivities to  $\xi_R^{Cu} = 0.57$  and  $\xi_R^V = 0.08$  [? 10]
- The target holder is only connected to the chamber by four stainless steel screws and so this heat-flux and losses are neglected

The values for the maximum temperature in the plasma tube as well as the mean temperature are given in table 5, the simulated target surfaces are listed in the appendix.

$d_C$ [mm]	$T_T^{max}$ [°C]	$T_T^{mean}$ [°C]
10	142	132
6	206	187
2	547	536
1	1206	1202
0	3673	3669

Table 5: *simulated target temperatures  $T_T^{max}$  and  $T_T^{mean}$  with assembly in fig. 35 for different cooling plate diameters  $d_C$*

The target temperatures could at this point not be quantified by experiments except the measurements with  $d_C = 0$  mm where a dark-red glow (600 °C-700 °C) could be observed directly after deposition. The temperatures for this diameter are  $T_T^{mean} = \infty$  in the one dimensional model and  $T_T^{mean} = 3669^\circ C$  in the simulations which both overestimate the real value. Although the one dimensional model and the simulations both show a decreasing target temperature for increasing cooling plate diameter, there are three main issues when interpreting the static calculations:

- The parameters emissivity, ambient temperature and heating power are not necessarily valid as neither the exact surface roughness is known for the copper and the vanadium parts nor the thermal influx of the plasma at the target surface
- The components are assumed to be in perfect contact like the target and the target holder, which in reality will not hold

## 4.2 Indirect Measurement of the Target Surface Temperature and Modeling

The calculations had to be quantified by measuring the target temperature. As the direct measurement of the target temperature at the target surface during the reactive sputter process is not possible due to the high voltage applied to the target and the

presence of a plasma, an indirect method was elaborated. In this process, a stainless steel ring was designed and mounted between the target and the substrate holder at a distance of 20 mm from the target surface and 30 mm from the substrate holder. The ring is equipped with a clamp to pin down a thermocouple and a hole of 2.5 mm diameter for the mounting of a PT100 thermal resistor. The ring was grounded and therefore a safe temperature read-out was possible during the measurements. The ring was mounted by two stainless steel screws to the target casing. An illustration of the assembly is shown in fig. 36.

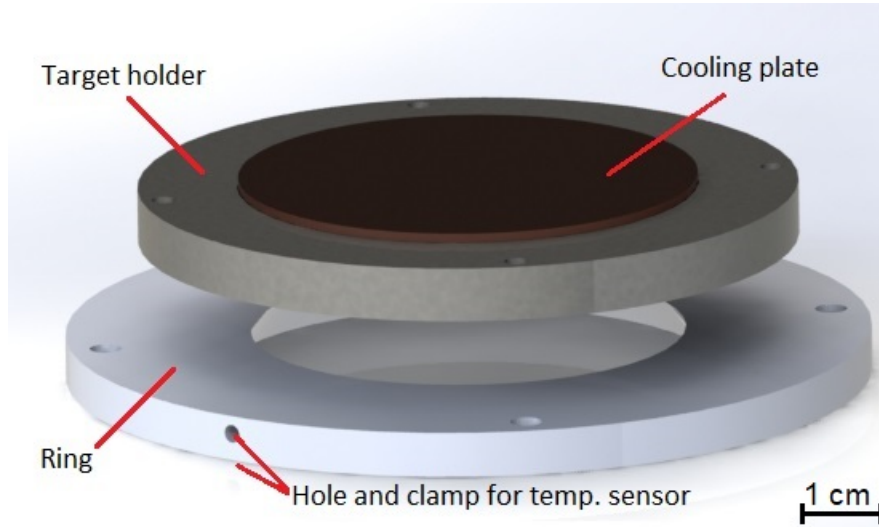


Figure 36: *Positioning of the stainless steel ring beneath the target for an indirect measurements of the target surface temperature*

Because the method is indirect, the individual contributions to the temperature at the ring had to be considered: ( $\xi_R^i$  describes the emissivities of the individual surfaces)

- radiative influx from the heated substrate holder:  $\propto \sigma T_S^4 \xi_R^u$
- radiative influx from the target surface:  $\propto \sigma T_T^4 \xi_V$
- radiative losses:  $= -\sigma A_R T_R^4 \xi_{st}$  where  $A_R$  is the surface of the stainless steel ring,  $T_R$  the temperature of the ring and  $\xi_{st}$  the emissivity of stainless steel
- heat transfer due to the particle influx from the target during the sputter process:  $= f(T_T)$
- due to the minimal contact of the ring to the chamber by two stainless steel screws the losses due to thermal conductivity are neglected

The individual radiative contributions must take the geometry into account. This is done by adding factors  $\tilde{g}$  to the radiative terms  $\propto \sigma T_i^4 \xi_i$  and must be evaluated individually. Because  $\sigma \cdot \xi_i$  is a constant the term  $\tilde{g}_i \cdot \sigma \cdot \xi_i$  is subsumed into  $g_i$ . Further, the function  $f(T_T)$  describing the heat flux from the sputtered particles is unknown but can be measured at full target cooling, where the target is assumed to have the same temperature as the cooling system. The function is proportional to the temperature dependent sputter yield  $f(T_T) \propto Y(T_T)$ . The sputter yield does however not increase significantly over temperature up to the melting point of the target material [12]. We assume the function  $f(T_T)$  therefore to be constant in our case. The total change of the internal energy of the stainless steel ring can then be generally expressed by<sup>17</sup>:

$$c_p^{st} V_R \frac{dT_R}{dt} = g_S T_S^4 + g_T T_T^4 - g_R (T_R^4 - T_{room}^4) + f \quad (27)$$

Here,  $c_p^{st}$  is the specific heat of stainless steel and  $V_R$  the volume of the ring, together with  $g_R = \sigma A_R \xi_{st}$  are the only known factors in in eq. 27. The System is in a thermal equilibrium state, so the left hand side vanishes leaving:

$$g_S T_S^4 + g_T T_T^4 - g_R (T_R^4 - T_{room}^4) + f = 0 \quad (28)$$

Therefore, three parameters  $g_S$ ,  $g_T$  and  $g_R$  had to be determined empirically in a thermal equilibrium, which was assumed at a temperature change below  $10^{-2} Ks^{-1}$  at the ring. Using a cooled target ( $T_T = 18^\circ C$ ), the impact of the heated substrate holder alone at  $T_S = 400^\circ C = 673 K$  was measured to be  $T_R = 120^\circ C = 393 K$ , starting from  $T_{room} = 26^\circ C = 299 K$ . Without further contributions eq. 28 then simplifies to  $g_S T_S^4 = g_R (T_R^4 - T_{room}^4)$  from which follows that  $g_S = 8.81 \cdot 10^{-15} WK^{-4}$ . The parameters  $g_T$  and  $f$  still had to be fixed. Therefore, at least two temperatures at the ring with a known temperature at the target surface had to be measured. The constants can then be extracted at known  $T_S$ ,  $T_R$  and  $T_T$  by:

$$g_T T_T^4 + f = 1.14 \cdot 10^{-13} \cdot (T_R^4 - T_{room}^4) - 8.81 \cdot 10^{-15} \cdot 673^4 \quad (29)$$

In order to obtain at least two target temperatures, several attempts were made:

---

<sup>17</sup>  $g_S = \tilde{g}_S \sigma \xi_{Cu}$ ,  $g_T = \tilde{g}_T \sigma \xi_V$ ,  $g_R = \sigma A_R \xi_{st}$  where the factor  $g_R = 1.14 \cdot 10^{-13}$  is the only known one and is composed of  $A_R = 2 \cdot 10^{-5} m^2$ , the assumed mean emissivity of polished steel between room temperature and  $800^\circ C$  of approximately  $\xi_{st} = 0.15$  calculated from [82] and the Stefan-Boltzmann constant  $\sigma$ . The volume of the ring is given by  $V_R = 2 \cdot 10^{-5} m^3$  and the heat capacity by  $c_p^{st} = 400 WKs^{-1}m^{-3}$ .

- At full target cooling  $d_C = 50.8$  mm the surface temperature was assumed to be equal to the temperature at the cooling system  $T_2 = 292$  K which fixes one of the two parameters.
- A thermosensor (thermocouple type K) was attached to the target surface so that both cables had the same high voltage. The cables were not measured till the plasma and the high voltage was turned off. After turning off the power, the ends of thermosensor were directly measured using a Eurotherm thermocontrol. However, the thermocouples melted under strong sparking directly after the plasma ignition.
- Constructing a thermosensor attached to the substrate holder (thermocouple type K) which could be turned to touch the target surface directly after the sputter process. Due to geometrical issues and a lack of controllability this device could not be used.
- Estimating the target temperature by using a thin nickel foil of 2 mm thickness (two pins of 1 mm pressed together) detached from the cooling system. At this thickness a weakened magnetic field can permeate the ferromagnetic material and ignite the plasma. The idea was to heat the target above its Curie temperature where the ferromagnetism vanishes and the magnetic field lines from the magnetron could unimpaird pass through the nickel target. Above the Curie temperature of nickel  $T_{Curie}^{Ni} = 631$  K [83] the voltage and the current (at fixed power) should change. When using low power levels and thus a slow heating of the target surface and consequently a slow temperature change at the ring, a quasi-equilibrium ring temperature could be assumed. The temperature of the ring at the moment of voltage/current change would correspond to the Curie temperature at the target. Using a nickel target, the lowest possible settings for igniting a magnetron plasma were a power level of 15 W and an argon pressure of 1 Pa. Voltage, Current and ring temperature were recorded simultaneously. The nickel target was heated several times for 30 minutes till a light red glow started and thus the Curie temperature was clearly exceeded. The ring was heating up but neither the voltage nor the current showed any significant changes during the heating or cooling cycles.

Hence, the indirect measurement of the target temperature was not quantifiable. However, qualitatively the heating effect of the reduced target cooling could be detected

using the ring. Therefore the substrate was not heated so that the only source of heat transfer was coming from the target. The measurements of the ring temperature were carried out at a relatively high chamber pressure of 2.1 Pa as this pressure was used for the production of vanadium dioxide thin films in section 5.1.2. At the end of this work, where the temperature measurements were carried out, the turbomolecular pump *Alcatel 5402 CP* started to reduce the rotational speed of 25000 rpm at the relatively high chamber pressures after about five minutes. Thus, the ring temperature could be recorded only until the turbomolecular pump started reducing the pumping speed. In table 6 the results of the temperature change at the ring  $\Delta T_R = T_R^{end} - T_R^{start}$  at different cooling plate diameters  $d_C$  is shown. The equilibrium temperature before sputtering is  $T_R^{start}$  and  $T_R^{end}$  is the temperature of the ring right after the end of the sputtering process. Sputtering lasted five minutes at 2 Pa argon pressure, 0.1 Pa of oxygen partial pressure at a power level of 200 W. The substrate holder was not heated.

$d_C$ [mm]	$T_R^{start}$ [°C]	$T_R^{end}$ [°C]	$\Delta T_R$ [K]
50.8	25	63.4	38.4
10	26	68.2	42.2
4	26	75.5	49.5
2	26.8	81.2	54.4

Table 6: *Measured temperature changes  $\Delta T_R$  at the ring, starting from an equilibrium temperature  $T_R^{start}$  at different cooling plate diameters  $d_C$  after 5 minutes*

From the values in table 6 it can be concluded, that the ring temperature and thus the gradient  $\frac{dT_R}{d(d_C)}$  increase with reducing cooling plate diameter, in accordance to the calculations and simulations.

## 5 Analysis of as-deposited $VO_2$ thin films produced by reactive DC magnetron sputtering

In the previous chapter the target temperature was investigated and qualitatively analyzed by simulating, calculating and indirectly measuring the target surface temperature. In the following sections the parameters of the sputter system that were varied during the deposition of vanadium oxide thin films, are given. The optimum set of parameters at fully cooled target for the production of thin films containing crystalline vanadium dioxide and/or showing a thermochromic behaviour is given. The

thermochromic samples of the measurements at full target cooling are then analyzed followed by the investigation of the measurements at reduced target cooling in dependence of the cooling plate diameter  $d_C$ .

## 5.1 Parameter Variation in reactive DC Magnetron Sputtering for as-deposited Crystalline $VO_2$ Thin Films

Following the current developments in the production of  $VO_2$  thin films, the aim of the experiments was, to produce pure crystalline  $VO_2$  thin films by reactive DC magnetron sputtering at low substrate temperatures and without further thermal annealing. A metallic two inch (50.8 mm) diameter, 3 mm thick vanadium target (99.9 %) from *Kurt J. Lesker* was used for the deposition. The produced thin films and their properties were mainly studied by four-point-probe and XRD-measurements. The parameters which were varied at full target cooling are:

- The argon pressure/flow: from 0.2 Pa to 2 Pa, corresponding to an argon flow between 3.8 sccm and 48 sccm
- The oxygen partial pressure/flow: from 0.05 Pa to 0.3 Pa, corresponding to an argon flow of 2 sccm to 6 sccm.
- The substrate surface temperature: from room temperature to 400 °C
- The power applied to the two inch target: from 60 W to 300 W

Further, the influence of the target temperature on the deposition of crystalline  $VO_2$  thin films was studied after fixing the other parameters to their optimum values. In this process the target was heated by reducing the contact-area between the vanadium target and the water-cooling cycle as explained in chapter four. The contact area was varied between a diameter of 50.8 mm (full contact) and 1 mm of the bottom center, circular contact surface. Therefore, the following measurements are subdivided into two groups:

- measurements done with full target cooling
- measurements done with reduced target cooling

The variation of parameters at full target cooling was done consecutively for 90 samples to find an optimum set of parameters for the production of thin films with thermochromic behaviour. Even though only 7 out of 90 samples showed  $VO_2$  to be present

in the XRD scans and the thermochromic behaviour associated with  $VO_2$ , the parameters could be roughly limited to the following regions:

- The power should be set to 200 W. A further increase up to 300 W did not enhance the formation of thermochromic films and higher power levels were not tested as the maximum recommended power for the 50.8 mm vanadium target is given by Kurt J. Lesker to be  $7 \text{ W cm}^{-2}$  [84]. The power was therefore set to 200 W throughout the deposition experiments.
- The substrate temperature had to be at 370 °C to 400 °C which is the maximum temperature achievable with the current setup without the risk of damaging the system.
- The oxygen partial pressure  $p_O$  must correspond to a region quite after the increase in total pressure which is observable upon transition from the metallic to the poisoned sputter mode (see section 2.1.3 for examples), which was found to be between 0.05 Pa to 0.075 Pa at a power level of 200 W and independent of the argon pressure. During the experiments with reduced target cooling, the onset of the poisoned sputter mode ranged from 0.1 Pa to 0.15 Pa oxygen partial pressure. During the experiments with full and reduced target cooling, thermochromism was very sensitive to changes of the oxygen partial pressure above and below these values.
- The ratio  $r_O^{Ar} = \frac{p_O}{p_{Ar}}$  of oxygen partial pressure  $p_O$  to argon pressure  $p_{Ar}$  should be small. The optimum argon pressure was thereby found to be the maximum possible value of 2 Pa. At a chamber pressure of about 2.3 Pa the vacuum pump *Alcatel 5402 CP* started to reduce the pumping speed which had to be avoided.

The heated samples were at least cooled down to 90 °C before taking them out of the chamber after deposition to prevent further oxidation processes. The cool-down temperature of 90 °C was assumed to be sufficient because the heated four-point measurements require temperatures up to 95 °C and therefore one must take possible oxidation into account anyway. The vanadium target was pre-sputtered for three minutes before adding the reactive gas. The oxygen flow was increased till the chamber pressure started to rise and the transition into the poisoned mode started. As this region was unstable we waited additional three to five minutes before coating the substrate to let the pressure stabilize between 0.05 to 0.075 Pa. The pressure did not totally stop increasing during

the coating of the substrate at a rate of around  $\leq 9 \cdot 10^{-5} \text{ Pa} \cdot \text{s}^{-1}$  which may arise from the fact that the transition region was not fully overcome and thus the target not fully poisoned. However, this region was the only one to allow the production of  $\text{VO}_2$  thin films with thermochromic properties at full target cooling. During the reduced target cooling measurements this region shifted to higher flow rates and oxygen partial pressures of 0.1 to 0.15 Pa but with a clearly enhanced reproducibility of the thermochromic effect in the deposited films.

### 5.1.1 Analysis of $\text{VO}_2$ Thin Films produced with full Target Cooling

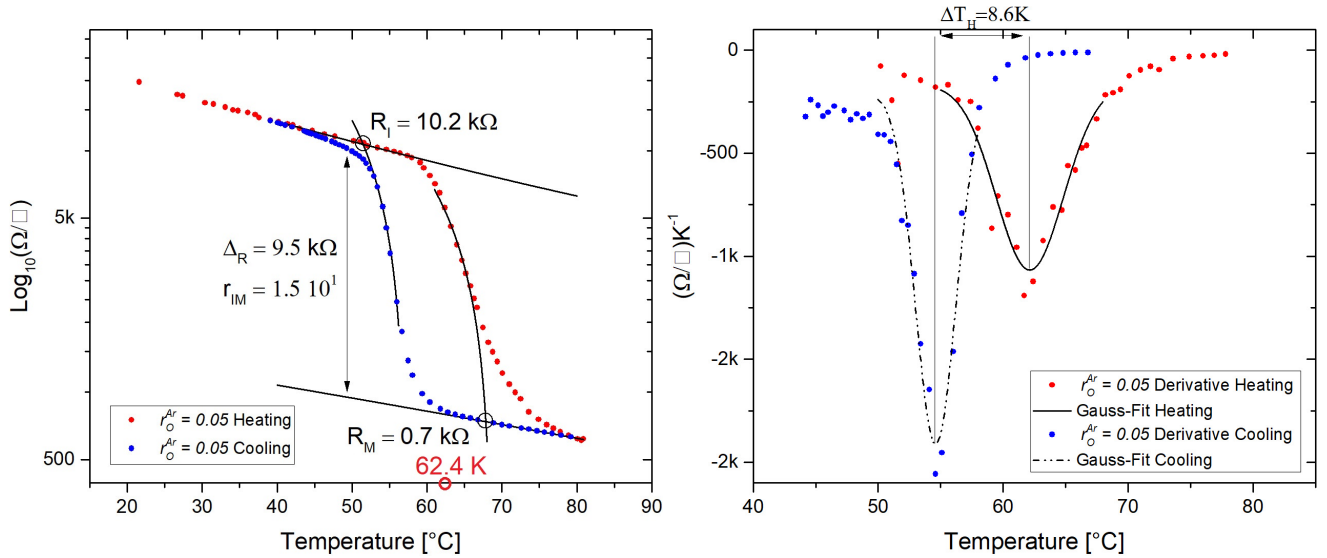
The set of parameters leading to crystalline  $\text{VO}_2$  was found to be very sensitive to slight changes in the oxygen partial pressure and always led to the formation of other oxides of vanadium which in the most cases overlaid and diminished the SMT of the  $\text{VO}_2$  thin films. Because of that, the measurements could hardly be reproduced using the same settings, so that from 89 measurements only 7 of them showed thermochromic behaviour. As mentioned in the previous section, the ratio  $r_O^{\text{Ar}} = \frac{p_O}{p_{\text{Ar}}}$  of oxygen partial pressure  $p_O$  to argon pressure  $p_{\text{Ar}}$  was found to be crucial for the production of thin films showing thermochromic properties. To provide an insight of the findings during the parameter variation at full target cooling, some samples are analyzed in the following, including the optimum set of parameters, shown in table 7. The settings were the same for all samples in this table except for the ratio  $r_O^{\text{Ar}}$  and the sputter time.

<i>sample name</i>	$r_O^{\text{Ar}} = \frac{p_O}{p_{\text{Ar}}}$	$\text{Ar} \frac{p_{\text{Ar}} [\text{Pa}]}{f_{\text{Ar}} [\text{sccm}]}$	$\text{O}_2 \frac{p_O [\text{Pa}]}{f_O [\text{sccm}]}$	$\frac{\text{Sputter time [s]}}{\text{Thickness [nm]}}$
VOX85	0.025	$\frac{2}{47.85}$	$\frac{0.055}{2.70}$	$\frac{900}{432}$
VOX86	0.025	$\frac{2}{47.86}$	$\frac{0.055}{2.75}$	$\frac{900}{432}$
VOX71	0.033	$\frac{1.5}{34.0}$	$\frac{0.057}{2.5}$	$\frac{600}{288}$
VOX51	0.05	$\frac{1}{[\text{sccm}]}$	$\frac{0.05}{2}$	$\frac{1400}{672}$

Table 7: *Sample name, ratio of oxygen to argon pressure  $r_O^{\text{Ar}}$ , argon pressure  $p_{\text{Ar}}$ , oxygen pressure  $p_O$  and corresponding flow rates and sputter times and corresponding film thicknesses from the list of experiments in appendix B; all films were produced at 200 W, full target-cooling and a substrate temperature of 370 °C.*

The samples given in table 7 are in the following analyzed according to their individual

ratio  $r_O^{Ar}$ . The samples in the table are marked green in the table of experiments in appendix B. In fig. 37 the hysteresis, sheet resistivity and the fitted derivatives of sample VOX51 produced at  $r_O^{Ar} = 0.05$  are shown.



(a) Sample VOX51 four-point probe measurement (b) Sample VOX51 derivative of four-point probe measurement

Figure 37: (a) Four-point measurement of sample VOX51 produced at  $r_O^{Ar} = 0.05$ , with resistivity change  $r_{IM} = 15$  and total resistivity change  $\Delta_R = 9.5 \text{ k}\Omega$ ; (b) derivatives in the heating and cooling cycle (indicated in red and blue respectively) yielding a hysteresis width of  $\Delta T_H = 8.6 \text{ K}$  and transition temperature  $T_{trans} = 62.4 \text{ K}$

Like for all samples produced at full target cooling showing a SMT, the resistivity change is relatively small with a value of  $r_{IM} = 15$  at a total resistivity change of  $\Delta_R = 9.5 \text{ k}\Omega$ . The hysteresis and transition temperature of this sample were calculated to be  $\Delta T_H = 8.6 \text{ K}$  and  $T_{trans} = 62.4 \text{ K}$ . Looking at the XRD scan in fig. 38, one can identify three different oxidation states of vanadium, namely orthorhombic  $V_2O_5$ , monoclinic  $V_6O_{13}$  and monoclinic  $VO_2$ .

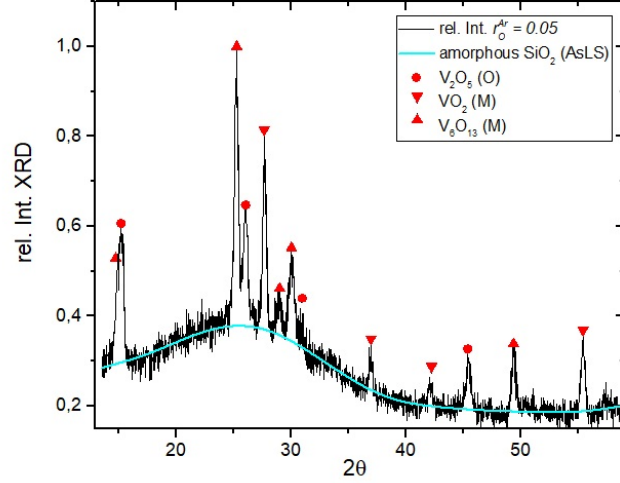
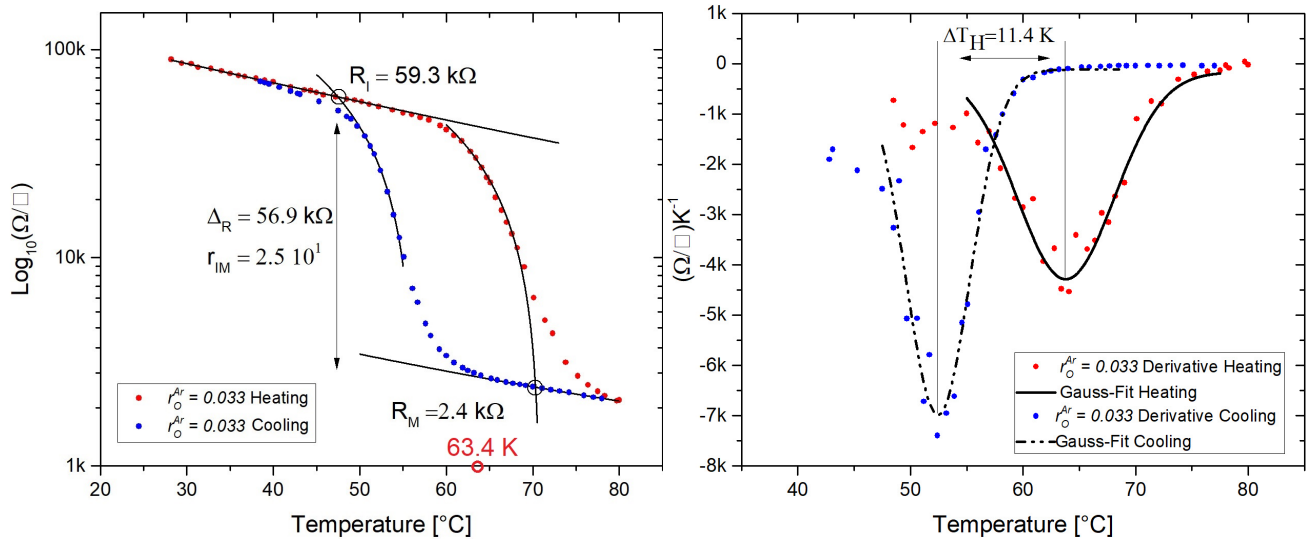


Figure 38: *GIXRD scan at  $\alpha = 5.5^\circ$  of sample VOX51 produced at  $r_O^{Ar} = 0.05$ , normalized to the maximum intensity and assignment of the identified peaks to  $VO_2(M)$ ,  $V_2O_5(O)$  and  $V_6O_{13}(M)$  using HighScore Plus; the broad peaks from the amorphous glass substrate were determined by AsLS fitting*

Upon lowering the ratio of oxygen partial pressure to argon pressure by rising the argon pressure to 1.5 Pa, corresponding to a ratio of  $r_O^{Ar} = 0.033$  (sample: VOX71) the resistivity change slightly increases to  $r_{IM} = 25$  at a total resistivity change of  $\Delta_R = 56.9 \text{ k}\Omega$  while the hysteresis became wider at  $\Delta T_H = 11.4 \text{ K}$  as shown in fig. 39. The sheet-resistivity starts at about  $90 \text{ k}\Omega/\square$  at room temperature, which is about half an order of magnitude more than in sample VOX51, the same holds for the total resistivity change. This may be attributed to the vanishing of the (thermochromic)  $V_6O_{13}$  phase, as can be extracted from the XRD scan in fig. 40.



(a) Sample VOX71 four-point probe measurement (b) Sample VOX71 derivative of four-point probe measurement

Figure 39: (a): Four-point measurement of sample VOX71 produced at  $r_O^{Ar} = 0.033$ , with a resistivity change  $r_{IM} = 25$  and total resistivity change  $\Delta_R = 56.9 \text{ k}\Omega$ ; (b): derivatives in the heating and cooling cycle (indicated in red and blue respectively) yielding a hysteresis width of  $\Delta T_H = 11.4 \text{ K}$  and transition temperature  $T_{trans} = 63.4 \text{ K}$

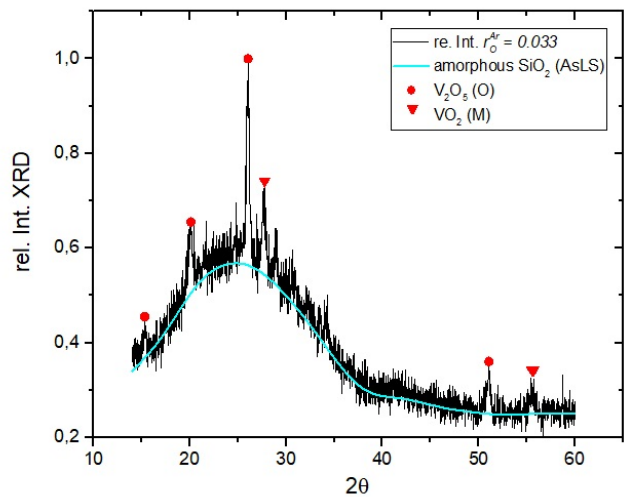


Figure 40: GIXRD scan of sample VOX71 produced at  $r_O^{Ar} = 0.033$  at  $\alpha = 5.5^\circ$ , normalized to the maximum intensity and assignment of the identified peaks to  $\text{VO}_2(M)$  and  $\text{V}_2\text{O}_5(O)$  using HighScore Plus; the broad peaks from the amorphous glass substrate were determined by AsLS fitting

In the XRD scan, monoclinic  $VO_2$  and orthorhombic  $V_2O_5$  could be identified. Upon further increasing the argon pressure to 2 Pa without changing the oxygen partial pressure, corresponding to a ratio of  $r_O^{Ar} = 0.025$ , the reproducibility slightly increased. However, the SMT of different samples produced under the same conditions were strongly dissimilar, indicating the coexistence of multiple oxides. Sample VOX86, produced at  $r_O^{Ar} = 0.025$ , is given in fig. 41.

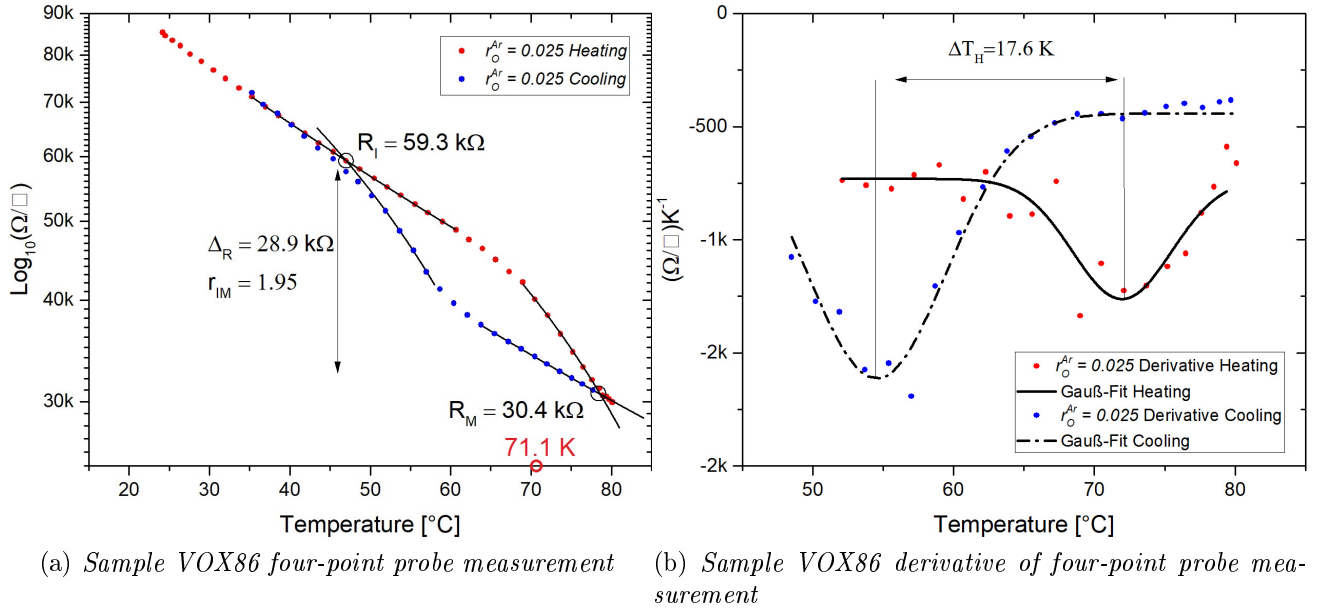


Figure 41: (a) Four-point measurement of sample VOX86 produced at  $r_O^{Ar} = 0.025$ , with resistivity change  $r_{IM} = 1.95$  and total resistivity change  $\Delta_R = 28.9 \text{ k}\Omega$ ; (b) derivatives in the heating and cooling cycle (indicated in red and blue respectively) yielding a hysteresis width of  $\Delta T_H = 17.6 \text{ K}$  and transition temperature  $T_{trans} = 71.1 \text{ K}$

The resistivity change is only  $r_{IM} = 1.95$  at a total value of  $\Delta_R = 28.9 \text{ k}\Omega$  while the hysteresis of this sample is calculated to be  $\Delta T_H = 17.6 \text{ K}$  and the transition temperature to be  $T_{trans} = 71.1 \text{ K}$ . In the XRD scan of this sample (fig. 42), one can hardly identify the monoclinic  $VO_2$  phase but a set of other oxides, mainly orthorhombic  $V_2O_5$  and monoclinic  $V_3O_7$ . These contribute to the strongly underlayed signal. Only one peak could be assigned to anorthic  $V_{14}O_6$  which is not enough for a verification of its presence in the thin film. Another sample produced at  $r_O^{Ar} = 0.025$  (VOX85) is shown in fig. 43. The four-point measurement shows no distinct transition.

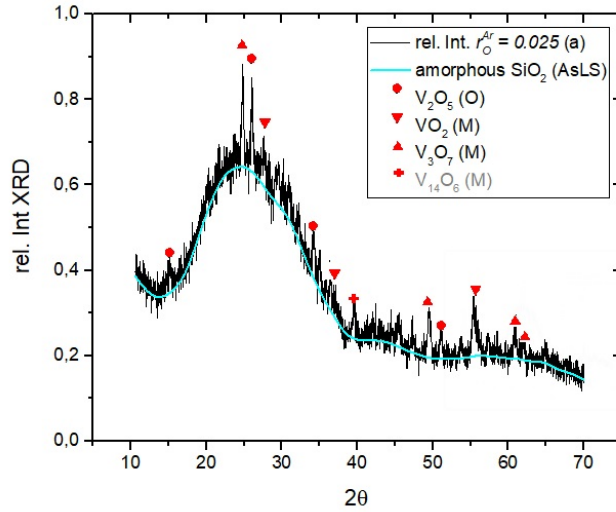


Figure 42: *GIXRD scan of sample VOX86 produced at  $r_O^{Ar} = 0.05$  (corresponding to index A in table 7) at  $\alpha = 5.5^\circ$ , normalized to the maximum intensity and assignment of the identified peaks using HighScore Plus to  $VO_2(M)$ ,  $V_2O_5(O)$ ,  $V_3O_7(M)$  and only one peak of  $V_{14}O_6(M)$  which is not enough for a verification; the broad peaks from the amorphous glass substrate were determined by AsLS fitting*

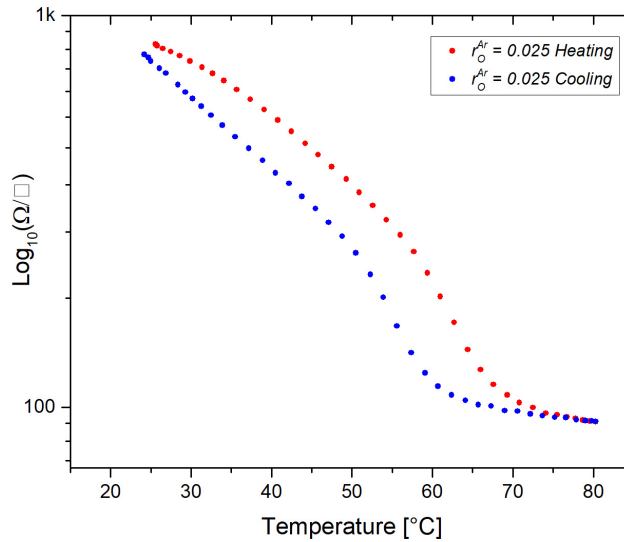


Figure 43: *Four-point measurement of sample VOX85 produced at  $r_O^{Ar} = 0.025$  showing a broad SMT and no distinct transition temperature*

Fig. 44 shows the corresponding XRD scan. A strong mixing of different oxides, namely orthorhombic  $V_2O_5$ , rhombohedral  $V_2O_3$  and only two peaks of monoclinic  $VO_2$  can be observed. The two discussed samples produced at  $r_O^{Ar} = 0.025$  (VOX85, VOX86) show

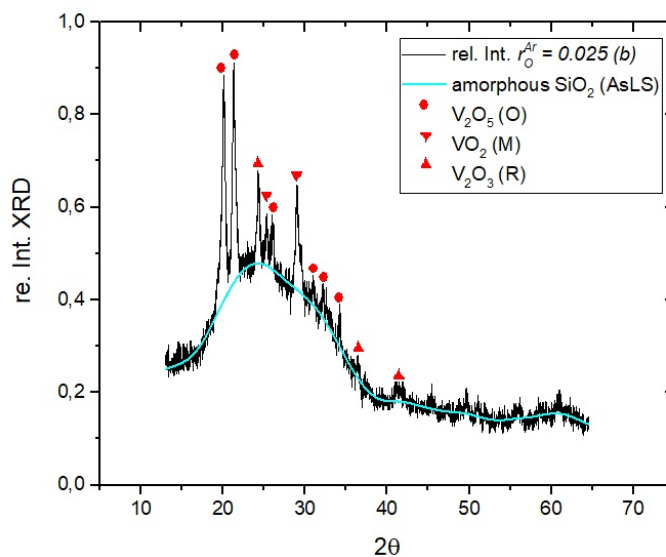


Figure 44: *GIXRD scan of sample VOX85 produced at  $r_O^{Ar} = 0.05$  (corresponding to index B in table 7) at  $\alpha = 5.5^\circ$ , normalized to the maximum intensity and assignment of the identified peaks using HighScore Plus to  $VO_2(M)$ ,  $V_2O_3(R)$  and  $V_2O_5(O)$ ; the broad peaks from the amorphous glass substrate were determined by AsLS fitting*

the strong variations of the quality of the SMT. Nevertheless, the better reproducibility in a sense that a thermochromic behaviour is observable, despite the strongly varying quality, indicates that minimizing the ratio  $r_O^{Ar}$  and at the same time sputtering at the very beginning of the poisoned mode most frequently yields thin films containing monoclinic  $VO_2$ .

### 5.1.2 Analysis of $VO_2$ Thin Films produced with reduced Target Cooling

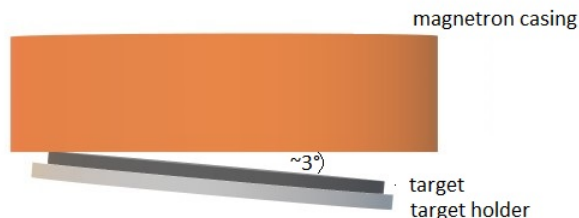


Figure 45: *Schematic illustration of the tilted assembly of the target due to a loose screw at the target holder; the tilting angle was approximately  $3^\circ$*

The technique of reduced target cooling improved not only the reproducibility but also the purity of the  $VO_2$  thin films. The concept of enhanced thermochromic films by

target heating during deposition was observed for the first time, when the target was not fully connected to the cooling system due to a loose screw which is shown schematically in fig. 45. The tilted assembly led to thin films with a narrow hysteresis and quite a big change of resistivity. Following this observation a systematic arrangement for reduced target cooling was elaborated. The controlled reduction of the heat transfer from the target by cooling plates of different diameters  $d_C$  was discussed in chapter four. The measurements were carried out at diameters  $d_C = 10$  mm, down to  $d_C = 1$  mm to find the optimum target temperature for the production of thermochromic thin films. In addition, measurements with no connection to the cooling system at all ( $d_C = 0$  mm) were performed.

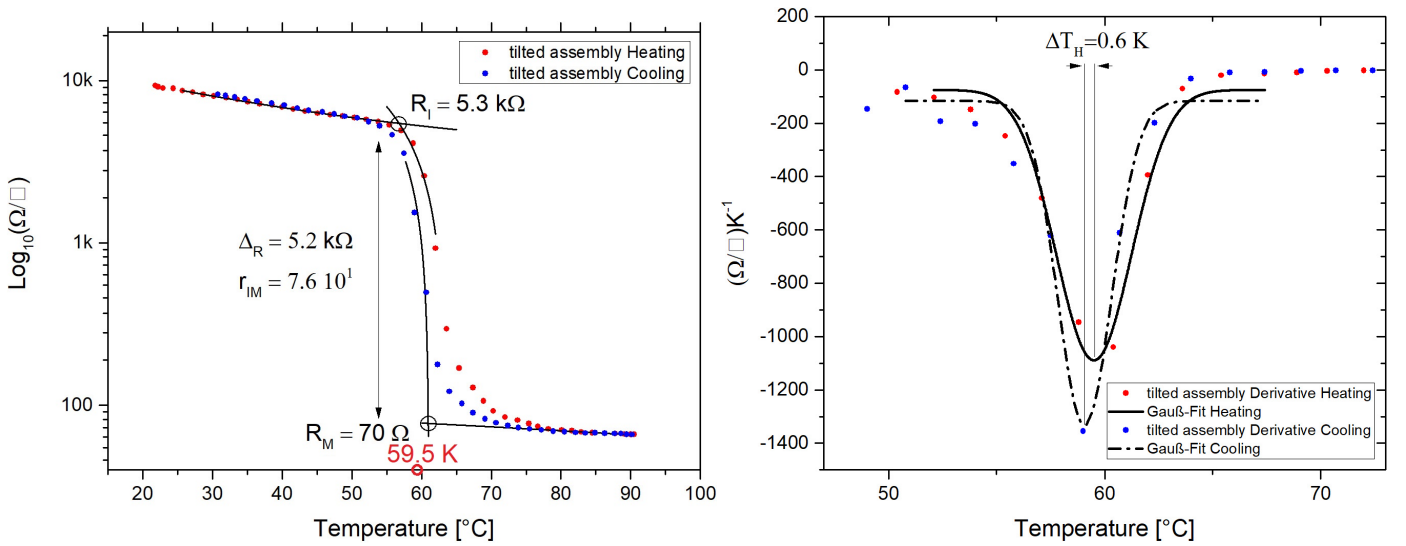
<i>sample name</i>	$\frac{d_C [mm]}{T_T [^\circ C]}$	$Ar \frac{[Pa]}{[sccm]}$	$O_2 \frac{[Pa]}{[sccm]}$	$\frac{Sputter Time [s]}{Thickness [nm]}$
VOX93	<i>tilted assembly</i>	$\frac{2}{47.4}$	$\frac{0.07}{3.5}$	$\frac{900}{432 (733 \text{ by SEM})}$
VOX100	$\frac{0 \text{ mm}}{600-700^\circ C}$	$\frac{2}{46.5}$	$\frac{0.08}{3.3}$	$\frac{150}{72}$
VOX103	$\frac{10 \text{ mm}}{\text{unk.}}$	$\frac{2}{47.5}$	$\frac{0.07}{3.5}$	$\frac{200}{96}$
VOX106	$\frac{6 \text{ mm}}{\text{unk.}}$	$\frac{2}{47.8}$	$\frac{0.075}{3.4}$	$\frac{300}{144}$
VOX118	$\frac{2 \text{ mm}}{\text{unk.}}$	$\frac{2}{47.8}$	$\frac{0.085}{4.5}$	$\frac{200}{96}$
VOX135	$\frac{1 \text{ mm}}{\text{unk.}}$	$\frac{20}{47.85}$	$\frac{1.1-1.25}{4.5}$	$\frac{400}{192}$

Table 8: *Sample name, cooling plate diameter  $d_C$  and estimated target temperature (unk.: unknown) argon/oxygen flow and pressure, sputter time and corresponding thickness in the measurement list in appendix B; all listed measurements were performed at a power of 200 W and a substrate temperature of 400 °C. All other parameters were fixed to the optimum values determined for a fully cooled target.*

In table 8, samples produced with different cooling plates are listed. The given samples in table 8 are the ones with the best thermochromic behaviour for the respective cooling plate diameter, the reproducibility is discussed in chapter six. In the following the samples are analyzed according to their respective cooling plate diameter  $d_C$  in table 8. The parameters argon pressure, ratio of oxygen and argon pressure, sputter power and substrate temperature, according to the findings during the measurements performed at full target cooling,  $p_{Ar} = 2 Pa$ ,  $r_O^{Ar} = 0.025 - 0.05$ ,  $P = 200 W$ , and  $T_S = 400^\circ C$

respectively, were used. The oxygen flow at which the hysteresis of the reactive sputter process started, slightly increased with decreasing cooling plate diameter. This is attributed to the increased sputter area with progressive target erosion and due to, yet not quantified, changes of the reactive sputter hysteresis itself because of the increasing target temperature.

Sample VOX93, shown in fig. 46 (corresponding to the *tilted assembly* in table 8) was also produced with a tilted assembly of the target and showed excellent thermochromic behaviour in the four-point measurements.



(a) Sample VOX93 four-point probe measurement

(b) Sample VOX93 derivative of four-point probe measurement

Figure 46: (a): Four-point measurement of a “tilted assembly” sample VOX93 with resistivity change  $r_{IM} = 76$  and total resistivity change  $\Delta_R = 5.2 \text{ k}\Omega$ ; (b): derivatives in the heating and cooling cycle (indicated in red and blue respectively) with hysteresis width  $\Delta T_H = 0.6 \text{ K}$  and transition temperature  $T_{trans} = 59.5 \text{ K}$

As can be seen, the resistivity changes by a factor of  $r_{IM} = 76$  and a total value of  $5.2 \text{ k}\Omega$  while the hysteresis width  $\Delta T_H = 0.6 \text{ K}$  is very small at a transition temperature  $T_{trans} = 59.5 \text{ K}$ . In the XRD scan in fig. 47 one can mainly identify the monoclinic phase of  $VO_2$  and some peaks of monoclinic  $V_6O_{13}$  as well as the metallic (cubic) vanadium peak. Looking at the SEM images of another sample produced at the same settings (see appendix, sample name: VOX92) in fig. 48(a) and a tilted assembly of the target, the formation of nanorods on the surface can be observed. It is of significance to determine whether the rods arise from a columnar structure or grow on the surface of a dense

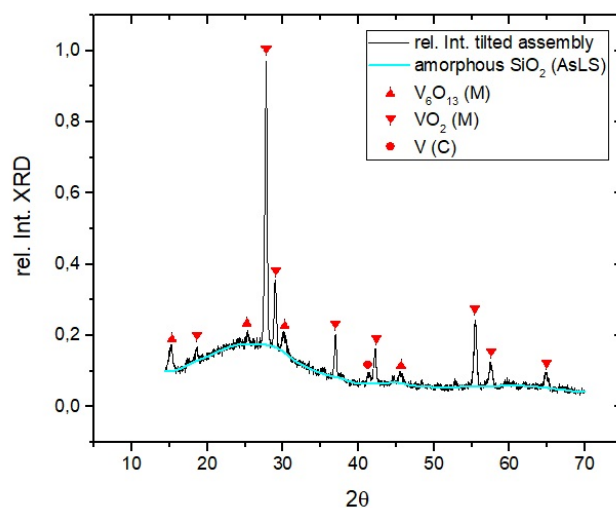
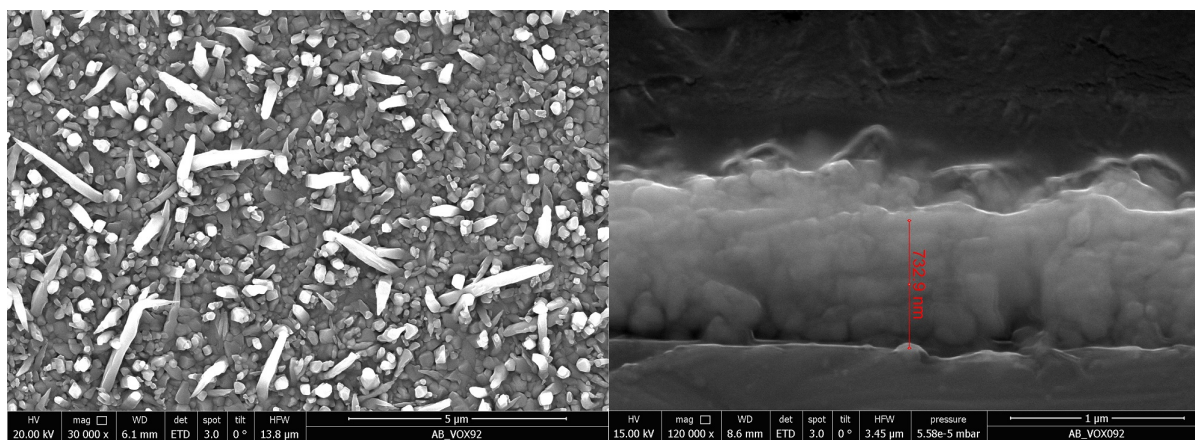


Figure 47: GIXRD scan of “tilted assembly” sample VOX93 at  $\alpha = 5.5^\circ$ , normalized to the maximum intensity and assignment of the identified peaks to  $VO_2(M)$ ,  $V_2O_5$ ,  $V_6O_{13}(M)$  and  $V(C)$  using HighScore Plus; the broad peaks from the amorphous glass substrate were determined by AsLS fitting

recrystallized layer. In order to do so, an additional cross sectional view of film reveals that the nanorods at the surface grow on a film of dense crystallites rather than from a columnar structure, see fig: 48(b).



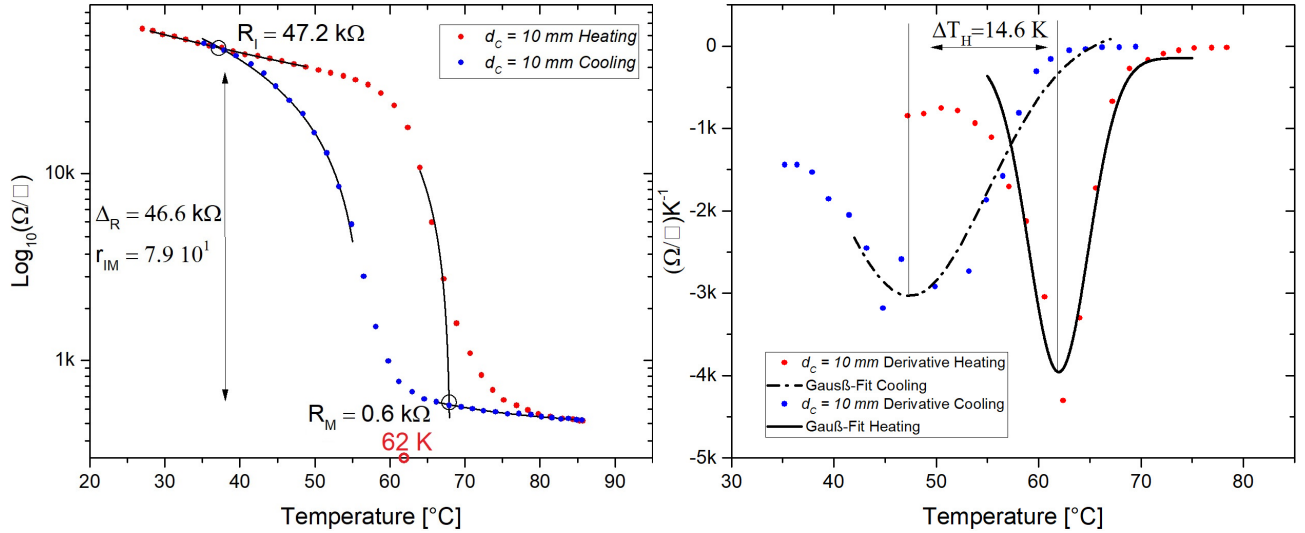
(a) SEM image of sample VOX92

(b) Side-view SEM image of sample VOX92

Figure 48: (a): nano-structured surfaces of “tilted assembly” sample VOX92, showing the growth of rods and needles, up to a length 3  $\mu\text{m}$ ; (b): cross sectional view (vertically cut) shows a dense film formation with an estimated (by SEM) thickness of 733 nm

In the following the influence of systematically reduced  $d_C$  on the thermochromic properties of selected samples will be discussed.

$d_C = 10 \text{ mm}$



(a) Sample VOX103 four-point probe measurement (b) Sample VOX103 derivative of four-point probe measurement

Figure 49: (a) Four-point measurement of a sample produced at  $d_C = 10 \text{ mm}$ , showing a resistivity change of  $r_{IM} = 79$  at total resistivity change of  $\Delta_R = 46.6 \text{ k}\Omega$ ; (b) derivatives in the heating and cooling cycle (indicated in red and blue respectively) yielding a hysteresis width of  $\Delta T_H = 14.6 \text{ K}$  and a transition temperature of  $T_{trans} = 62 \text{ K}$

Sample VOX103, sputtered with a cooling plate diameter of  $d_C = 10 \text{ mm}$  exhibits a decrease in sheet resistivity of  $r_{IM} = 79$  and an absolute change of  $\Delta_R = 46.6 \text{ k}\Omega$  whereas the width of the hysteresis  $\Delta T_H = 14.6 \text{ K}$  becomes significantly broader compared to the tilted assembly sample and the transition temperature rises to  $T_{trans} = 62 \text{ K}$ , as seen in fig. 49. From the XRD scan in fig. 50 it is visible that the signal is strongly underlayed by the amorphous glass substrate. However, monoclinic  $\text{VO}_2$  and anorthic  $\text{V}_6\text{O}_{11}$  can be identified.

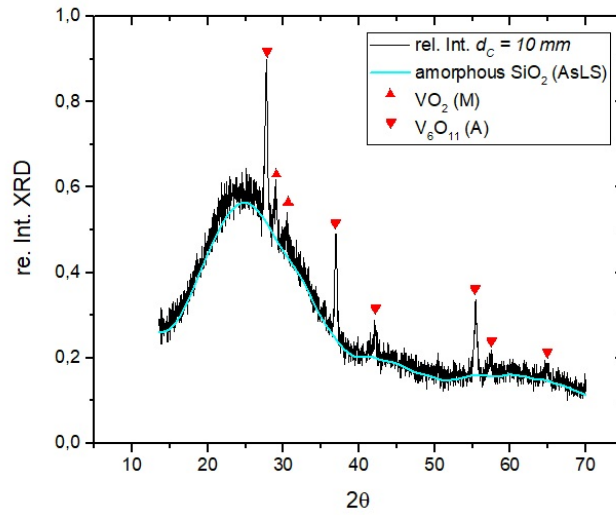
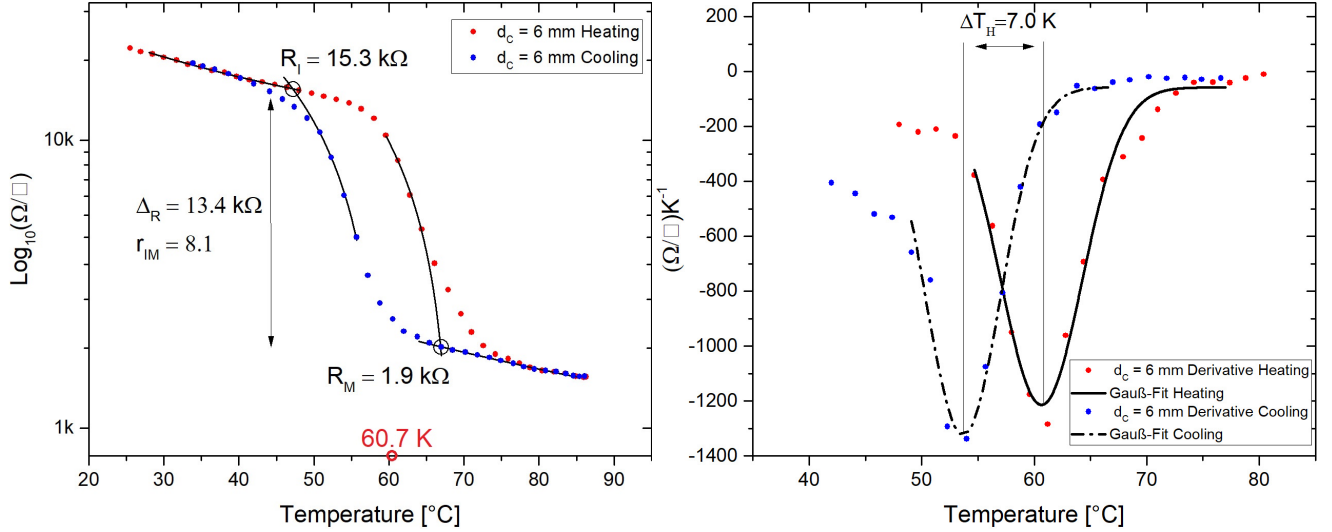


Figure 50: *GIXRD scan at  $\alpha = 5.5^\circ$ , of sample VOX103 produced at  $d_C = 10$  mm, normalized to the maximum intensity and assignment of the identified peaks to  $VO_2(M)$  and  $V_6O_{11}(A)$  using HighScore Plus; the broad peaks from the amorphous glass substrate were determined by AsLS fitting*

$$d_C = 6 \text{ mm}$$



(a) *Sample VOX106 four-point probe measurement* (b) *Sample VOX106 derivative of four-point probe measurement*

Figure 51: (a) *Four-point measurement of sample VOX106 produced at  $d_C = 6 \text{ mm}$ , showing a resistivity change of  $r_{IM} = 8.1$  at total resistivity change of  $\Delta_R = 13.4 \text{ k}\Omega$ ; (b): derivatives in the heating and cooling cycle (indicated in red and blue respectively) with hysteresis width  $\Delta T_H = 7.0 \text{ K}$  and a transition temperature  $T_{trans} = 60.7 \text{ K}$*

By further decreasing the cooling plate diameter to  $d_C = 6 \text{ mm}$  an interesting observation could be made. The resistivity is only lowered by  $r_{IM} = 8.1$  at a total resistivity change of  $\Delta_R = 13.4 \text{ k}\Omega$ , but the hysteresis width becomes clearly smaller  $\Delta T_H = 7 \text{ K}$  at a transition temperature of  $T_{trans} = 60.7 \text{ K}$ . Fig. 51 shows the four-point measurement of this sample. The according XRD scan (see fig. 52) shows a clear monoclinic  $\text{VO}_2$  structure, orthorhombic  $\text{V}_2\text{O}_5$  and like the “tilted assembly” sample, a metallic vanadium peak. A small peak, which may be assigned to  $\text{V}_6\text{O}_{11}$  is marked in grey.

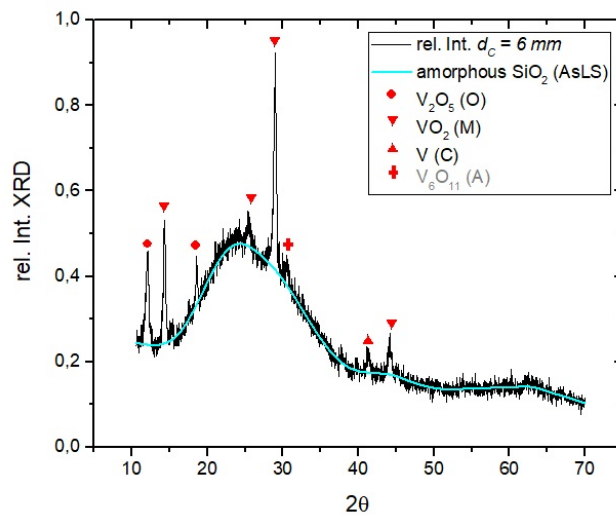
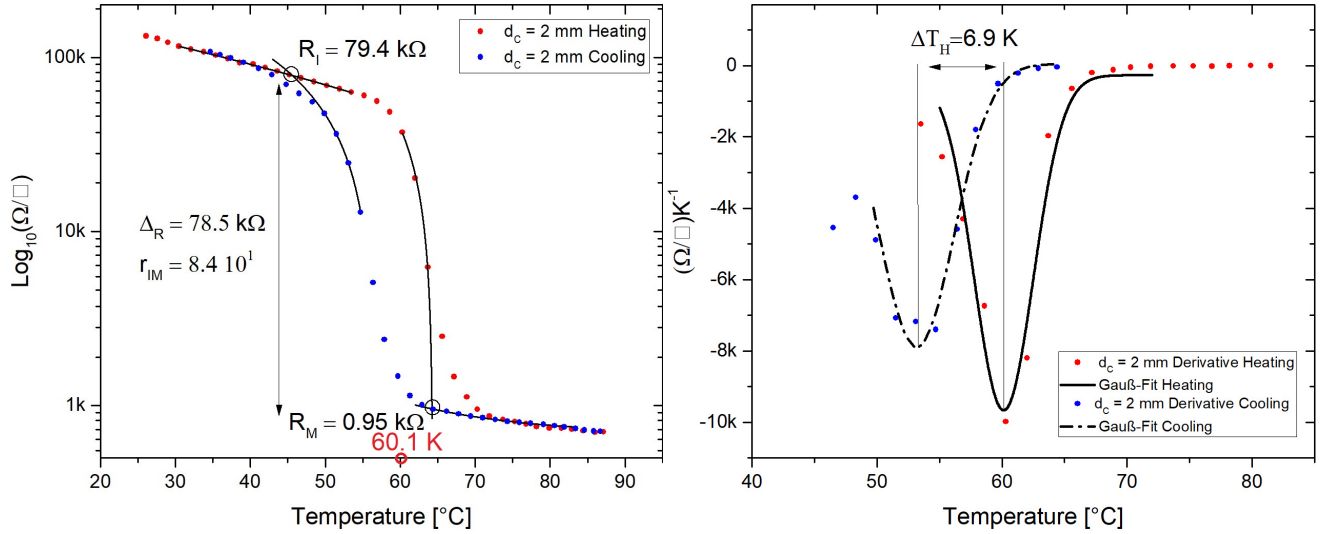


Figure 52: *GIXRD* scan at  $\alpha = 5.5^\circ$ , of sample *VOX106* produced at  $d_C = 6$  mm, normalized to the maximum intensity and assignment of the identified peaks to  $\text{VO}_2(M)$ ,  $\text{V}_2\text{O}_5(O)$ ,  $\text{V}(C)$  ( $\text{V}_6\text{O}_{11}(A)$ ?) using *HighScore Plus*; the broad peaks from the amorphous glass substrate were determined by *AsLS* fitting

$$d_C = 2 \text{ mm}$$



(a) Sample VOX118 four-point probe measurement

(b) Sample VOX118 derivative of four-point probe measurement

Figure 53: (a) Four-point measurement of sample VOX118 produced at  $d_C = 2 \text{ mm}$ , showing a resistivity change of  $r_{IM} = 84$  at total resistivity change of  $\Delta_R = 78.5 \text{ k}\Omega$ ; (b): derivatives in the heating and cooling cycle (indicated in red and blue respectively) with hysteresis width  $\Delta T_H = 6.9 \text{ K}$  and a transition temperature  $T_{trans} = 60.1 \text{ K}$

At a cooling plate diameter of  $d_C = 2 \text{ mm}$  the resistivity change reaches  $r_{IM} = 84$  at a total resistivity change of  $\Delta_R = 78.5 \text{ k}\Omega$ , a hysteresis width of  $\Delta T_H = 6.9 \text{ K}$  and a transition temperature  $T_{trans} = 60.1 \text{ K}$ . In fig. 53 the four-point measurement of sample VOX118 is shown. The analysis of the XRD pattern indicates a composition of monoclinic  $\text{VO}_2$ , a metallic peak of vanadium and anorthic  $\text{V}_6\text{O}_{11}$  as can be seen in fig. 54. The presence of  $\text{V}_6\text{O}_{11}$ , which itself is thermochromic, seems not to have a big influence on the SMT or at least does not diminish it.

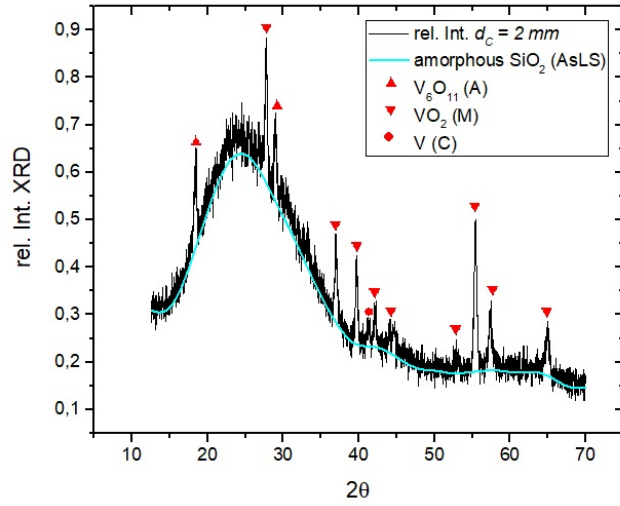
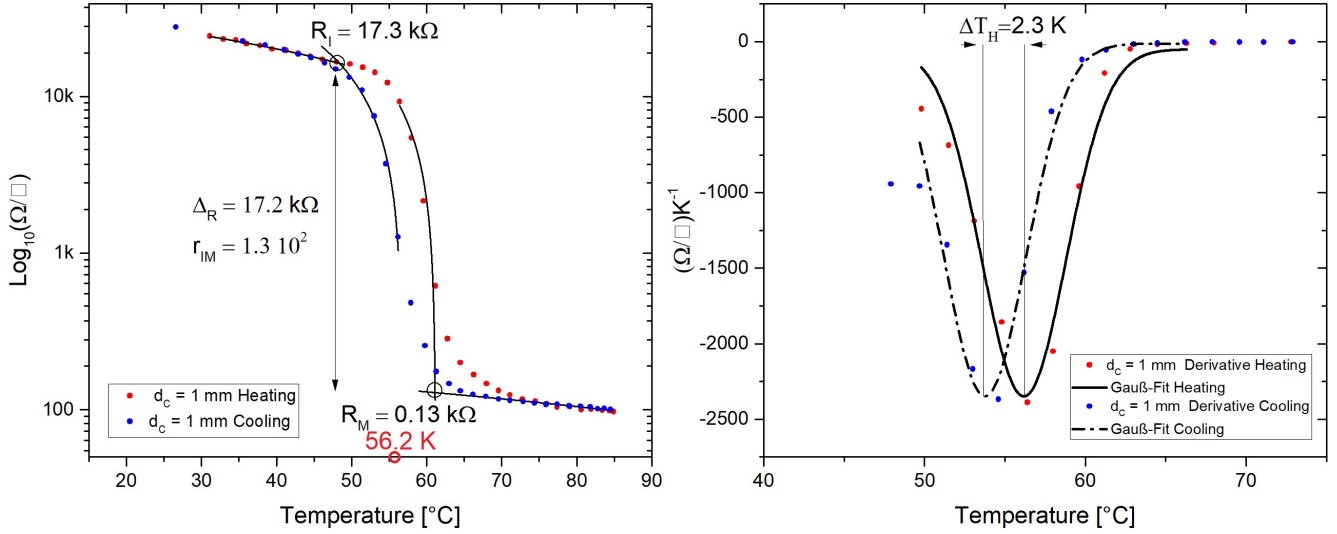


Figure 54: *GIXRD scan at  $\alpha = 5.5^\circ$ , of sample VOX118 produced at  $d_C = 2$  mm, normalized to the maximum intensity and assignment of the identified peaks to  $VO_2(M)$ ,  $V(C)$  and  $V_6O_{11}(A)$  using HighScore Plus; the broad peaks from the amorphous glass substrate were determined by AsLS fitting*

$d_C = 1 \text{ mm}$



(a) Sample VOX135 four-point probe measurement (b) Sample VOX135 derivative of four-point probe measurement

Figure 55: (a) Four-point measurement of sample VOX135 produced at  $d_C = 1 \text{ mm}$ , showing a resistivity change  $r_{IM} = 133$  and total resistivity change of  $\Delta_R = 17.2 \text{ k}\Omega$ ; (b): derivatives in the heating and cooling cycle (indicated in red and blue respectively) yielding a hysteresis width of  $\Delta T_H = 2.3 \text{ K}$  and a transition temperature  $T_{trans} = 56.2 \text{ K}$

Sample VOX135 produced at a cooling plate diameter of  $d_C = 1 \text{ mm}$  yielded a change of the sheet resistivity of  $r_{IM} = 133$  at a total resistivity change of  $\Delta_R = 17.3 \text{ k}\Omega$ , a hysteresis width of  $\Delta T_H = 2.3 \text{ K}$  and a transition temperature  $T_{trans} = 56.2 \text{ K}$ . The according four-point measurement of sample VOX135 is shown in fig. 55. The XRD scan reveals a crystal structure, mainly composed of monoclinic  $VO_2$  and two small peaks of orthorhombic  $V_2O_5$ , as seen in fig. 56. The sample produced at  $d_C = 1 \text{ mm}$  was also analyzed by high temperature XRD at  $90^\circ\text{C}$  to observe the phase change of the crystal, which is shown in fig. 57 in comparison to the XRD scan at room temperature. The peaks (1) and (2) in fig. 57 are slightly shifted above the SMT and were fitted with a Gaussian curve. The peaks were assigned to the respective lattice planes of the monoclinic and tetragonal phase. The peaks at  $48.51^\circ$  and  $52.86^\circ$  in the monoclinic phase vanish above the SMT, which is in accordance with the theoretical prediction. This is mentioned because Zhang et al. [8] assigned the peak shift to internal stresses in the thin films. The influence of internal stresses on the peak positions is not denied here, but the possibility to assign the peaks to the respective lattice planes of the

monoclinic and tetragonal phase and the vanishing of certain peaks indicates that the lattice distortion of the SMT is the main contributor to the peak shift in the XRD pattern.

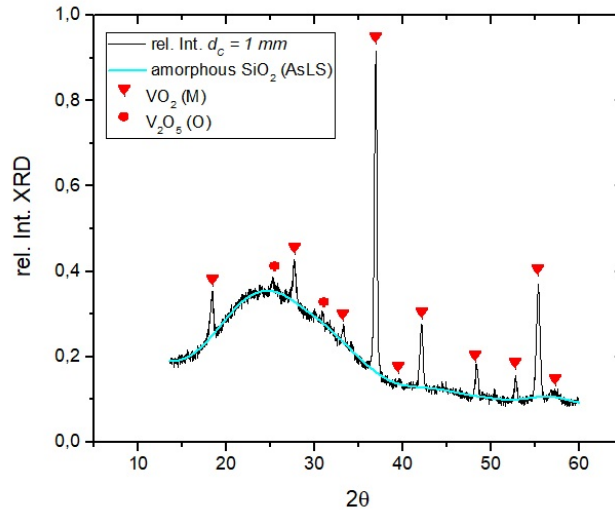


Figure 56: *GIXRD scan at  $\alpha = 5.5^\circ$ , of sample VOX135 produced at  $d_C = 1$  mm, normalized to the maximum intensity and assignment of the identified peaks to  $VO_2(M)$  and  $V_2O_5(O)$  using HighScore Plus; the broad peaks from the amorphous glass substrate were determined by AsLS fitting*

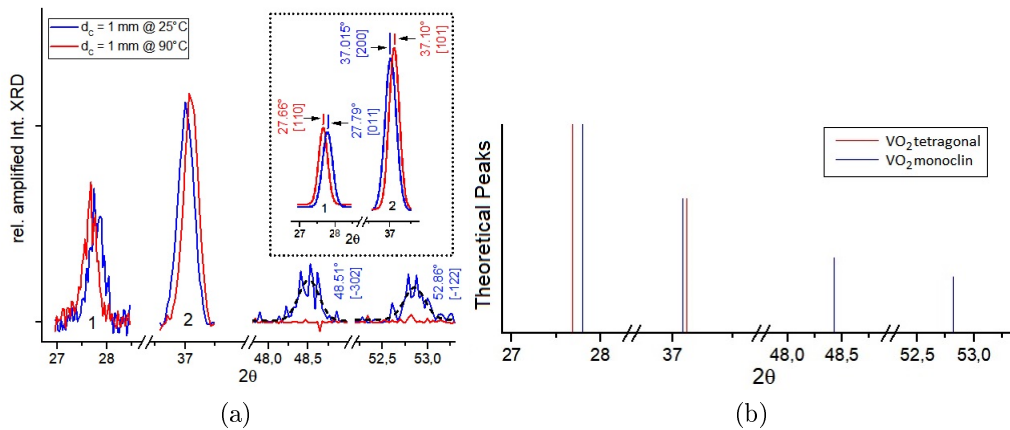


Figure 57: (a): *GIXRD scan at  $\alpha = 5.5^\circ$  of sample VOX135 produced at  $d_C = 1$  mm, at  $25^\circ C$  (blue: monoclinic structure) and  $90^\circ C$  (red: tetragonal structure), peaks are relatively amplified for a better illustration; peak 1 and 2 were fitted with a Gaussian function; the peak shifts were assigned to the lattice planes  $[hkl]$  of the respective crystalline structure; (b): theoretical peaks of the bulk material, adapted from [85, 86]*

$d_C = 0 \text{ mm}$

Finally looking at sample VOX100 from table 8 produced without cooling ( $d_C = 0 \text{ mm}$ ), for which a dark-red glow of the target surface (directly after turning off the plasma) could be observed, the layers became metallic. This demonstrates on one hand the sensitivity of the method of reduced target cooling to slight changes of the cooling plate diameter (below  $d_C = 2 \text{ mm}$ ) and on the other hand the influence of the temperature on the target surface composition.

## 6 Discussion

The samples presented in section 4.1.2 showed the best thermochromic behaviour for the respective cooling plate diameter. In this chapter, the reproducibility for the respective cooling plate diameter and corresponding trends for resistivity change, hysteresis width and transition temperature are discussed. Further, the mass absorption coefficients and Tauc-plots of several samples at different cooling plate diameters, obtained by FTIR, are compared to connect the optical and electrical properties of the films.

The settings in table 8 led to the best thermochromic behaviour for the respective cooling plate diameter and were therefore reproduced. The reproducibility  $R = \frac{n_T^C}{n^C}$  is defined as the ratio of the number of samples showing a thermochromic behaviour  $n_T^C$  to the number of samples produced  $n^C$  at a certain cooling plate diameter. The results for the respective cooling plate diameters are given in table 9.

$d_C$ [mm]	$n^C$	$n_T^C$	$R = \frac{n_T^C}{n^C}$
10	3	3	1
6	3	2	0.67
2	9	6	0.67
1	10	9	0.9

Table 9: *Reproducibility  $R = \frac{n_T^C}{n^C}$  of samples showing a thermochromic behaviour  $n_T^C$  out of  $n^C$  samples in total, at the respective cooling plate diameter  $d_C$*

The quality of the SMT did however still vary, which is mostly attributed to the sensitivity of the system against changes of the oxygen partial pressure. In the following the values  $r_{IM}$ ,  $T_{trans}$  and  $\Delta T_H$  are averaged over three samples, which are marked in blue in the measurement list in appendix B, except for the measurements produced at  $d_C = 6 \text{ mm}$ , where only two samples showed a thermochromic behaviour.

By studying the change of sheet resistivity  $r_{IM}$  as a function of the cooling plate diameter  $d_C$ , one can observe the change of resistivity to increase by half an order of magnitude, except for measurements taken at  $d_C = 6$  mm, as seen in fig. 58.

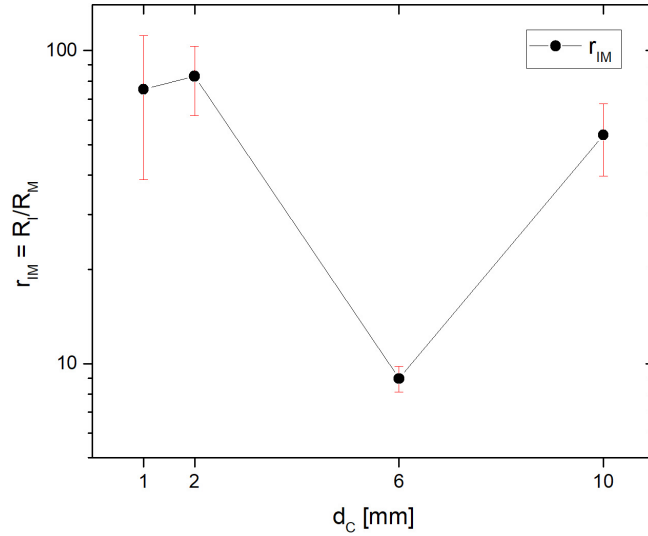


Figure 58: Resistivity change  $r_{IM}$  in dependence of their respective cooling plate diameter  $d_C$ , mean value out of 3 samples (except  $d_C=6$  mm, two samples).

To explain the lower resistivity at  $d_C = 6$  mm, FTIR measurements were performed on all samples with reduced contact area given in table 8. To compare the samples of different thicknesses, the mass absorption coefficient  $\alpha = -\frac{\ln(T)}{d}$  was calculated from the transmission  $T$  and the film thickness  $d$ . The mass absorption coefficients and Tauc-plots for an assumed direct optical bandgap of  $VO_2$  [87] are shown in fig. 59. Qualitatively, the mass absorption at  $d_C = 2$  mm and  $d_C = 10$  mm are similar, while the coefficients for  $d_C = 6$  mm and  $d_C = 1$  mm are clearly lower. They show no clear trend towards smaller cooling plate diameters over all. The linear fits of the corresponding Tauc plots however, are in close proximity to the theoretical value of the electrical bandgap of 0.7 eV [1] except for the sample produced at  $d_C = 6$  mm, which intersects the energy-axis at 0.81 eV. This may indicate bigger inter-atomic distances and internal stresses compared to the other samples. When the SMT takes place, the overlap of the atomic orbitals could then also be smaller leading to less electrical conductivity and a smaller resistivity change  $r_{IM}$ , which is in fact observed. The origin of the different behaviour at  $d_C = 6$  mm remains unclear but may correspond to an undetected issue in the assembly of the cooling plate and therefore different target temperature and gradient at the surface.

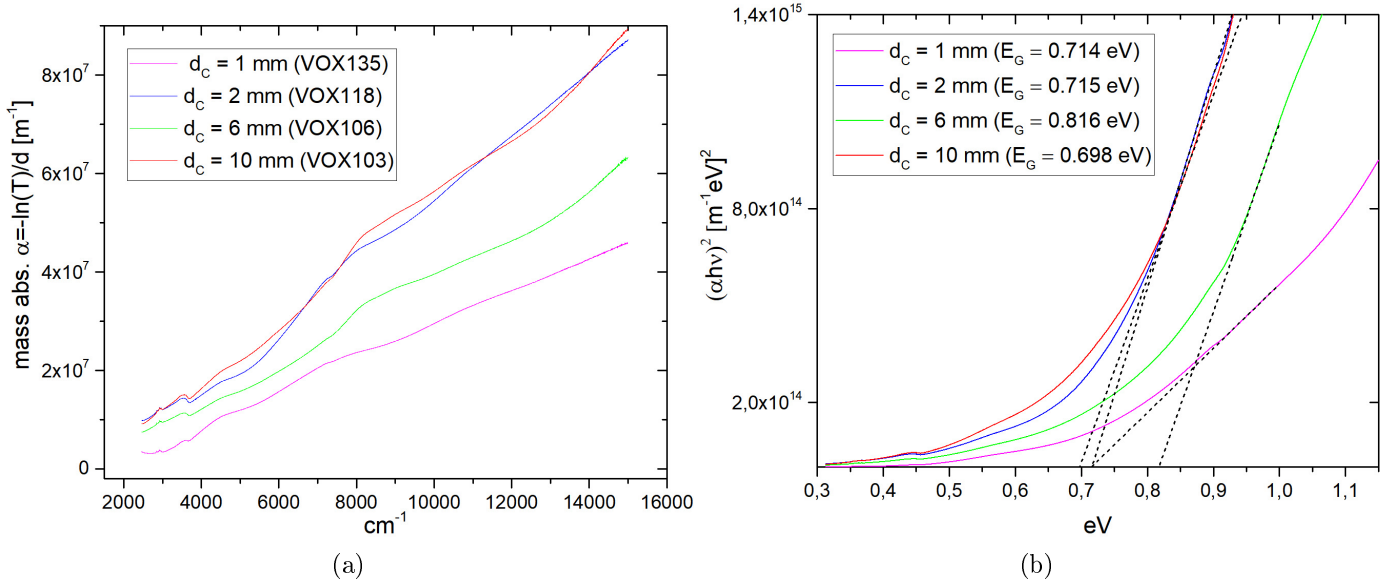


Figure 59: (A): mass absorption coefficient  $\alpha$  obtained by FTIR measurements of the samples listed in table 8, labeled by the respective cooling plate diameter; (B): Corresponding Tauc-plots for indirect optical bandgap calculations; except for the sample produced at  $d_C = 6$  mm (bandgap of 0.82 eV) the optical bandgaps are close to theoretical value of 0.7 eV [1]

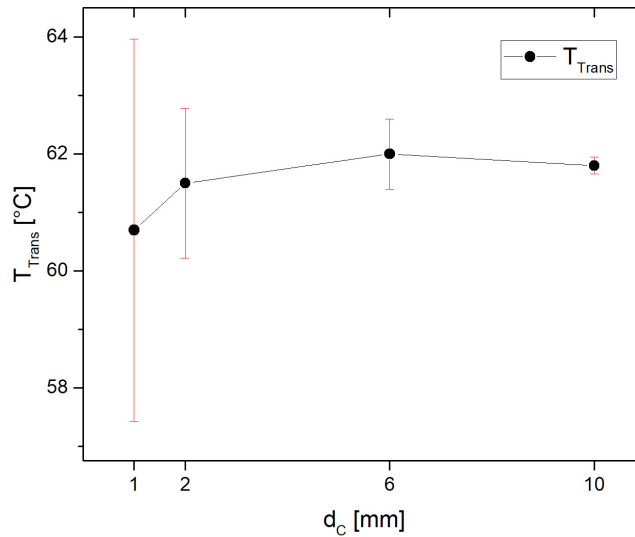


Figure 60: Transition temperature  $T_{Trans}$  (in the heating cycle) in dependence of their respective cooling plate diameter  $d_C$ , mean value out of 3 samples (except  $d_C = 6$  mm, two samples).

To estimate the transition temperature  $T_{Trans}$  of the SMT, the respective saddle points

from the four-point measurements in the heating cycle (from the Gaussian fit of the derivatives) are given in fig. 60. As visible in fig. 60 the mean transition temperature decreases with decreasing contact area while the standard deviation increases in a way, that no clear trend can be confirmed.

However, looking at the hysteresis width a clear trend is observed. The hysteresis width decreases over all with decreasing cooling plate diameter as shown in figure 61.

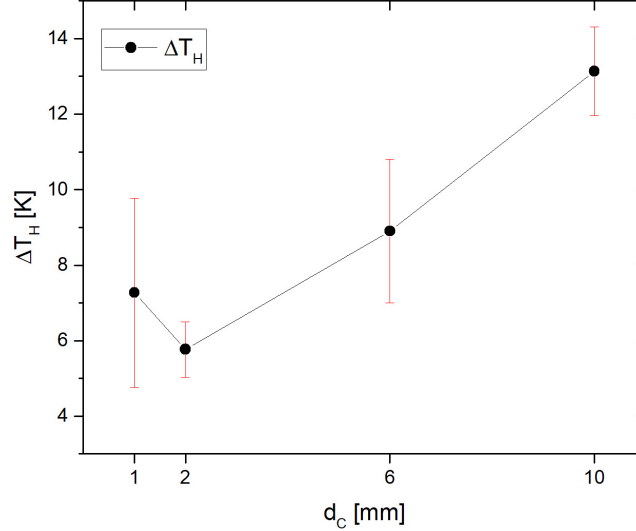


Figure 61: *Hysteresis width  $\Delta T_H$  in dependence of their respective cooling plate diameter  $d_C$ , mean value out of 3 samples (except  $d_C=6$  mm, two samples).*

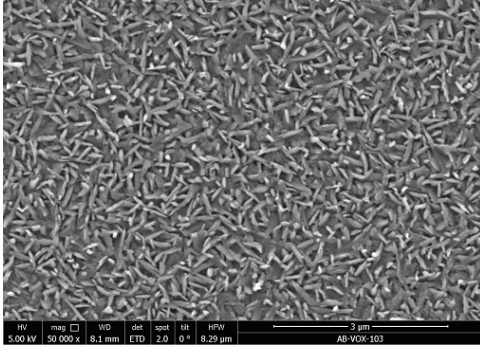
Table 10 shows the calculated grain size for the samples with variable  $d_C$  and tilted assembly in table 8 calculated by the Scherrer method, which is described in section 2.7 The Scherrer constant  $K_S$  for spherical packing  $K_S = \frac{4}{3} \left(\frac{\pi}{6}\right)^{\frac{1}{3}}$  was used. The similar values for the mean grain size of all five samples indicate, that grain boundary effects do not contribute to the decreasing hysteresis width, resistivity change and transition temperature.

$d_C$ [mm]	grain size [nm]
tilted assembly	$34 \pm 6.6$
10	$33.8 \pm 7.5$
6	$30.6 \pm 6.1$
2	$47.9 \pm 4.5$
1	$32.7 \pm 8.6$

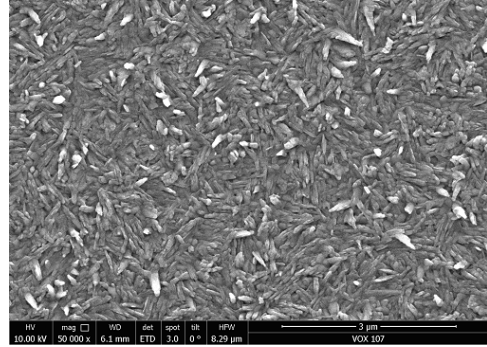
Table 10: *Scherrer calculation of grain size of of the samples from table 8 in dependence of cooling plate diameter  $d_C$*

The width of the hysteresis of the “tilted assembly” sample with  $\Delta T_H = 0.6 K$  could not be achieved using cooling plates, even though the cooling plate with  $d_C = 1$  mm resulted in thin films (VOX135) with a best value of  $\Delta T_H = 2.3 K$ . This indicates that not only the contact area between cooling system and target is decisive for the properties and composition of the layers, but also the spot at which the cooling plate contacts the target and thus the target temperature gradient across the surface. It follows, that the temperature gradient along the target may be a parameter of this method itself.

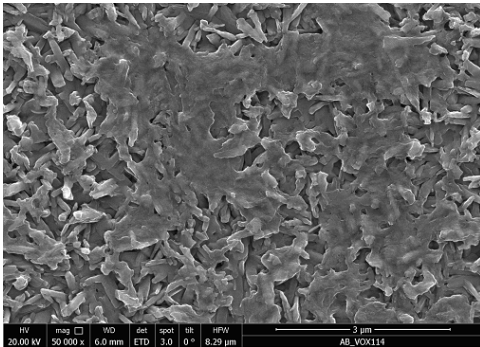
The surface structures observed by SEM of thin films produced at different  $d_C$  are given in fig. 62 and compared to a sample produced at fully cooled target. The sample names from the measurement list in appendix B are given in the figure description.



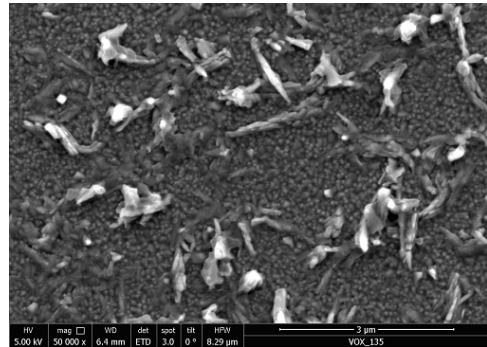
(a) SEM image of sample VOX103 at  $d_C = 10$  mm



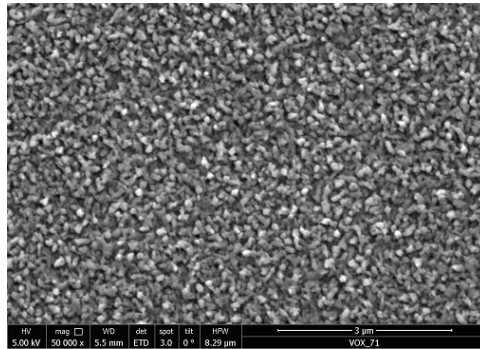
(b) SEM image of sample VOX107 at  $d_C = 6$  mm



(c) SEM image of sample VOX114 at  $d_C = 2$  mm



(d) SEM image of sample VOX135 at  $d_C = 1$  mm



(e) SEM image of sample VOX71 at full target cooling

Figure 62: SEM images of the (a) sample VOX103 at  $d_C = 10$  mm; (b) sample VOX107 at  $d_C = 6$  mm; (c) sample VOX114 at  $d_C = 2$  mm; (d) sample VOX135 at  $d_C = 1$  mm; (e) sample VOX71 at full target cooling; while the surface of the sample at  $d_C = 10$  mm is covered in nanorods of 300-500 nm, the rods begin to merge to platelets in the samples produced at  $d_C = 6$  mm and  $d_C = 2$  mm, while the surface becomes granular with randomly oriented and elongated islands growing on top, for the sample produced at  $d_C = 1$  mm; similar to sample VOX135 the surface structure of sample VOX71, produced at fully cooled target is granular.

The surface structure shows a clear trend with decreasing cooling plate diameter. The surface at  $d_C = 10$  mm consists of rods of about 300 to 500 nm length with a random orientation. These rods are still visible at  $d_C = 6$  mm but start to merge and form clusters and interlinked platelets. The length of the rods was estimated by the SEM images to be 400 to 700 nm. The surface structure at  $d_C = 2$  mm is similar to  $d_C = 6$  mm with random oriented, acicular rods of 600 to 1000 nm length emerging from a flat structure. The surface structure of the films produced at  $d_C = 1$  mm clearly differs from the ones at broader cooling plates. The surface no longer shows a rod-like but a dense granular structure. The grains were estimated to be 70 to 100 nm and their characteristic shape consists of disjointed crystallites of random orientation. This morphology is similar to the one of the sample produced with a tilted target, see fig. 48.

## 7 Conclusion and Outlook

Within this work it could be show that the production of thermochromic films containing  $VO_2$  with DC magnetron sputtering cannot be stabilized at full target cooling. Only after increasing the target temperature good quality films with thermochromic behaviour were produced. In comparison, the reduced target cooling measurements show a clear stabilization of the monoclinic  $VO_2$  phase, even though other oxide phases were still detected in the XRD patterns. Almost pure  $VO_2$  films could be produced at  $d_C = 1$  mm. The resistivity change, hysteresis width and transition temperature show an over all decreasing trend for decreasing the cooling plate diameters even though different samples produced at the same cooling plate diameter still exhibit partially strong variations in the thermochromic behaviour of the thin films. The calculations, simulations and measurements of the target temperature in chapter three all agreed in the indirect proportion between the target temperature and the cooling plate diameter  $T_T \propto (d_C)^{-\kappa}$ .

However, the temperature measurements of the target surface did not allow a quantitative temperature determination but qualitative analysis only. The indirect and direct measurements of the target temperature either did not work or contained undetermined parameters. Further temperature measurements should be done optically using an infrared sensor.

As a case of minimum thermal contact, the “tilted assembly” measurements demonstrate the possibilities of the cooling plate position and shape on the produced films. The

SMT in the tilted assembly measurements showed a hysteresis width of 0.6 K which even for the samples produced at  $d_C = 1$  mm with a best value of  $\Delta T_H = 2.3$  K could not be achieved, giving rise to the assumption that a temperature gradient across the target plays also an important role. This is underlined by the observations of structural gradients of some layers produced with reduced target cooling. The gradient seemed to follow the shape of the plasma ring on the target surface. The thermochromic behaviour also changed across the surface in that case. Experiments with different forms and positions of the cooling plates should be performed to further investigate the compositional and structural inhomogeneities of the layers.

A major drawback of the measurements was, that the oxygen partial pressure could not be varied in a broad range without losing the thermochromic behaviour of the thin films, in accordance with J. Theil et al. [51]. Although the reduced target cooling mainly facilitated the production and reproducibility of thin films with thermochromic behaviour, the oxygen partial pressure was still a limiting factor. It is suggested to change the position of the oxygen inlet and the direction of the oxygen flow between target and substrate in further experiments. As stated by Shu-Yi Li et al. [53], the structure of the thin films can be significantly changed by this manipulation, because it allows to alter the amount of oxygen consumed by the substrate and the target. Subsequently, the reproducibility may also be enhanced in this process and the oxygen partial pressure can be stabilized.

The main issue with the current cooling plate design seems to be the limitation in terms of further decreasing the diameter  $d_C$ . As the central cooling plate was difficult to cut below 1 mm, it is suggested to change the design for smaller contact areas.

The effects of substrate temperatures, different than 370 °C to 400 °C during the reduced target cooling experiments have not been investigated in this work. It would be of great interest for thin oxide films on temperature-sensitive materials like organic or synthetic polymers to produce as deposited thin oxide films in a controlled manner at substrate temperatures  $< 200$  °C.

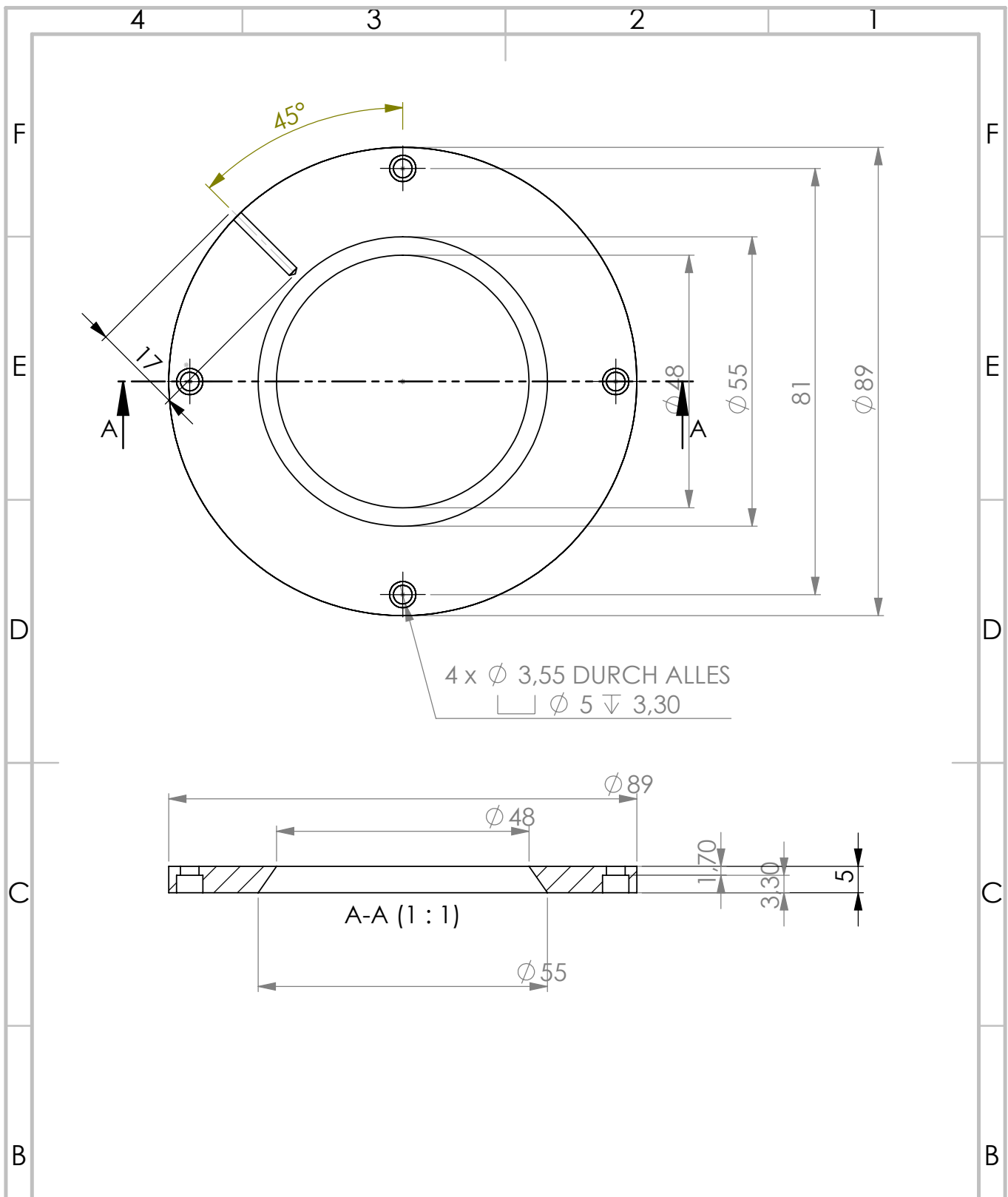
The behaviour of the reactive sputter hysteresis at different power or current levels, especially in the transition region in dependence of the cooling plate diameter would also be worthwhile to be studied in further experiments. This would give an indirect insight into the influence of target heating on the poisoning of the surface area and compound formation for instance by making according adjustments to the Berg model. It is suggested to exchange the sputter yields of the metals and the oxides in the Berg model by a temperature dependent function  $Y(T)$  and let the target heat up before

the hysteresis loop is measured to work in state conditions as done in [88]

Finally, the doping of the oxide layers by other metals like tungsten in a reactive co-sputtering process to further lower the transition point towards room temperature may form the most complex but interesting experiment to be combined with the method of reduced target cooling. Before performing these measurements one must understand and control the hysteresis behaviour of a two-target reactive system. Then the individual effects of target heating on both target materials must be investigated and the necessary sputter powers for doping have to be determined.

This work could clearly demonstrate, that variable target temperature improves the production of thermochromic vanadium dioxide thin films. The quality of the SMT over all increased with higher target temperatures, so did the reproducibility. Therefore, the method of reduced target cooling, which is currently not represented strongly in research, opens up promising possibilities for the production of thermochromic thin films by reactive DC magnetron sputtering.

## 8 Design Drawings



4 x  $\varnothing$  3,55 DURCH ALLES  
 $\square$   $\varnothing$  5  $\nabla$  3,30

A-A (1 : 1)

WENN NICHT ANDERS DEFINIERT:  
 BEMASSUNGEN SIND IN MILLIMETER  
 OBERFLÄCHENBESCHAFFENHEIT:  
 TOLERANZEN:  
 LINEAR:  
 WINKEL:

OBERFLÄCHENGÜTE:

ENTGRATEN  
 UND SCHARFE  
 KANTEN  
 BRECHEN

ZEICHNUNG NICHT SKALIEREN

ÄNDERUNG

NAME	SIGNATUR	DATUM
GEZEICHNET Anatol Beck		10.4.2018
GEPRÜFT		
GENEHMIGT		
PRODUKTION		
QUALITÄT		
WERKSTOFF: Edelstahl		
GEWICHT: 20,30 g		

BENENNUNG: <b>Überwurf-Ring</b>
ZEICHNUNGSNR.
MASSTAB: 1:1
BLATT 1 VON 1

A4

## References

- [1] F. J. Morin. Oxides which show a metal-to-insulator transition at the neel temperature. *Physical Review Letters*, 3(1):34–36, Jan 1959.
- [2] I.g. Madida, A. Simo, B. Sone, A. Maity, J.b. Kana Kana, A. Gibaud, G. Merad, F.t. Thema, and M. Maaza. Submicronic VO<sub>2</sub>-pvp composites coatings for smart windows applications and solar heat management. *Solar Energy*, 107:758–769, 2014.
- [3] Sihai Chen, Hong Ma, Xinjian Yi, Tao Xiong, Hongcheng Wang, and Caijun Ke. Smart VO<sub>2</sub> thin film for protection of sensitive infrared detectors from strong laser radiation. *Sensors and Actuators A: Physical*, 115(1):28–31, 2004.
- [4] Changhong Chen, Xinjian Yi, Xingrong Zhao, and Bifeng Xiong. Characterizations of VO<sub>2</sub>-based uncooled microbolometer linear array. *Sensors and Actuators A: Physical*, 90(3):212–214, 2001.
- [5] Evgheni Strelcov, Yigal Lilach, and Andrei Kolmakov. Gas sensor based on metal-insulator transition in VO<sub>2</sub> nanowire thermistor. *Nano Letters*, 9(6):2322–2326, Oct 2009.
- [6] M. Rini, Z. Hao, R. W. Schoenlein, C. Giannetti, F. Parmigiani, S. Fourmaux, J. C. Kieffer, A. Fujimori, M. Onoda, S. Wall, and et al. Optical switching in VO<sub>2</sub> films by below-gap excitation. *Applied Physics Letters*, 92(18):181904, May 2008.
- [7] Lele Fan, Yuliang Chen, Qianghu Liu, Shi Chen, Lei Zhu, Qiangqiang Meng, Baolin Wang, Qinfang Zhang, Hui Ren, Chongwen Zou, and et al. Infrared response and optoelectronic memory device fabrication based on epitaxial VO<sub>2</sub> film. *ACS Applied Materials & Interfaces*, 8(48):32971–32977, 2016.
- [8] Dong-Ping Zhang, Mao-Dong Zhu, Yi Liu, Kai Yang, Guang-Xing Liang, Zhuang-Hao Zheng, Xing-Min Cai, and Ping Fan. High performance VO<sub>2</sub> thin films growth by DC magnetron sputtering at low temperature for smart energy efficient window application. *Journal of Alloys and Compounds*, 659:198–202, 2016.
- [9] Luo Zhen-Fei, Wu Zhi-Ming, Xu Xiang-Dong, Wang Tao, and Jiang Ya-Dong. Study of nanocrystalline VO<sub>2</sub> thin films prepared by magnetron sputtering and post-oxidation. *Chinese Physics B*, 19(10):106103, 2010.

- [10] S. Chen, J.Lai, H. Ma, H. Wang, and X. Yi. Characterization of nanostructured VO<sub>2</sub> thin films grown by magnetron controlled sputtering deposition and post annealing method. *Optics Express*, 17(26), 2009.
- [11] V. Melnik, I. Khatsevych, V. Kladko, A. Kuchuk, V. Nikirin, and B. Romanyuk. Low-temperature method for thermochromic high ordered VO<sub>2</sub> phase formation. *Materials Letters*, 68:215–217, 2012.
- [12] R. Behrisch and W. Eckstein. Sputtering yield increase with target temperature for Ag. *Nuclear Instruments and Methods in Physics Research Section B: Beam Interactions with Materials and Atoms*, 82(2):255–258, 1993.
- [13] A. Billard, D. Mercks, F. Perry, and C. Frantz. Influence of the target temperature on a reactive sputtering process. *Surface and Coatings Technology*, 116-119:721–726, 1999.
- [14] R.A. Häfer. *Oberfl{ä}chen- und Dünnschicht- Technologie, Teil 1: Beschichtungen von Oberflächen*. Springer Verlag, , Berlin, 1987.
- [15] J Reece Roth. *Industrial Plasma Engineering: Volume 1: Principles*. CRC Press, 1995.
- [16] J.Roth, J.Rahel, Xin Dai, and D. Sherman. The physics and phenomenology of one atmosphere uniform glow discharge plasma (*oaugd<sup>TM</sup>*) reactors for surface treatment applications. *Journal of Physics D: Applied Physics*, 38(4):555, 2005.
- [17] J. M. Walls, editor. *Methods of Surface Analysis: Techniques and Applications*. Cambridge University Press, 1989.
- [18] R.Smith, M. Jakas, D. Ashworth, B. Oven, M. Bowyer, I. Chakarov, and R. Webb. *Atomic and Ion Collisions in Solids and at Surfaces: Theory, Simulation and Applications*. Cambridge University Press, 2005.
- [19] S. Berg, H-O. Blom, T. Larsson, and C. Nender. Modeling of reactive sputtering of compound materials. *Journal of Vacuum Science & Technology*, 5(2):202–207, 1987.
- [20] S. Berg and T. Nyberg. Fundamental understanding and modeling of reactive sputtering processes. *Thin Solid Films*, 476(2):215–230, 2005.

- [21] Ted A O'Brien, Katrin Albert, and Michael C. Zerner. The electronic structure and spectroscopy of V<sub>2</sub>. *The Journal of Chemical Physics*, 112(7):3192–3200, 2000.
- [22] A.a. Akande, E.c. Linganiso, B.p. Dhonge, K.e. Rammutla, A. Machatine, L. Prinsloo, H. Kunert, and B.w. Mwakikunga. Phase evolution of vanadium oxides obtained through temperature programmed calcinations of ammonium vanadate in hydrogen atmosphere and their humidity sensing properties. *Materials Chemistry and Physics*, 151:206–214, 2015.
- [23] A. L. Pergament, G. B. Stefanovich, N. A. Kuldin, and A. A. Velichko. On the problem of metal-insulator transitions in vanadium oxides. *ISRN Condensed Matter Physics*, 2013:1–6, 2013.
- [24] Zheng Yang, Changhyun Ko, and Shriram Ramanathan. Oxide electronics utilizing ultrafast metal-insulator transitions. *Annual Review of Materials Research*, 41(1):337–367, Apr 2011.
- [25] Chiranjivi Lamsal and N. M. Ravindra. Optical properties of vanadium oxides- an analysis. *Journal of Materials Science*, 48(18):6341–6351, 2013.
- [26] L. Baldassarre, A. Perucchi, E. Arcangeletti, D. Nicoletti, D. Di Castro, P. Postorino, V. A. Sidorov, and S. Lupi. Electrodynamics near the metal-to-insulator transition in V<sub>3</sub>O<sub>5</sub>. *Physical Review B*, 75(24), Dec 2007.
- [27] F.a. Chudnovskii, E.i. Terukov, and D.i. Khomskii. Insulator-metal transition in V<sub>3</sub>O<sub>5</sub>. *Solid State Communications*, 25(8):573–577, 1978.
- [28] S. Asbrink, M. Wolcyrz, and S.H. Hong. X-ray bond-type diffractometer investigations on V<sub>3</sub>O<sub>5</sub> in the temperature interval 298 to 480 K including the phase transition temperature  $t_t = 428$  K. *Physica Status Solidi A - Applications and Materials*, 87:135–140, 1985.
- [29] S.H. Hong and S. Asbrink. The structure of the high-temperature modification of V<sub>3</sub>O<sub>5</sub> at 458 K. *Acta Crystallographica B (24,1968-38,1982)*, 38:713–719, 1982.
- [30] H. Horiuchi, N. Morimoto, and M. Tokonami. Crystal structures of V<sub>n</sub>O<sub>2n-1</sub> ( $2 < n < 7$ ). *Journal of Solid State Chemistry*, 17:407–424, 1976.
- [31] J.L. Hodeau and M. Marezio. The crystal structure of V<sub>4</sub>O<sub>7</sub> at 120K. *Journal of Solid State Chemistry*, 23:253–263, 1978.

- [32] H. Horiuchi, M. Tokonami, N. Morimoto, and K. Nagasawa. The crystal structure of V4 O7. *Acta Crystallographica B (24,1968-38,1982)*, 28:1404–1410, 1972.
- [33] M. Marezio, D.B. McWhan, P.D. Dernier, and J.P. Remeika. Structural aspects of the metal-insulator transition in V4 O7. *Journal of Solid State Chemistry*, 6:419–429, 1973.
- [34] M. Marezio, P.D. Dernier, D.B. McWhan, and S. Kachi. Structural aspects of the metal-insulator transition in V5 O9. *Journal of Solid State Chemistry*, 11:301–313, 1974.
- [35] Y. le Page, P. Bordet, and M. Marezio. Valence ordering in V5 O9 below 120K. *Journal of Solid State Chemistry*, 92:380–385, 1991.
- [36] V6O11 (orthorhombic, cmcm, 63). <https://materialsproject.org/materials/mp-849537/>. Last Accessed on 18.9. 2018.
- [37] J.M. Allred and R.J. Cava. Crystal structures of the high temperature forms of V8 O15 and V9 O17 and structural trends in the VnO2n-1 magneli series. *Journal of Solid State Chemistry*, 198:10–17, 2013.
- [38] H. Katzke and R. Schloegl. General structural relationships between rutile-type V O2 and the Magneli-phases Vn O2n-1. *Zeitschrift fuer Kristallographie (1979-2010)*, 218:432–439, 2003.
- [39] Manil Kang, Inkoo Kim, Sok Won Kim, Ji-Wook Ryu, and Hyo Yeol Park. Metal-insulator transition without structural phase transition in V2O5 film. *Applied Physics Letters*, 98(13):131907, 2011.
- [40] John B. Goodenough. The two components of the crystallographic transition in VO2. *Journal of Solid State Chemistry*, 3(4):490–500, 1971.
- [41] Changzheng Wu, Feng Feng, and Yi Xie. Design of vanadium oxide structures with controllable electrical properties for energy applications. *Chemical Society Reviews*, 42(12), 2013.
- [42] N. F. Mott. The transition to the metallic state. *Philosophical Magazine*, 6(62):287–309, 1961.

- [43] R. Peierls. *More Surprises in Theoretical Physics (Princeton Series in Physics)*. Princeton University Press, 1991.
- [44] P. W. Anderson. Absence of diffusion in certain random lattices. *Physical Review*, 109(5):1492–1505, Jan 1958.
- [45] J. Hubbard. Electron correlations in narrow energy bands. *Proceedings of the Royal Society A: Mathematical, Physical and Engineering Sciences*, 276(1365):238–257, 1963.
- [46] T Holstein. Studies of polaron motion. *Annals of Physics*, 8(3):325–342, 1959.
- [47] Holger Fehske and Georg Hager et al. *Metal-to-Nonmetal Transitions (Springer Series in Materials Science)*. Springer, 2010.
- [48] Janos K. Asboth, Laszlo Oroszlany, and Andras Palyi. *A Short Course on Topological Insulators: Band Structure and Edge States in One and Two Dimensions (Lecture Notes in Physics)*. Springer, 2016.
- [49] Matthias Bartelmann, Björn Feuerbacher, Timm Krüger, Dieter Lüst, Anton Rebhan, and Andreas Wipf. *Theoretische Physik (German Edition)*. Springer Spektrum, 2015.
- [50] John D. Budai, Jiawang Hong, Michael E. Manley, Eliot D. Specht, Chen W. Li, Jonathan Z. Tischler, Douglas L. Abernathy, Ayman H. Said, Bogdan M. Leu, Lynn A. Boatner, and et al. Metallization of vanadium dioxide driven by large phonon entropy. *Nature*, 515(7528):535–539, 2014.
- [51] J. Theil. Reactive magnetron sputtering of VO<sub>2</sub> thin films. Master’s thesis, University of Illinois at Urbana-Champaign, 1988.
- [52] M. Zeiner. Konstruktion eines Substrathalters für bias - Sputtern, Analyse der Auswirkungen auf die Schichtbildung von Vanadiumdioxid und Untersuchung der Heizkurve des Substrats im Vakuum. 2018.
- [53] Shu-Yi Li, Kyoko Namura, Motofumi Suzuki, Gunnar A. Niklasson, and Claes G. Granqvist. Thermochromic VO<sub>2</sub> nanorods made by sputter deposition: Growth conditions and optical modeling. *Journal of Applied Physics*, 114(3), 2013.

- [54] Hadis Bashiri. Desorption kinetics at the solid/solution interface: A theoretical description by statistical rate theory for close-to-equilibrium systems. *The Journal of Physical Chemistry C*, 115(13):5732–5739, Oct 2011.
- [55] H.j. Kreuzer and S.h. Payne. Chapter 3. theories of the adsorption-desorption kinetics on homogeneous surfaces. *Studies in Surface Science and Catalysis Equilibria and Dynamics of Gas Adsorption on Heterogeneous Solid Surfaces*, pages 153–200, 1997.
- [56] K. Oura, M. Katayama, A. V. Zotov, V. G. Lifshits, and A. A. Saranin. *Surface Science: An Introduction*. Advanced Texts in Physics. Springer-Verlag Berlin Heidelberg, 1 edition, 2003.
- [57] Diederik Depla and Stijn Mahieu. *Reactive Sputter Deposition*. Springer-Verlag Berlin Heidelberg, 2008.
- [58] John A. Thornton. Influence of apparatus geometry and deposition conditions on the structure and topography of thick sputtered coatings. *Journal of Vacuum Science and Technology*, 11(4):666–670, 1974.
- [59] J A Thornton. High rate thick film growth. *Annual Review of Materials Science*, 7(1):239–260, 1977.
- [60] E.h. Sondheimer. The mean free path of electrons in metals. *Advances in Physics*, 1(1):1–42, 1952.
- [61] K. Fuchs and N. F. Mott. The conductivity of thin metallic films according to the electron theory of metals. *Mathematical Proceedings of the Cambridge Philosophical Society*, 34(01):100, 1938.
- [62] J.J. Thomson. On the theory of electric conduction through thin metallic films. *Proc. Camb. Phil. Soc.*, 11:120, 1901.
- [63] Milton Ohring. *The materials science of thin films*, chapter 10. Academic Press, 1993.
- [64] A. F. Mayadas and M. Shatzkes. Electrical-resistivity model for polycrystalline films: the case of arbitrary reflection at external surfaces. *Physical Review B*, 1(4):1382–1389, 1970.

- [65] Milton Ohring. *The materials science of thin films*. Academic Press, 1993.
- [66] Arthur Uhlir. The potentials of infinite systems of sources and numerical solutions of problems in semiconductor engineering. *Bell System Technical Journal*, 34(1):105–128, 1955.
- [67] Mario Birkholz, Paul F. Fewster, and Christoph Genzel. *Thin film analysis by X-ray scattering*, chapter 1-2. Wiley-VCH, 2009.
- [68] W. L. Bragg. The diffraction of short electromagnetic waves by a crystal. *Scientia*, 23(45):153, 1929.
- [69] Mario Birkholz, Paul F. Fewster, and Christoph Genzel. *Thin film analysis by X-ray scattering*, chapter 3. Wiley-VCH, 2009.
- [70] Paul H C Eilers and Hans F M Boelens. Baseline correction with asymmetric least squares smoothing. 2005.
- [71] D. Stokes. *Principles and Practice of Variable Pressure / Environmental Scanning Electron Microscopy (VP-ESEM)*, chapter 2. Wiley, 2008.
- [72] Peter R. Griffiths and James A. De Haseth. *Fourier Transform Infrared Spectrometry*, chapter 2. Wiley-Interscience, 2007.
- [73] Thermo Scientific. Advantages of a fourier transform infrared spectrometer. Last Accessed on 18.9. 2018.
- [74] Peter R. Griffiths and James A. De Haseth. *Fourier Transform Infrared Spectrometry*. Wiley-Interscience, 2007.
- [75] Nicola Sangiorgi, Lucrezia Aversa, Roberta Tatti, Roberto Verucchi, and Alessandra Sanson. Spectrophotometric method for optical band gap and electronic transitions determination of semiconductor materials. *Optical Materials*, 64:18–25, 2017.
- [76] Zihui Liang, Li Zhao, Wanfan Meng, Cheng Zhong, Shoubin Wei, Binghai Dong, Zuxun Xu, Li Wan, and Shimin Wang. Tungsten-doped vanadium dioxide thin films as smart windows with self-cleaning and energy-saving functions. *Journal of Alloys and Compounds*, 694:124–131, 2017.
- [77] J.H. Lienhard IV and J.H. Lienhard V. *A Heat Transfer Textbook*. Phlogiston Press, Cambridge, MA, 4th edition, 2018. Version 2.12.

- [78] Charles David Hodgman and Robert C. Weast. *Handbook of chemistry and physics a ready-reference book of chemical and physical data*. Chemical Rubber Publ. Co., 1962.
- [79] G. G. Gubareff. *Thermal Radiation Properties Survey: a review of the literature*. Honeywell Research Center, 1960.
- [80] S. X. Cheng, P. Cebe, L. M. Hanssen, D. M. Riffe, and A. J. Sievers. Hemispherical emissivity of V, Nb, Ta, Mo, and W from 300 to 1000 K. *Journal of the Optical Society of America B*, 4(3):351, Jan 1987.
- [81] <http://www.goodfellow.com/E/Copper.html>. Last Accessed on 18.9. 2018.
- [82] C. R. Roger, S. H. Yen, and K. G. Ramanathan. Temperature variation of total hemispherical emissivity of stainless steel AISI 304. *Journal of the Optical Society of America*, 69(10):1384, Jan 1979.
- [83] S. Velasco and F. L. Roman. Determining the curie temperature of iron and nickel. *The Physics Teacher*, 45(6):387–389, 2007.
- [84] [https://www.lesker.com/newweb/deposition\\_materials/depositionmaterials\\_sputtertargets\\_1.cfm?pgid=van1](https://www.lesker.com/newweb/deposition_materials/depositionmaterials_sputtertargets_1.cfm?pgid=van1). Last Accessed on 18.9. 2018.
- [85] K. D. Rogers. An x-ray diffraction study of semiconductor and metallic vanadium dioxide. *Powder Diffraction*, 8(04):240–244, 1993.
- [86] John M. Longo, Peder Kierkegaard, C. J. Ballhausen, Ulf Ragnarsson, S. E. Rasmussen, Erling Sunde, and Nils Andreas S. A refinement of the structure of VO<sub>2</sub>. *Acta Chemica Scandinavica*, 24:420–426, 1970.
- [87] Y. Y. Luo, L. Q. Zhu, Y. X. Zhang, S. S. Pan, S. C. Xu, M. Liu, and G. H. Li. Optimization of microstructure and optical properties of VO<sub>2</sub> thin film prepared by reactive sputtering. *Journal of Applied Physics*, 113(18):183520, 2013.
- [88] V I Shapovalov and V V Smirnov. Modelling of hot target reactive sputtering. *Journal of Physics: Conference Series*, 857:012039, 2017.
- [89] H. A. Bethe and J. Ashkin. Passage of radiation through matter. *Experimental Nuclear Physics*, 1(2):253, 1953.

- [90] F. Bloch. Zur Bremsung rasch bewegter Teilchen beim Durchgang durch Materie.  
*Annalen der Physik*, 408(3):285–320, 1933.

## List of Figures

1	Schematic of DC-Sputtering . . . . .	4
2	Sputter regimes by means of ion kinetic energy . . . . .	5
3	Schematic drawing of DC magnetron sputtering . . . . .	6
4	Hysteresis of titanium at a fixed power level of 100 W power and at a fixed current of 300 mA . . . . .	7
5	Simulation of hysteresis according to Berg’s model . . . . .	8
6	Comparison of semiconductor to metal transitions in various vanadium oxides . . . . .	10
7	Semiconductor to metal transition between the semiconducting monoclinic and the conductive tetragonal structure of $VO_2$ . . . . .	11
8	Schematic illustration of the terms in the Holstein-Hubbard hamiltonian	12
9	Compositional analysis of thin films produced by J. Theil . . . . .	15
10	Nucleation of thin films . . . . .	19
11	Thronton’s zone diagram . . . . .	20
12	Comparison of theoretical bulk electrical resistivity to one of thin films	22
13	Principle of a four point probe setup . . . . .	23
14	Four point probe setup . . . . .	24
15	Schematic illustration of how transition temperature, hysteresis width and resistivity change are calculated . . . . .	25
16	Schematic drawing of GIXRD in the inset and the generation of interference pattern at the detector . . . . .	28
17	XRD setup used for the (non-heated) GIXRD measurements . . . . .	28
18	Interaction volume of an electron beam with initial energy $E_0$ . . . . .	31
19	SEM setup used for secondary electron images . . . . .	32
20	FTIR setup . . . . .	35
21	Schematic drawing of the sputter system . . . . .	36
22	The glass slide is mounted on a heatable copper substrate holder containing a 300 W heating cartridge . . . . .	38
23	Schematic circuit of the analog to digital converters . . . . .	40
24	Block diagram of the LabView subVI “Arduino_readout.vi” . . . . .	41
25	Front panel of flow and pressure control . . . . .	43
26	Block diagram of the LabView subVI “Pressure_PID_Control.vi” . . . . .	44
27	Block diagram of the LabView subVI “Pressure_PID_Control.vi” . . . . .	45

28	Block diagram of the LabView VI “Steuerung_LABII.lvproj” . . . . .	46
29	Front panel of the subVI “Pressure_hysteresis.vi” . . . . .	47
30	Block diagram of the LabView subVI “Pressure_PID_Control.vi” . . . . .	48
31	True case (control of flow increase) of case structure (3) in fig. 30 . . . . .	49
32	False case (control of flow decrease) of case structure (3) in fig. 30 . . . . .	49
33	<i>Example of copper plates for connection of target to the cooling system and schematic side-view</i> . . . . .	50
34	Illustration of the variables in the one dimensional model . . . . .	51
35	assembly of target holder with mounted vanadium target and plasma ring area . . . . .	54
36	Positioning of the aluminum ring beneath the target . . . . .	56
37	Four-point measurement of sample VOX51 produced at $r_O^{Ar} = 0.05$ . . . . .	63
38	GIXRD scan at $\alpha = 5.5^\circ$ of sample VOX51 produced at $r_O^{Ar} = 0.05$ . . . . .	64
39	Four-point measurement of sample VOX71 produced at $r_O^{Ar} = 0.033$ . . . . .	65
40	GIXRD scan at $\alpha = 5.5^\circ$ of sample VOX71 produced at $r_O^{Ar} = 0.05$ . . . . .	65
41	Four-point measurement of samples VOX86 produced at $r_O^{Ar} = 0.025$ . . . . .	66
42	GIXRD scan at $\alpha = 5.5^\circ$ of sample VOX86 produced at $r_O^{Ar} = 0.025$ . . . . .	67
43	<i>Four-point measurement of the samples produced at <math>r_O^{Ar} = 0.025</math></i> . . . . .	67
44	GIXRD scan at $\alpha = 5.5^\circ$ of sample VOX85 produced at $r_O^{Ar} = 0.025$ . . . . .	68
45	Schematic illustration of the tilted assembly . . . . .	68
46	Four-point measurement of “tilted assembly” sample VOX93 . . . . .	70
47	GIXRD scan of “tilted assembly” sample VOX93 at $\alpha = 5.5^\circ$ . . . . .	71
48	SEM images of a “tilted assembly” sample . . . . .	71
49	Four-point measurement of sample VOX103 produced at $d_C = 10$ mm . . . . .	72
50	GIXRD scan at $\alpha = 5.5^\circ$ , of sample VOX103 produced at $d_C = 10$ mm . . . . .	73
51	Four-point measurement of sample VOX106 produced at $d_C = 6$ mm . . . . .	74
52	GIXRD scan at $\alpha = 5.5^\circ$ , of sample VOX106 produced at $d_C = 6$ mm . . . . .	75
53	Four-point measurement of sample VOX118 produced at $d_C = 2$ mm . . . . .	76
54	GIXRD scan at $\alpha = 5.5^\circ$ , of sample VOX118 produced at $d_C = 2$ mm . . . . .	77
55	Four-point measurement of sample VOX135 produced at $d_C = 1$ mm . . . . .	78
56	GIXRD scan at $\alpha = 5.5^\circ$ , of sample VOX135 produced at $d_C = 1$ mm . . . . .	79
57	GIXRD scan at $\alpha = 5.5^\circ$ of sample VOX135 produced at $d_C = 1$ mm at $25^\circ\text{C}$ (blue: monoclin structure) and $90^\circ\text{C}$ . . . . .	79
58	Resistivity change $r_{IM}$ . . . . .	81
59	Mass absorption coefficient and indirect optical bandgap by Tauc-plot . . . . .	82

60	Transition temperature $T_{Trans}$ . . . . .	82
61	Hysteresis width $\Delta T_H$ . . . . .	83
62	SEM images of the (a) sample VOX103 ;(b) sample VOX107;(c) sample VOX114; (d) sample VOX135; (e) sample VOX71 . . . . .	85
63	Schematic illustration of the Berg-model with contributions to the total reactive gas flow and fractional poisoned areas . . . . .	104
64	Simulation of the target temperature for $d_C = 10 \text{ mm}$ . . . . .	109
65	Simulation of the target temperature for $d_C = 6 \text{ mm}$ . . . . .	110
66	Simulation of the target temperature for $d_C = 2 \text{ mm}$ . . . . .	110
67	Simulation of the target temperature for $d_C = 1 \text{ mm}$ . . . . .	111
68	Simulation of the target temperature for $d_C = 0 \text{ mm}$ . . . . .	111

## List of Tables

1	The transition temperature $T_{c\uparrow}$ and bandgap of different vanadium oxides	9
2	Five crystal systems and the respective constraints on their lattice constants	27
3	Empirically derived values for “Pressure_PID_Control.vi”	45
4	Calculated target temperatures $T_T$	53
5	Simulated target temperatures $T_T^{max}$ and $T_T^{mean}$	55
6	Measured temperature changes $\Delta T_R$ at the ring	59
7	Samples at full target-cooling showing thermochromic behaviour	62
8	Sample at reduced target-cooling showing the best thermochromic behaviour	69
9	Reproducibility at the respective cooling plate diameter $d_C$	80
10	Scherrer calculation of grain size	83

# A Appendix

## A.1 Berg Model

The reactive gas entering the chamber with a flow  $q_0$  is subdivided into the flow that is gettered at the chamber surface and the substrate  $q_c$ , by the target  $q_t$  and pumped out without interacting  $q_p$ . The term  $q_p$  is connected to the reactive gas partial pressure  $p_R$  via the pumping speed  $S$  by  $q_p = p_R \cdot S$ . For a further explanation of the model an illustration of the different contributions to the system is given in fig. 63.



Figure 63: *schematic illustration of the Berg-model; (a) contributions to the total reactive gas flow  $q_0$ , where  $q_t$  is the fraction poisoning the target,  $q_c$  the chamber and  $q_p$  the fraction pumped out without interaction, in total the chamber pressure rises to  $p_R$  for a general gas and  $p_N$  for nitrogen as primarily used by Berg; (b): fractional poisoned areas  $\theta_1, \theta_2$  and mettalic areas  $1 - \theta_1, 1 - \theta_2$  of the target with total area  $A_t$  and chamber with total area  $A_c$  respectively,  $J$  describes the argon atoms sputtering from the target and  $F$  the adsorbed oxygen ions at the target and the chamber;  $F_i$  denote the particle flows from the target to the surface fractions; adapted from [20, 19]*

The reactive gas is on the one hand implanted into the target and either forms compounds or surface impurities, the same applies for the chamber which fraction is denoted  $F$ . The flux of ionization gas  $J$  is responsible for the transport of compounds or elemental target material and reactive gas ions from the target surface to the chamber walls and substrate. In a simple approach the target and the substrate contain only compound material which is sputtered as a compound and pure target atoms which are sputtered as pure target atoms. This assumption does not hold in reality where compounds are mostly not sputtered completely but fractionally. This subdivision allows to define two fractional areas at the target for compound material  $\theta_1$  and for pure target atoms  $1 - \theta_1$  where the total target area is denoted  $A_t$ . At the chamber walls and the substrate, the

fraction  $\theta_2$  denotes sputtered compounds and  $1 - \theta_2$  sputtered pure target atoms where the total surface area is denoted  $A_c$ . The chamber pressure is dependent on the particle flux of reactive atoms  $\frac{dN}{dt}$  which in turn is defined by the consumption and release at the target, the chamber walls and the substrate. From fig. 62 two equations can be derived for the number of particles at the target  $\frac{dN_t}{dt}$  and the chamber walls or substrate  $\frac{dN_c}{dt}$  per time [20, 19]:

$$\begin{aligned} \frac{dN_t}{dt} &= 2 \cdot \alpha_t \cdot F \cdot (1 - \theta_1) - \left(\frac{J}{e}\right) \cdot Y_C \cdot \theta_1 \\ \frac{dN_c}{dt} &= 2 \cdot \alpha_c \cdot F \cdot (1 - \theta_2) + \left(\frac{J}{e}\right) \cdot Y_C \cdot \theta_1 \cdot (1 - \theta_2) \cdot \frac{A_t}{A_c} - \\ &\quad - \left(\frac{J}{e}\right) \cdot Y_T \cdot (1 - \theta_1) \cdot \theta_2 \cdot \frac{A_t}{A_c} \end{aligned} \quad (30)$$

The first term term in  $\frac{dN_t}{dt}$  denotes the flux of free reactive gas ions per time<sup>18</sup>  $F = p_R \cdot (2\pi m k_B T)^{-\frac{1}{2}}$  sticking to fraction  $1 - \theta_1$  with sticking coefficient  $\alpha_t$ .<sup>19</sup> The second term accounts for the sputtered compounds from the fraction  $\theta_1$  which is proportional to number of ionization gas ions  $J/e$  per time and the corresponding sputter yield of the compound  $Y_C$  at the target. The term  $\frac{dN_c}{dt}$  contains the sticking of free reactive gas ions to the fraction  $1 - \theta_2$  of the wall with sticking coefficient  $\alpha_c$ . The second term denotes the deposition of compounds from  $\theta_1$  to  $(1 - \theta_2)$  and the last term includes the sputtering of pure target material  $\left(\frac{J}{e}\right) \cdot Y_T \cdot (1 - \theta_1)$  deposited at the fraction of the chamber walls and substrate already containing compounds  $\theta_2$ , thus lowering the reaction gas content of this fraction by coverage. Together with the two expressions for the flow that is gettered at the chamber and substrate surface  $q_c = \alpha_c \cdot F \cdot (1 - \theta_2) \cdot A_c$  and by the target  $q_t = \alpha_t \cdot F \cdot (1 - \theta_1) \cdot A_t$  a recursive progression for the total flow consumption and the partial pressure of the reactive gas is indicated in the steady state case  $\frac{dN_c}{dt} = \frac{dN_t}{dt} = 0$  by the following recipe:

1. Solving for F and  $q_p$  at given temperature and assumed  $p_R^{(1)}$
2. Solving  $\frac{dN_t}{dt} = 0$  for  $\theta_1^{(1)}$
3. Solving  $\frac{dN_c}{dt} = 0$  for  $\theta_2^{(1)}$
4. Solving  $q_c^{(1)}$  and  $q_t^{(1)}$

---

<sup>18</sup> $p_R = \frac{d}{dA} \frac{d(N_N m \bar{v})}{dt} = \frac{d^2 N_N}{dt dA} m \bar{v} \cong F m \sqrt{v^2} = F \sqrt{2 k_B m T} \rightarrow F = \frac{p_R}{\sqrt{2 k_B m T}}$  in the case of oxygen

and nitrogen the factor 2 accounts for the two ions per double bond

<sup>19</sup>In the Berg model the fraction  $\theta_1$  is already filled with reactive gas atoms to a saturation and thus no further ions are inserted

5. Converting  $q_e^{(1)}$  and  $q_t^{(1)}$  in particles per second to sccm by  $1 \text{ sccm} = 4.47 \cdot 10^{17} \text{ s}^{-1}$
6. Solving  $q_0^{(1)} = S \cdot p_R^{(1)} + q_c + q_t$
7. repeat with  $p_R^{(2)} = p_R^{(1)} + \delta p_R$

## A.2 Explanation of XRD and Laue Condition

Considering a photon of wave vector  $\vec{k}_0 = \frac{2\pi}{\lambda} \vec{e}_0$  moving into the direction  $\vec{e}_0$  and scattered by  $2\theta$  elastically at the local electrons inside the crystal lattice in the direction  $\vec{e}$  with the corresponding wave-vector  $|\vec{k}(2\theta)| = |\vec{k}_0|$ , the scattering vector  $\vec{Q} = \vec{k} - \vec{k}_0$  is then of length  $|\vec{Q}| = \frac{4\pi}{\lambda} \sin(\theta)$ . The information about the crystal structure of solids or thin films is contained in the constructive and destructive interference of scattered photons at different lattice points which is denoted here as  $\vec{r}_{n_1 n_2 n_3} = n_1 \cdot a_1 \cdot \vec{c}_1 + n_2 \cdot a_2 \cdot \vec{c}_2 + n_3 \cdot a_3 \cdot \vec{c}_3$  where  $n_i$  with  $0 \leq n_i \leq N_i - 1$  denotes the  $n_i$ -th position of an atom in direction  $\vec{c}_i$  with lattice constants  $a_i$  describing the multiple of the unit cell in the respective direction. The x-ray source is assumed to emit a monochromatic plane wave which excites bound electrons at a lattice point in a distance  $\vec{R}_Q + \vec{r}_{n_1 n_2 n_3}$  from the source with an electric field strength of  $\vec{E}_Q(\vec{R}_Q + \vec{r}_{n_1 n_2 n_3}) = (\hat{e}_\sigma \cdot E_{0\sigma} + \hat{e}_\pi \cdot E_{0\pi}) \cdot e^{-i\vec{k}_0(\vec{R}_Q + \vec{r}_{n_1 n_2 n_3})} = \vec{E}_0 \cdot e^{-i\vec{k}_0(\vec{R}_Q + \vec{r}_{n_1 n_2 n_3})}$  where  $\sigma$  and  $\pi$  denote the polarization of the x-rays and  $\vec{k}_0$  the initial wave vector. The electron emits a dipole field which is approximated by a spherical wave for great distances. The spherical wave reaches the detector at a distance  $\vec{R} - \vec{r}_{n_1 n_2 n_3}$  under a scattering angle of  $2\theta$  where the wave vector changes by  $\vec{Q}(2\theta)$ . The amplitude of the scattered x-rays additionally depends on the polarization of the incoming light which is denoted by the polarization factor  $C_{\sigma\pi}$ . The amplitude of the scattered wave at the detector in the Fraunhofer limit is then given by:

$$\vec{E}(\vec{R} - \vec{r}_{n_1 n_2 n_3}, 2\theta) \propto C_{\sigma\pi} \frac{\vec{E}_0}{|\vec{R} - \vec{r}_{n_1 n_2 n_3}|} e^{-i\vec{k}_0(\vec{R}_Q + \vec{r}_{n_1 n_2 n_3})} e^{-i(\vec{k}_0 + \vec{Q})(\vec{R} - \vec{r}_{n_1 n_2 n_3})} \quad (31)$$

Assuming that  $\vec{R} \gg \vec{r}_{n_1 n_2 n_3}$  and thus  $|\vec{R} - \vec{r}_{n_1 n_2 n_3}| \cong |\vec{R}|$  and forming the sum over all lattice points yields the total signal under an angle  $2\theta$ :

$$\vec{E}(\vec{R}, 2\theta) \propto C_{\sigma\pi} \frac{\vec{E}_0}{|\vec{R}|} e^{-i\vec{k}_0 \vec{R}_Q} e^{-i(\vec{k}_0 + \vec{Q}) \vec{R}} \sum_{n_1, n_2, n_3} e^{-i\vec{Q} \vec{r}_{n_1 n_2 n_3}} \quad (32)$$

The relevant information is contained in the sum  $f = \sum e^{-i\vec{Q} \vec{r}_{n_1 n_2 n_3}}$  which, for a lattice of size  $N_1, N_2$  and  $N_3$  is given by explicit calculation of the geometric sum by the so called interference function  $\mathfrak{S}(\vec{Q}) = |f|^2$  is given by:<sup>20</sup>

$$\mathfrak{S}(\vec{Q}) = \prod_{i=1}^3 \frac{\sin^2\left(\frac{N_i \vec{Q} \cdot \vec{c}_i a_i}{2}\right)}{\sin^2\left(\frac{\vec{Q} \cdot \vec{c}_i a_i}{2}\right)} \quad (33)$$

This function has a sharp maximum of height  $N_i^2$  where  $\vec{Q} \cdot \vec{c}_i a_i = m_i \cdot 2\pi$ . The diffraction order  $m_i$  defines the Miller indices  $h = m_1, k = m_2, l = m_3$  which are identified as a triple  $hkl$ . Using the fact that  $|\vec{Q}| = \frac{4\pi}{\lambda} \sin(\theta)$  the maximum condition yields the Laue or Bragg condition:<sup>21</sup>

$$\sin(\theta) \cdot d_{hkl} = \frac{\lambda}{2} \quad (34)$$

### A.3 Explanation of SEM by Bethe-formula

The The energy loss  $-\frac{dE}{ds}$  or stopping power of electrons traveling through a medium along the path  $s$  is roughly described by the Bethe formula [89, 90] for energies above 5 keV, which in the non-relativistic limit reads:

$$-\frac{dE}{ds} \propto \frac{\rho_e \cdot e^4}{E} \cdot \ln\left(\frac{4E}{J}\right) \quad (35)$$

The formula contains the charge of the electron  $e$  and the mean excitation potential  $J$  of the atoms and the electron density per volume  $\rho_e \propto Z$  which is proportional to the atomic number of the elements in the medium. For  $J$  various approximations are available one of which is given by  $J = 10 \cdot Z$  eV.[90] The stopping power in eq. 36

$$\begin{aligned} {}^{20} f &= \sum_{n_1, n_2, n_3} e^{-i\vec{Q} \vec{r}_{n_1 n_2 n_3}} = \sum_{i=1}^3 \sum_{n_i=0}^{N_i-1} \left(e^{-i\vec{Q} \cdot \vec{c}_i a_i}\right)^{n_i} = \sum_{i=1}^3 \frac{1 - e^{-iN_i \vec{Q} \cdot \vec{c}_i a_i}}{1 - e^{-i\vec{Q} \cdot \vec{c}_i a_i}} = \\ [1 - e^{-ix} = -2ie^{i\frac{x}{2}} \sin\left(\frac{x}{2}\right)] &= \prod_{i=1}^3 e^{i\frac{(N_i-1)\vec{Q} \cdot \vec{c}_i a_i}{2}} \frac{\sin\left(\frac{N_i \vec{Q} \cdot \vec{c}_i a_i}{2}\right)}{\sin\left(\frac{\vec{Q} \cdot \vec{c}_i a_i}{2}\right)} \rightarrow |f|^2 = \prod_{i=1}^3 \frac{\sin^2\left(\frac{N_i \vec{Q} \cdot \vec{c}_i a_i}{2}\right)}{\sin^2\left(\frac{\vec{Q} \cdot \vec{c}_i a_i}{2}\right)} \end{aligned}$$

$$\begin{aligned} {}^{21} \vec{Q} \cdot (\vec{c}_1 + \vec{c}_2 + \vec{c}_3) &= 2\pi \left(\frac{h^2}{a_1^2} + \frac{k^2}{a_2^2} + \frac{l^2}{a_3^2}\right)^{\frac{1}{2}} \text{ the maximum of this expression is obtained for} \\ \vec{Q} \cdot (\vec{c}_1 + \vec{c}_2 + \vec{c}_3) = |\vec{Q}| &= \frac{4\pi}{\lambda} \sin(\theta) \text{ this yields } \sin(\theta) = \frac{\lambda}{2} \cdot \left(\frac{h^2}{a_1^2} + \frac{k^2}{a_2^2} + \frac{l^2}{a_3^2}\right)^{\frac{1}{2}} \end{aligned}$$

decreases with increasing electron energy and increases with the electron density or atomic number of the medium. Electrons can thus penetrate deeper when they hit a surface with higher primary energies and are stopped earlier in heavier media. The energy of secondary electrons is in the range of J and therefore approximately  $N_{se} \cong \frac{E_0}{J}$  electrons are generated by a single electron of primary energy  $E_0$ . The secondary electrons path out of the sample is also described by eq. 36 but due to their lower initial energy only escape from within some 10 nm and are therefore used to investigate the surface structure. The number of detected secondary electrons thus depends on the initial energy of the impinging electrons and on the atomic mass  $Z$  of the medium. If a surface is built up of different materials, the number of detected secondary electrons varies across the surface and so does the appearance in the SEM.

## A.4 Simulations of Target Temperature by *Solidworks 2017*

The following figures show the target temperature and temperature gradient at various cooling plate diameters  $d_C$ .

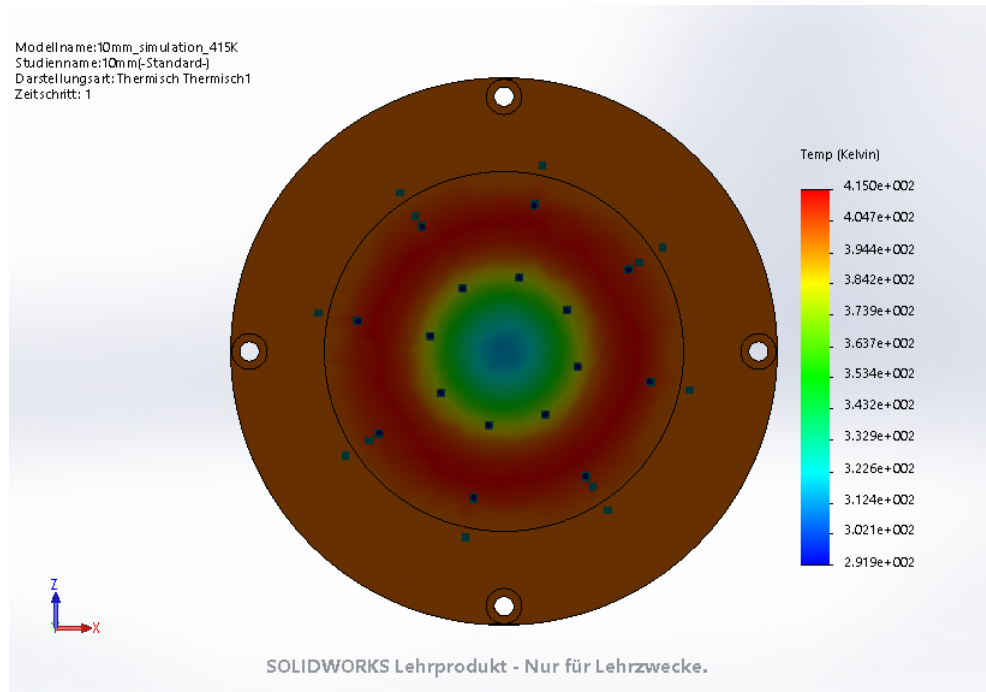


Figure 64: Simulation of the target temperature for  $d_C = 10 \text{ mm}$

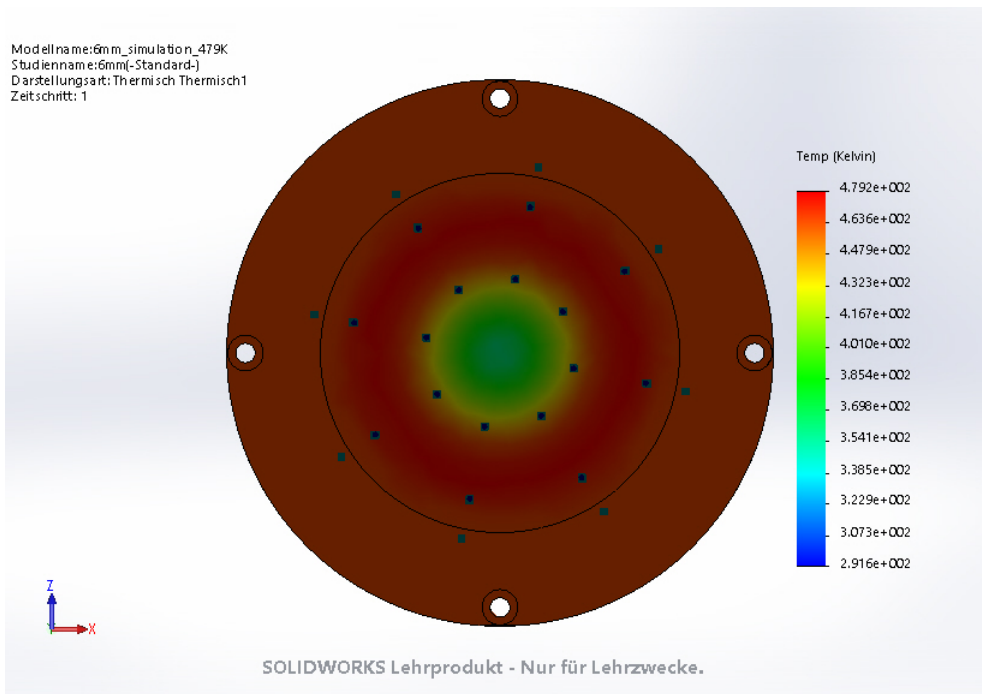


Figure 65: Simulation of the target temperature for  $d_C = 6 \text{ mm}$

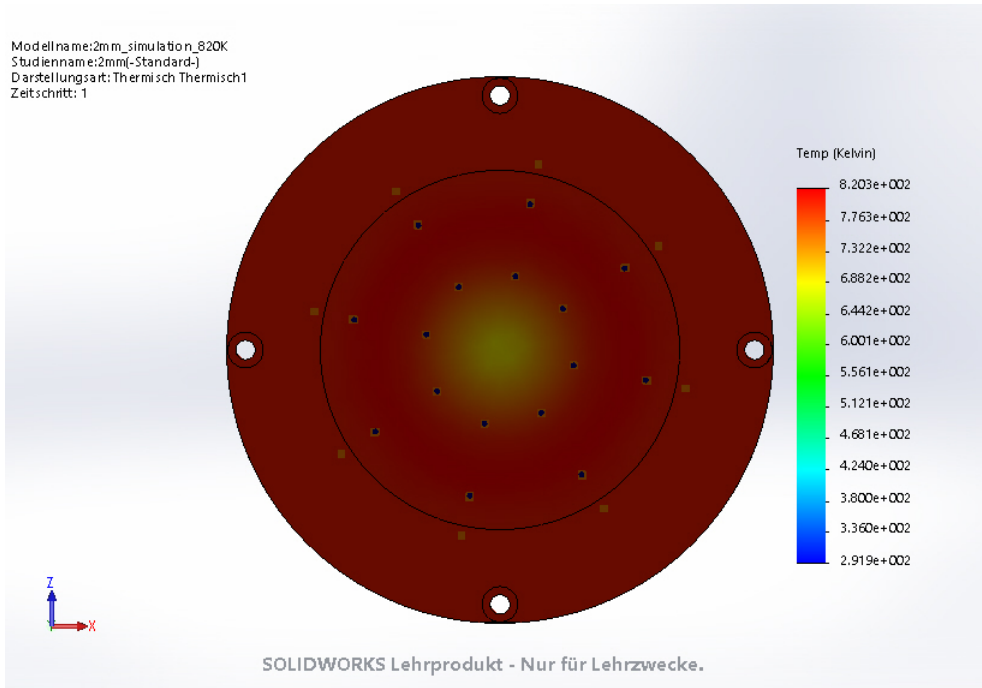


Figure 66: Simulation of the target temperature for  $d_C = 2 \text{ mm}$

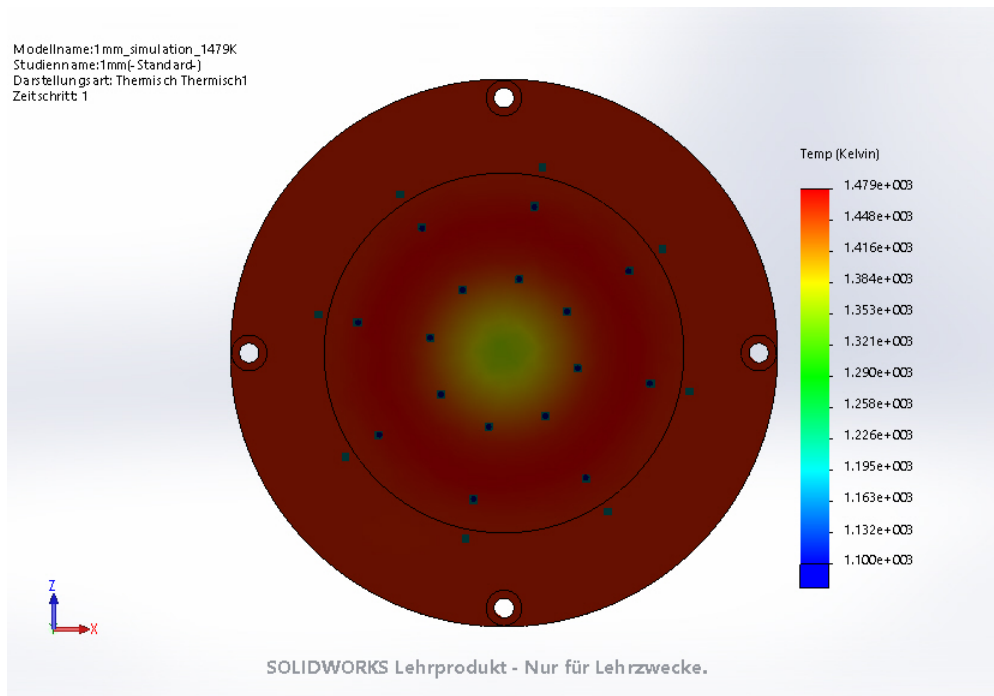


Figure 67: Simulation of the target temperature for  $d_C = 1 \text{ mm}$

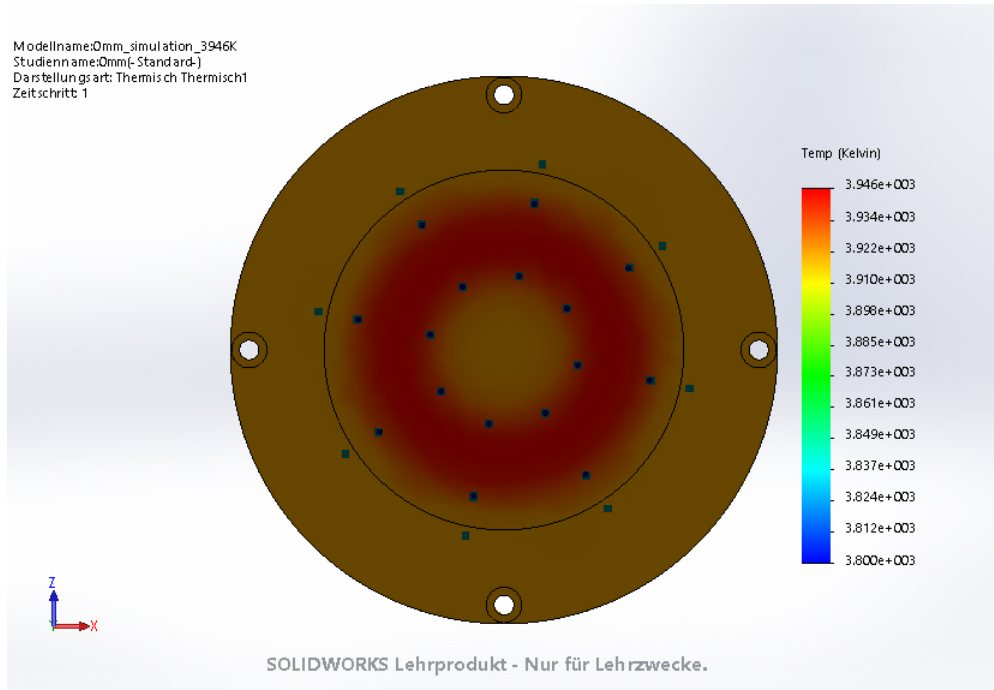


Figure 68: Simulation of the target temperature for  $d_C = 0 \text{ mm}$

## B Table of Measurements

Sub. Name	Target	$T_{Sputt}$ [s]	Substr.	P [W]	U[V]	I [A]	$T_{Sub}$	$p_{Ar}$ [ $10^{-3}$ mbar]	$p_O$ [ $10^{-3}$ mbar]	notes	$d_C$
ABV1	V	600	Si	40	360	0,1	TSputt	0,4	-	SD	
ABV2	V	900	Si	40	360	0,11	Tsputt	0,4	-	=Schichtdicke	
ABV3	V	1200	Si	30	330	0,09	Tsputt	0,4	-	SD	
ABV4	V	1100	Si	30	347	0,085	Tsputt	0,4	-	SD	
ABV5	V	1600	Si	20	320	0,06	Tsputt	0,4	-	SD	
ABV6	V	1400	Si	19	337	0,058	Tsputt	0,4	-	SD	
ABVo1	V	1400	Si	40	492	0,08	Tsputt	0,4	0,028	SD Ar=8,3 sccm	
ABVo2	V	1600	Si	40	492	0,08	Tsputt	0,4	0,054	O2=1 sccm SD Ar=8,3 sccm	
ABVo3	V	1600	Si	50	488	0,1	Tsputt	0,4	0,058	O2=1,5 sccm SD Ar=8,3 sccm	
ABVo4	V	1400	Si	50	489	0,1	Tsputt	0,4	0,053	O2=1,5 sccm SD Ar= 8,3 sccm O2= 1,5 sccm	
ABVo5	V	1400	Si	60	519	0,115	Tsputt	0,4	0,058	SD Ar=8,3 sccm O2=1,5 sccm	
ABVo6	V	1600	Si	60	513	0,118	Tsputt	0,4	0,052	SD Ar=8,3 sccm O2=1,5 sccm	

Sub. Name	Target	$T_{Sputt}$ [s]	Substr.	P [W]	U[V]	I [A]	$T_{Sub}$	$p_{Ar}$ [ $10^{-3}$ mbar]	$p_{O}$ [ $10^{-3}$ mbar]	notes	$d_C$
ABW1	W	600	Si	50	420	0,1	Tsputt	0,4	0	SD Ar=8,26 sccm O2=0	
ABW2	W	1000	Si	50	440	0,1	Tsputt	0,4	0	SD Ar=8,28 sccm O2=0	
ABW5	W	1200	Si	40	422	0,095	Tsputt	0,4	0	SD Ar=8,28 sccm O2=0	
ABW6	W	1000	Si	40	441	0,091	Tsputt	0,4	0	SD Ar=8,12 sccm O2=0	
ABW3	W	1200	Si	60	428	0,14	Tsputt	0,4	0	SD Ar=8,2 sccm O2=0 sccm	
ABW4	W	1000	Si	60	466	0,128	300	0,4	0	SD Ar=8,14 sccm O2=0	
ABVø7	V	1600	Si	110	568	0,192	Tsputt	0,4	0,053	SD Ar=8,07 sccm O2=1,5	
										sccm	

Sub. Name	Target	$T_{Sputt}$ [s]	Substr.	P [W]	U[V]	I [A]	$T_{Sub}$	$p_{Ar}$ [ $10^{-3}$ mbar]	$p_{O}$ [ $10^{-3}$ mbar]	notes	$d_C$
ABVo8	V	1400	Si	110	573	0,191	40	0,4	0,057	SD Ar=8,03 sccm O2=1,5 sccm	
ABVo10	V	1600	Si	50	500	0,1	34	0,4	0,168	SD Ar=8,03 sccm O2=4 sccm	
ABVo11	V	1800	Si	60	501	0,118	Tsputt	0,4	0,167	SD Ar=8,01 sccm O2=4 sccm	
ABVo12	V	1800	Si	110	583	0,187	54	0,4	0,165	SD Ar=8,03 sccm O2=4 sccm	
ABVo9	V	1600	Si	110	584	0,187	40,8	0,4	0,055	SD Ar=7,96 sccm O2=1,5 sccm	
ABVo13	V	292	Si	110	581	0,189	SP: 200 (201- 240)	0,4	0,056	SD Ar=8,2 sccm O2=1,5 sccm	
ABVo14	V	292	Glas dünn	110	574	0,19	200 (195- 204)	0,4	0,048	SD Ar=8,07 sccm O2=1,5 sccm	

Sub. Name	Target	$T_{Sputt}$ [s]	Substr.	P [W]	U[V]	I [A]	$T_{Sub}$	$p_{Ar}$ [ $10^{-3}$ mbar]	$p_{O}$ [ $10^{-3}$ mbar]	notes	$d_C$
ABVO15	V	1600	Si	140	604	0,232	34,8	0,4	0,049	SD Ar=8,15 sccm O2=1,5 sccm	
ABVox16	V	292	Si rau	110	570	0,192	200 (197- 204)	0,4	0,048	SD Ar=8,12 sccm O2=1,5 sccm	
ABVox17	V	292	Glas dick	110	576	0,19	200 (199- 205)	0,4	0,049	SD Ar=8,13 sccm O2=1,5 sccm	
ABVox18	V	400	Si glatt	110	584	0,188	200 (197- 203)	0,4	0,155	SD Ar=8,14 sccm O2=4 sccm	
ABVox19	V	400	Si rau	110	583	0,188	200 (197- 204)	0,4	0,157	SD Ar=8,06 sccm O2=4 sccm	
ABVox20	V	400	Glas dick	110	575	0,191	200 (197- 203)	0,4	0,154	SD Ar=7,93 sccm O2=4 sccm	
ABVox21	V	640	Si glatt	60	503	0,188	200 (197- 203)	0,4	0,054	SD Ar=8,03 sccm O2=1,5 sccm	

Sub. Name	Target	$T_{Sputt}$ [s]	Substr.	P [W]	U[V]	I [A]	$T_{Sub}$	$p_{Ar}$ [ $10^{-3}$ mbar]	$p_O$ [ $10^{-3}$ mbar]	notes	$d_C$
ABVox22	V	640	si rau	60	490	0,12	200 (199-205)	0,4	0,056	SD Ar=8,17 sccm O2=1,5 sccm	
ABVox23	V	640	Glas dick	60	503	0,118	200 (199-205)	0,4	0,054	SD Ar=8,09 sccm O2=1,5 sccm	
ABVox24	V	640	Si glatt	60	510	0,12	200 (197-204)	0,4	0,053	SD Ar=8,04 sccm O2=1,5 sccm	
ABVox25	V	700	Glas dick	60	510	0,116	200 (197-203)	0,4	0,16	SD Ar=8,19 sccm O2=4 sccm	
ABVox26	V	700	Si glatt	60	520	0,114	200 (198-202)	0,4	0,157	SD Ar=8,01 sccm O2=4 sccm	
ABVox27	V	700	Si rau	60	524	0,113	200 (196-201)	0,4	0,157	SD Ar=8,08 sccm O2=4 sccm	
ABVox28	V	1600	Glas dick	110	575	0,191	200 (198-203)	0,4	0,054	SD Ar=8,04 sccm O2=1,5 sccm	

Sub. Name	Target	$T_{Sputt}$ [s]	Substr.	P [W]	U[V]	I [A]	$T_{Sub}$	$p_{Ar}$ [ $10^{-3}$ mbar]	$p_{O}$ [ $10^{-3}$ mbar]	notes	$d_C$
ABVox29	V	1600	Si glatt	110	570	0,193	200 (197-202)	0,4	0,055	SD Ar=8,06 sccm O2=1,5 sccm	
ABVox30	V	1600	Si grau	110	574	0,191	202 (199-204)	0,4	0,056	SD Ar=8,05 sccm O2=1,5 sccm	
ABVox31	V	1600	Si glatt	110	570	0,19	200 (197-203)	0,4	0,055	SD Ar=8,15 sccm O2=1,5 sccm	
ABVox32	V	2000	Glas dick	110	575	0,187-019	200 (197-203)	0,4	0,16	SD Ar=8,14 sccm O2=4 sccm	
ABVox33	V	2000	Si rau	110	570	0,191	200 (197-203)	0,4	0,154	SD Ar=8,04 sccm O2=4 sccm	
ABVox34	V	2000	Si glatt	110	580	0,188	200 (198-203)	0,4	0,157	SD Ar=8,1 sccm O2=4 sccm	
ABVox35	V	3600	Si glatt	60	510	0,115	200 (197-203)	0,4	0,157	SD Ar=8,14 sccm O2=1,5 sccm	

Sub. Name	Target	$T_{Sputt}$ [s]	Substr.	P [W]	U[V]	I [A]	$T_{Sub}$	$p_{Ar}$ [ $10^{-3}$ mbar]	$p_{O}$ [ $10^{-3}$ mbar]	notes	$d_C$
ABVox36	V	3600	Si rau	60	507	0,116	200 (196-203)	0,4	0,054	SD Ar=8,13 sccm O2=1,5 sccm	
ABVox37	V	3600	Glas dick	60	510	0,115	200 (200-205)	0,4	0,058	SD Ar=8,1 sccm O2=1,5 sccm	
ABVox38	V	4000	Si glatt	60	512	0,115	200 (197-203)	0,4	0,056	SD Ar=8,16 sccm O2=4 sccm	
ABVox39	V	4000	Si rau	60	516	0,114	200 (196-202)	0,4	0,156	SD Ar=8,14 sccm O2=4 sccm	
ABVox40	V	4000	Glas dick	60	503	0,117	200 (197-203)	0,4	0,162	SD Ar=8,21 sccm O2=4 sccm	
ABVox41	V	300	Glas dick	110	560	0,196	300 (295-305)	0,4	0,16	SD Ar=28,81 sccm O2=1,3 sccm	
ABVox42	V	1000	Glas dick	110	563	0,194	425 (419-431)	0,4	0,042	SD Ar=8,13 sccm O2=10,05 sccm	

Sub. Name	Target	$T_{Sputt}$ [s]	Substr.	P [W]	U[V]	I [A]	$T_{Sub}$	$p_{Ar}$ [ $10^{-3}$ mbar]	$p_O$ [ $10^{-3}$ mbar]	notes	$d_C$
ABVOx43	V	500	Glas dick	110	412	0,27	400 (mit neuem Regler +0°C)	0,4	0,402	SD Ar=8,06 sccm O2=0,75 sccm	
AB-VOX44	V	1200	Si glatt	170	465	0,36	TSputt	0,4	0,056	SD Ar=8,04 sccm O2= 1,5 sccm	
MZSDVO1	V	1200	Si glatt	170	596	0,283	TSputt	0,4	0,16	SD Ar= 8,05 sccm O2= 4 sccm	
ABVOX45	V	320	Glas dick	170	572	0,294	400°C +0,5	0,4	0,158	SD Ar= 8,17 sccm O2= 4sccm	
ABVOX46	V	1800	Glas dick	170	590	0,286	400°C ±0,6	0,4	0,159	Ar=8,12 sccm O2= 4 sccm	
ABVOX47	V	1800	Glas dick	170	571	0,29	400°C±0,40,266	0,40,266	0,084	Ar=5,26 sccm O2= 2,26 sccm	
ABVOX48	V	900	Glas dick	190	587	0,32	400°C±0,40,4	0,40,4	0,112	Ar= 7,78 sccm O2= 3 sccm	

Sub. Name	Target	$T_{Sputt}$ [s]	Substr.	P [W]	U[V]	I [A]	$T_{Sub}$	$p_{Ar}$ [ $10^{-3}$ mbar]	$p_O$ [ $10^{-3}$ mbar]	notes	$d_C$
ABVOX51	V	1400	Glas dick	200			700°C	10	0,5	Ar= 22 sccm O2= 2 sccm	
ABVOX69	V	300	Glas dick	200	542	0,37	700°C	0,4	0,058	Ar=8,08 sccm O2=2 sccm	
ABVOX70	V	600	Glas dick	200	557	0,35	700°C	4	1,5	Ar= 8,21 sccm O2= 4 sccm	
ABVOX71	V	600	Glas dick	200	452	0,41	700°C	15	0,55	Ar= 34 sccm O2= 2,5 sccm	
ABVOX72	V	600	Glas dick	200	530	0,35	700°C	2	0,87	Ar= 3,88 sccm O2= 2,5 sccm	
ABVOX73	V	600	Glas dick	200	436	0,49	700°C	18	0,45	Ar= 42,3 sccm O2= 2,3 sccm	
ABVOX74	V	200	Glas dick	200	448	0,43	700°C	18	0,53	Ar= 42,5 sccm O2= 2,5 sccm	
ABVOX75	V	600	Glas dick	200	447	0,44	700°C	18	0,5	Ar= 42,3 sccm O2= 2,5 sccm	

Sub. Name	Target	$T_{Sputt}$ [s]	Substr.	P [W]	U[V]	I [A]	$T_{Sub}$	$p_{Ar}$ [ $10^{-3}$ mbar]	$p_O$ [ $10^{-3}$ mbar]	notes	$d_C$
ABVOX76	V	600	Glas dick	200	485	0,41	700°C	10	0,57	Ar= 22 sccm O2= 2,3 sccm Mythlayer 1.) 60 sec 2,3 sccm 2.) 20 sec: 0 sccm ab 540 sec. Murmeln 2,3 sccm	
ABVOX77	V	320	Glas dick	200	480	0,81	700°C	10	0,5	Ar= 21,9 sccm O2= 2,3 sccm 1.) 60 sec.: 2,3 sccm 2.) 5 sec.: 0 sccm	
ABVOX78	V	300	Glas dick	200	443	0,45	700°C	20	0,5	Ar= 47,9 sccm O2= 2,5 sccm	
ABVOX79	V	600	Glas dick	200	510	0,39	700°C	4	0,55	Ar= 8,08 sccm O2= 2,3 sccm red. Sccm after 200 sec. To 2 sccm	

Sub. Name	Target	$T_{Sputt}$ [s]	Substr.	P [W]	U[V]	I [A]	$T_{Sub}$	$p_{Ar}$ [ $10^{-3}$ mbar]	$p_O$ [ $10^{-3}$ mbar]	notes	$d_C$
ABVOX80	V	600	Glas dick	200	517	0,38	750°C	4	0,61	Ar= 8,12 sccm O2= 2,5 sccm	
ABVOX81	V	600	Glas dick	200	470	0,41	750°C	10	0,62	Ar= 21,96 sccm O2= 2,6 sccm	
ABVOX82	V	900	Glas dick	200	472	0,4	700°C	10	0,58	Ar= 22,04 sccm O2= 2,6 sccm	
ABVOX83	V	900	Glas dick	200	529	0,37	700°C	4	0,62	Ar= 8,23 sccm O2= 2,5 sccm	Erhitzung deutlich!
ABVOX84	V	900	Glas dick	200	535	0,36	700°C	4	0,66	Ar= 8,12 sccm O2= 2,5 sccm	
ABVOX85	V	900	Glas dick	200	449	0,43	700°C	20	0,57	Ar= 47,86 sccm O2= 2,75 sccm	
ABVOX86	V	900	Glas dick	200	455	0,4	700°C	20	0,57	Ar= 47,85 sccm O2= 2,7 sccm	
ABVOX87	V	900	Glas dick	200	PNCL:463 MDX: 0,47	PNCL:463 MDX: 0,47	700°C	20	0,69	Ar= 47,76 sccm O2= 2,7 sccm	
					29	MDX:0,07					

Sub. Name	Target	$T_{Sputt}$ [s]	Substr.	P [W]	U[V]	I [A]	$T_{Sub}$	$p_{Ar}$ [ $10^{-3}$ mbar]	$p_{O}$ [ $10^{-3}$ mbar]	notes	$d_C$
ABVOX88	V	900	Glas dick	200	430	0,46	700°C	20	0,44	Ar= 47,54 sccm O2= 2,5 sccm <— 2,7 sccm reduziert aktive Kontrolle des Potentialdrucks auf <= 0,5 mbar durch sccm regulieren	
ABVOX89	V	900	Glas dick	200	456	0,43	700°C	20	0,73	Ar= 47,5 sccm O2= 3 sccm	
ABVOX90	V	900	Glas dick	200	442	0,45	750°C	20	0,5	Ar= 47,55 sccm O2= 2,6 sccm Druck aktiv auf <0,55 reguliert	
ABVOX91	V	900	Glas dick	200	435	0,46	750°C	20	0,35	tarte Druckuntersch. Durch Erhöhung -> Druck sinkt zunächst bei O2 Zufuhr wegen	tilted

Sub. Name	Target	$T_{Sputt}$ [s]	Substr.	P [W]	U[V]	I [A]	$T_{Sub}$	$p_{Ar}$ [ $10^{-3}$ mbar]	$p_O$ [ $10^{-3}$ mbar]	notes	$d_C$
ABVOX92	V	900	Glas dick	200	432	0,46	750°C	20	0,7	Ar= 47,6 sccm O2= 3,5 sccm	tilted
ABVOX93	V	900	Glas dick	200	436	0,45	750°C	20	0,7	Ar= 47,4 sccm O2= 3,5 sccm	tilted
ABVOX94	V	900	Glas dick	200	433	0,46	750°C	20	0,7	Ar= 47,4 sccm O2= 3,5 sccm +1h bei 750°C post annealing 15:20-16:20	tilted
ABVOX95	V	150	Glas dick	200	432	0,46	750°C	20	0,7	Ar= 47,6 sccm O2= 3,6 sccm Hirkser zu Beginn!	tilted
ABVOX96	V	200	Glas dick	200	462	0,43	750°C	10	0,69	Ar= 21,7 sccm O2= 3 sccm	tilted
ABVOX97	V	200	Glas dick	215	452	0,46	750°C	20	0,73	Ar= 47,2 sccm O2= 3,35 sccm	
ABVOX98	V	200	Glas dick	260	470	0,55	750°C	20	0,75	Ar= 47,6 sccm O2= 3,4 sccm	

Sub. Name	Target	$T_{Sputt}$ [s]	Substr.	P [W]	U[V]	I [A]	$T_{Sub}$	$p_{Ar}$ [ $10^{-3}$ mbar]	$p_{O}$ [ $10^{-3}$ mbar]	notes	$d_C$
ABVOX99	V	200	Glas dick	300 +10 min pre. Und.	470	0,63	750°C	20	0,93	Ar= 47,6 sccm O2= 4,3 sccm	
AB- VOXI00	V	150	Glas dick	200	432	0,46	750°C	20	0,8	Ar= 46,5 sccm O2= 3,3 sccm	0
ABVOX101	V	200	Glas dick	140	451	0,29	750°C	4	1,26	Ar= 7,9 sccm O2= 4,5 sccm	0
ABVOX102	V	200	Glas dick	200	439	0,44	750°C	20	0,7	Ar= 47,26 sccm O2= 3,5 sccm	10
AB- VOXI03	V	200	Glas dick	230	448	0,5	750°C	20	0,7	Ar= 47,5sccm O2= 3,5 sccm	10
ABVOX104	V	200	Glas dick	230	447	0,51	400°C	20	0,7	Ar= 47,75sccm O2= 3,6 sccm	10
ABVOX105	V	200	Glas dick	230	453	0,5	750°C	20	0,8	Ar= 47,4sccm O2= 3,5 sccm	10

Sub. Name	Target	$T_{Sputt}$ [s]	Substr.	P [W]	U[V]	I [A]	$T_{Sub}$	$p_{Ar}$ [ $10^{-3}$ mbar]	$p_{O}$ [ $10^{-3}$ mbar]	notes	$d_C$
AB- VOXI06	V	300	Glas dick	200	455	0,44	750°C	20	0,79	Ar= 47,8sccm O2= 3,4 sccm / 5 min V.	6
AB- VOXI07	V	500	Glas dick	200	442	0,45	750°C	20	0,68	pre.cond. Ar= 47,5sccm O2= 3,5 sccm / 5 min V.	6
ABVOXI08	V	500	Glas dick	200	439	0,45	750°C	20	0,48	pre.cond. Ar= 47,6 sccm O2= 3 sccm / 5 min V.	6
ABVOXI09	V	400	Glas dick	200	443	0,46	750°C	20	0,65	pre.cond. Ar= 47,3 sccm O2= 3,5 sccm	2
ABVOXI10	V	400	Glas dick	200	441	0,45	750°C	20	0,6	Ar= 47,3 sccm O2= 3,7 sccm /5 min V.pre. cond.	2

Sub. Name	Target	$T_{Sputt}$ [s]	Substr.	P [W]	U[V]	I [A]	$T_{Sub}$	$p_{Ar}$ [ $10^{-3}$ mbar]	$p_O$ [ $10^{-3}$ mbar]	notes	$d_C$
ABVOX111	V	400	Glas dick	200	457	0,45	750°C	20	0,86	Ar= 47,3 sccm O2= 3,5 sccm /5 min V pre. Cond.	2
ABVOX112	V	400	Glas dick	200	439	0,46	400°C	20	0,6	Ar= 47,5 sccm O2= 4 sccm /3 min V pre. Cond.	2
ABVOX113	V	400	Glas dick	200	458	0,45	750°C	20	1,12	Ar= 47,75 sccm O2= 4 sccm /3 min V pre. Cond.	2
AB- VOX114	V	400	Glas dick	200	448	0,45	750°C	20	0,75	Ar= 47,7 sccm O2= 4,4 sccm /5 min V pre. Cond.	2
ABVOX115	V	400	Glas dick	200	453	0,45	750°C	20,06	0,77	Ar= 47,6 sccm O2= 4,3 sccm /5 min V pre. Cond.	2

Sub. Name	Target	$T_{Sputt}$ [s]	Substr.	P [W]	U[V]	I [A]	$T_{Sub}$	$p_{Ar}$ [ $10^{-3}$ mbar]	$p_{O}$ [ $10^{-3}$ mbar]	notes	$d_C$
ABVOX116	V	200	Glas dick	200	451	0,46	750°C	20,1	0,7	Ar= 47,8 sccm O2= 4,3 sccm /5 min V pre. Cond.	2
ABVOX117	V	200	Glas dick	200	443	0,47	750°C	20,07	0,67	Ar= 47,8 sccm O2= 4,2 sccm /10 min V pre. Cond.	2
AB- VOX118	V	200	Glas dick	200	453	0,45	750°C	20	0,85	Ar= 47,8 sccm O2= 4,5 sccm /10 min V pre. Cond.	2
ABVOX119	V	200	Glas dick	200	441	0,46	750°C	20,06	0,73	Ar= 47,7 sccm O2= 3,7 sccm /5 min V pre. Cond.	1
ABVOX120	V	200	Glas dick	200	449	0,45	750°C	20,08	0,79	Ar= 46,6 sccm O2= 5 sccm /15 min V pre. Cond.	1

Sub. Name	Target	$T_{Sputt}$ [s]	Substr.	P [W]	U[V]	I [A]	$T_{Sub}$	$p_{Ar}$ [ $10^{-3}$ mbar]	$p_O$ [ $10^{-3}$ mbar]	notes	$d_C$
ABVOX121	V	200	Glas dick	200	365	0,56	400°C	20	0	Ar=47,6 sccm Probe	1
ABVOX122	V	200	Glas dick	200	436	0,46	750°C	akuter Druck- ausstieg wen sputt 20	0,65	weggedreht, ohne Shutter Ar= 47,7 sccm O2= 4,1 sccm /2 min V pre. Cond.; ohne Shutter	1
ABVOX123	V	130	Glas dick	200	446	0,46	750°C	20,06	1,1	Ar= 47,5 sccm O2= 4,5 sccm /1 min V pre. Cond.; Kurzschluss	1
ABVOX124	V	200	Glas dick	200	447	0,45	750°C	20,04	0,96	Ar= 47,8 sccm O2= 4,5 sccm	1

Sub. Name	Target	$T_{Sputt}$ [s]	Substr.	P [W]	U[V]	I [A]	$T_{Sub}$	$p_{Ar}$ [ $10^{-3}$ mbar]	$p_{O}$ [ $10^{-3}$ mbar]	notes	$d_C$
ABVOX125	V	200	Glas dick	200	438	0,46	750°C neues Heizele- ment	20	0,72	Ar= 47,6 sccm / O2= 3,9 sccm / +dünne V Schicht weil Probe kurz falsch nur kein V. pre. cond.	1
ABVOX126	V	200	Glas dick	200	443	0,46	750°C	20,09	1,1- 1,25	Ar= 47,8 sccm / O2= 4,5 sccm / 2min V pre. Cond	1
ABVOX127	V	400	Glas dick	200	446	0,46	750°C	20,1	1,05- 1,27	Ar= 47,8 sccm / O2= 5 sccm / 2min V pre. Cond	1
ABVOX128	V	600	Glas dick	200	448	0,46	750°C	20,05	1,05- 1,4	Ar= 47,5 sccm / O2= 5,1 sccm / 5min V pre. Cond	1

Sub. Name	Target	$T_{Sputt}$ [s]	Substr.	P [W]	U[V]	I [A]	$T_{Sub}$	$p_{Ar}$ [ $10^{-3}$ mbar]	$p_O$ [ $10^{-3}$ mbar]	notes	$d_C$
ABVOX129	V	400	Glas dick	200	447	0,46	750°C	20,05	1,28-1,63	Ar= 47,6 sccm / O2= 6 sccm / 5min V pre. Cond	1
ABVOX130	V	600	Glas dick	200	446	0,46	750°C	20,05	1,36-1,72	Ar= 47,5 sccm / O2= 6 sccm / 5min V pre. Cond ; V-Target 1,27 mm abgetragen	1
ABVOX131	V and W	300	Glas dick	V: 200 W:10	V: 445 W: 26,8	V: 0,46 W: 0,37	750°C	20,1	1,05-1,4	Ar= 47,7 sccm / O2= 6 sccm / 5min V pre. Cond	1
ABVOX132	V and W	400	Glas dick	V:200 W:7	V:446 W:353	V:0,46 W:0,02	750°C	20,07	1,1-1,4	Ar= 47,8 sccm / O2= 4,6 sccm / 3min V pre. Cond	1

Sub. Name	Target	$T_{Sputt}$ [s]	Substr.	P [W]	U[V]	I [A]	$T_{Sub}$	$p_{Ar}$ [ $10^{-3}$ mbar]	$p_{O}$ [ $10^{-3}$ mbar]	notes	$d_C$
ABVOX133	V	400	Glas dick	200	443	0,46	750°C	20,1	1-	Ar= 47,7 sccm / O2= 4,5 sccm / 4min V pre. Cond	1
ABVOX134	V	400	Glas dick	200	442	0,46	750°C	20,12	1,1- 1,4	Ar= 47,8 sccm / O2= 5,1 sccm / 4min V pre. Cond	1
AB- VOX135	V	400	Glas dick	200	447	0,46	750°C	20,1	1,1- 1,25	Ar= 47,85 sccm / O2= 4,5 sccm / 2min V pre. Cond	1
ABVOX136	V and W	300	Glas dick	V:200 W:40	V:445 W:458	V:0,46 W:0,085	750°C	20	1,1- 1,17	Ar= 47,8 sccm / O2= 4,7 sccm / 2min V pre. Cond (Plasma Abbruch bei 200 sec -> neu zünden	1